Title
REDUCTION OF NITRIC OXIDE BY CARBON MONOXIDE OVER A SILICA SUPPORTED PLATINUM CATALYST: INFRARED AND KINETIC STUDIES

Permalink
https://escholarship.org/uc/item/5g33c0nw

Author
Lorimer, D.H.

Publication Date
1978-08-01

REDUCTION OF NITRIC OXIDE BY CARBON MONOXIDE
OVER A SILICA SUPPORTED PLATINUM CATALYST:
INFRARED AND KINETIC STUDIES

D'Arcy Harold Lorimer
(Ph.D thesis)

July 1978

REDUCTION OF NITRIC OXIDE BY CARBON MONOXIDE
OVER A SILICA SUPPORTED PLATINUM CATALYST:
INFRARED AND KINETIC STUDIES

by

D'Arcy Harold Lorimer

Lawrence Berkeley Laboratory
University of California
Berkeley, California 94720

Table of Contents

List of Figures

List of Tables

REDUCTION OF NITRIC OXIDE BY CARBON MONOXIDE OVER A SLICA

SUPPORTED PLATINUM CATALYST: INFRARED AND KINETIC STUDIES

D'Arcy H. Lorimer

Materials and Molecular Research Division
Lawrence Berkeley Laboratory and Department of Chemistry
University of California
Berkeley, California   94720

ABSTRACT

The reduction of nitric oxide by carbon monoxide over a 4.5 weight precent platinum catalyst supported on silica was studied at $300^{\circ}C$. Reaction rate data was obtained together with in situ infrared spectra of species on the catalyst surface. The kinetics of the system were found to exhibit two distinct trends, depending on the molar ratio of CO/NO in the reactor. For net reducing conditions (CO/NO > 1) the catalyst underwent a transient deactivation, the extent of which was dependent on the specific CO/NO ratio during reaction. Reactivation of the catalyst was obtained with both oxidizing and reducing pretreatments. For molar feed ratios of CO/NO less than one, carbon monoxide conversion was typically 95 to 100%, resulting in strongly oxidizing conditions over the catalyst. Under these conditions no deactivation was apparent. Infrared spectra recorded under reaction conditions revealed intense bands at 2075 and 2300 cm^{-1}, which were identified as carbon monoxide adsorbed on Pt and Si-NCO, respectively. Isocyanate bands formed under reducing conditions were more intense and exhibited greater stability than those formed under oxidizing conditions.

A reaction mechanism based on the dissociation of nitric oxide as the rate-limiting step was used to correlate nitric oxide reaction

rates and nitrous oxide selectivities observed under reducing conditions.
As part of this mechanism it is assumed that nitrous oxide is formed
via a Langmuir-Hinshelwood process in which an adsorbed nitrogen atom
reacts with an adsorbed nitric oxide molecule. The nitric oxide reaction
rate was found to be first order in nitric oxide partial pressure,
and inverse second order in carbon monoxide partial pressure.

A mechanism is proposed to qualitatively explain the deactivation
process observed under reducing conditions. The essential part of
this mechanism is the formation of an isocyanate species on the Pt
crystallites of the catalyst and the subsequent transient diffusion
of these species to the silica support. The deactivation is believed
to result from the build-up of NCO on vacant sites necessary for the
dissociation of nitric oxide.

I.   INTRODUCTION AND LITERATURE REVIEW

The importance of automative emissions control in recent years has focused much attention on the catalytic reduction of nitric oxide. Since 1975, most automobile manufacturers have used catalytic oxidation to reduce CO and hydrocarbon emissions, and have relied on engine modifications for the reduction of NO_x emissions. However, such modifications are inadequate to comply with future NO_x emission requirements. As a result, the catalytic approach is being considered for the control of all three major pollutants; NO_x, CO, and hydrocarbons. This means that the catalyst must be capable of utilizing the reducing agents present in the exhaust stream for nitric oxide reduction. Previous investigations have revealed that CO and H_2 are the major reducing agents involved in NO reduction and that the major nitrogen containing reaction products are N_2, N_2O, and NH_3. This work has also demonstrated that at least eight reactions pertaining to NO reduction take place simultaneously in a catalytic converter. Obviously, with such complexity it is not possible to obtain information regarding the surface mechanisms through which the reduction of NO occurs. Since the gathering of basic mechanistic information is of central importance in this study, simplification of the reaction system to two reactants was necessary to accomplish this goal.

A. Introduction

The purpose of this investigation was to study the mechanisms

by which NO and CO interact over a platinum catalyst. As yet these

mechanisms have not been firmly established, since very little work

has been reported containing quantitative rate expressions. Platinum

was chosen as the catalyst due to its potential widespread use as

the main constituent in the proposed three way automotive catalytic

converters. In addition, a significant amount of adsorption and infrared

data is available in the literature for various gases on platinum.

The experimental approach involved the recording of infrared spectra

of species adsorbed on the catalyst under reaction conditions and

the simultaneous collection of kinetic data.

B. Literature Review

1. Nitric Oxide and Carbon Monoxide Adsorption Studies

Recent work gives detailed information on the absorption of carbon

monoxide on platinum. Winterbottom (2) found two distinct surface

states for carbon monoxide on polycrystalline platium in thermal desorption

studies. In thermal desorption work on the 110 surface of platinum,

Lambert and Comrie (3) also found two carbon monoxide adsorption sites

with heats of adsorption of 25 and 31 kcal/mole. Somorjai et al (4)

has reported the dissociative adsorption of carbon monoxide at the

steps and kinks of a platinum vicinal surface, the adsorption being

associative at the terrace sites. Finally, infrared spectra of carbon

monoxide adsorbed on platinum exhibit a strong band at 2075 cm^{-1} (5).

A significant amount of work on the adsorption of nitric oxide

on platinum has also been reported. The work of Lambert and Comrie (3)

indicates that two surface sites for the molecular adsortion of ntric

oxide, having heats of adsorption of 23 and 28 kcal/mole, exist on

the 110 surface of platinum. The nitric oxide on one of these sites

dissociates readily into adsorbed nitrogen and oxygen atoms at temper-

atures greater than $200^{\circ}C$. These results are in good agreement with

those of Pirug and Bonzel (6, 7) who found significant nitric oxide

dissociation in the temperature range of 180 to $220^{\circ}C$ on the 100 surface

of platinum. These authors (6, 7) found only molecular nitric oxide

adsorbed at temperatures lower than $100^{\circ}C$. The adsorption and desorption

of nitric oxide on a 5% Pt/Al_2O_3 catalyst has been reported by Solymosi

et al (8). At adsorption temperatures greater than $100^{\circ}C$, nitrous

oxide was detected in the gas phase during nitric oxide adsorption,

and at $400^{\circ}C$, significant amounts of nitrous oxide, oxygen and nitrogen

were detected. The characteristics of the thermal desorption of nitric

oxide were complex and highly dependent on the temperature of adsorption.

Broad infrared bands, in the region of 1760 to 1785 cm^{-1}, arising

from adsorbed nitric oxide (at low temperature) on platinum have been

report by Ludvik (9), Duken and Hobert (10), and Brown and Gonzalez (11).

2.   Kinetic Studies

Experimental investigations of nitric oxide reduction by carbon

monoxide have been reported by a number of researchers. Some of these

studies (12-15) have been aimed at comparing the relative activity

of various noble metal and transition metal oxide catalysts, and have

not been directed toward establishing rate expressions and mechanisms

for the kinetics. Lambert and Comrie (3) have studied the Langmuir-

Hinshelwood reaction between co-adsorbed nitric oxide and carbon monoxide

at low pressure on the 111 and 110 platinum surfaces. A reaction
mechanism was proposed which accounts for the relative amounts of
the individual products, and involves the dissociation of adsorbed
NO prior to the formation of any products. Cant et al (1) have studied
the reduction of nitric oxide by carbon monoxide over five silica
supported noble metal catalysts, including platinum. The nitric oxide
reaction rate over the platinum catalyst was determined to be approximately
first order in nitric oxide partial pressure, and approached inverse
order in carbon monoxide. A mechanism involving nitric oxide dissociation
as the rate limiting step was proposed to explain the observed kinetics.
Nitrous oxide formation was assumed to occur via a Langmuir-Hinshelwood
process involving nitrogen atoms and adsorbed nitric oxide molecules,
and molecular nitrogen was assumed to form via the recombination of
two absorbed nitrogen atoms. Finally, Niiyama et al (16) have also
studied the reduction of NO by CO and reported the decline in activity
of a Pt/Al_2O_3 catalyst under reaction conditions, which was attributed
to the formation of a platinum isocyanate species.

3.   Studies Relating to the Formation and Observation of Isocyanate Species

Infrared studies of the interaction of NO and CO on noble metal
catalysts have revealed the formation of an isocyanate species and
a number of authors have speculated about its role in the reduction
mechanism. Unland (17-19) has observed intense infrared bands at
2270 cm^{-1} in studies involving the high temperature dosing of an alumina
supported platinum catalyst with mixtures of nitric oxide and carbon
monoxide. These results are consistent with those reported by Solymosi
et al (8) and Niiyama (16) for alumina supported platinum catalysts.

Ludvik (9) has identified an infrared band at 2300 cm^{-1} as belonging to an isocyanate species formed during the reaction of nitric oxide and carbon monoxide over a platinum catalyst supported on silica.

Recently it has been proposed that the isocyanate species observed by infrared absorption is bonded to the catalyst support rather than to the metal. Dalla Betta and Shelef (20) have studied isocyanate formation over silica and alumina supported platinum catalysts, and have observed intense infrared bands at 2260 cm^{-1} for alumina supported platinum and 2304 cm^{-1} for silica supported platinum. Due to the large intensity of the infrared bands and the significant 44 cm^{-1} frequency shift between bands on different supports, these authors have identified the infrared bands as belonging to isocyanate species bonded to the alumina and silica supports. These results are in good agreement with studies reported by Eley et al (21) and Guillet et al (22), in which the dissociative adsorption of ethyl isocyanate on silica, and n-butyl isocyanate on alumina and silica, were investigated. Intense infrared bands at 2300 cm^{-1} on silica (21, 22) and 2270 cm^{-1} on alumina (22) were identified as belonging to the isocyanate species.

II. EXPERIMENTAL SECTION

A. Apparatus

The apparatus used for this study consisted of a gas feed system for mixing and controlling reactant flows, a backmix reactor, and an analysis system consisting of two gas chromatographs in series coupled to an automated digital data acquisition system. A more detailed description of this equipment is presented below.

1. Gas Feed System

A schematic of the gas feed system is shown in Figure 1. Feed to the reactor originated from one of two main subsystems, designated as system A and system B. A gas stream from each could be fed independently to the reactor or vented, without disturbing the other's status. System A was used primarily for the blending of feed mixtures, while System B was used for purge and and in situ catalyst pretreatment. This arrangement was especially useful in that the reactor could be purged without disturbing the steady state status of system A.

Feed system A is made up of four independent sections which can be used to make mixtures of up to four components. Only three of the sections were used in this study. The gas in each section is passed through a glass capillary tube and the pressure drop across the tube measured by a manometer filled with silicon diffusion pump oil. The pressure in each section was held above atmospheric (nominally 15 to 30 psig) to prevent leaks into the system. The pressure and flow rate were controlled by metering needle valves before and after each capillary. A shut-off valve was connected in parallel with each

Figure 1.   Schematic of gas feed system
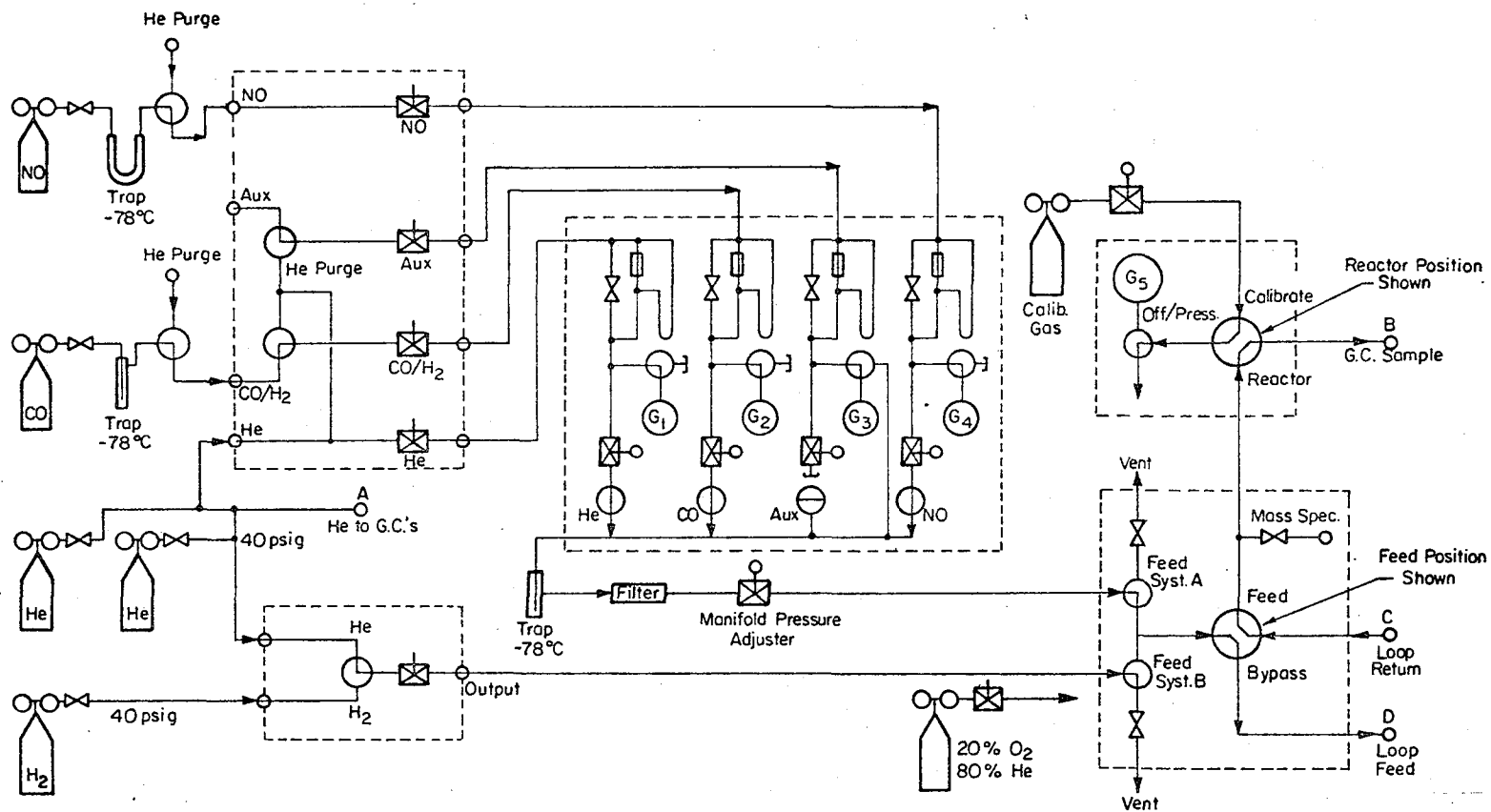
FLOW CONTROL AND FEED SYSTEM

XBL784-4813

Fig. 1

capillary as a bypass to prevent surges from overloading the manometers during start up and shut down.

Under operating conditions, the gas flow in the capillary tubes is laminar and the pressure drop is proportional to the volumetric flow rate. Each component section was calibrated by measuring the volumetric flow rate and pressure drop though each capillary using He. Correction for the individual components was made using gas viscosity data, based on the Hagen-Poiseuille law. The error associated with the flow measurement of each component was approximately 2%, and was due mainly to the error of the pressure gauges used to measure the total pressure in each capillary. Details relating to the calculation of flow rates can be found in Appendix 1.

The component streams were mixed in a manifold and the total stream was passed through a metering needle valve. This valve was used to keep the manifold pressure at 7 to 8 psig in order to minimize leaks and isolate the capillary flow systems from downstream pressure fluctuations. Prior to this valve, the gas mixture was passed through a dry ice/trichloroethylene trap and a sintered stainless steel 15 micron filter. This was done to insure that oil vapor (from the capillary manometer tubes) would not to be fed to the reactor.

A four way ball valve was used to control the feeding or bypassing of the reactor. In the FEED position this valve routes the selected feed system (A or B) to the input of the recycle loop, and the exit stream from the loop is routed to the chromatographic analysis train. The BYPASS position of this valve shorts the loop input and exit streams, while routing the feed stream directly to the analysis train.

2. Reactor and Recycle Loop

The reactor was connected to a gas recycle loop (Figure 2)
containing two preheaters located upstream of the reactor and a forced
air cooled tubing coil immediately downstream of the reactor. Gas flow
in the loop was provided by a stainless steel bellows pump with a nominal
volumetric flow rate of 40 liters/min. Total volumetric feed rates to
the recycle loop were nominally 200 cm^3/min, which results in a recycle
ratio of approximately 200:1. Under these conditions the reactor/recycle
loop behavior closely approximates that of a constant flow stirred tank
reactor (CFSTR).

The preheaters were made of 1/4" o.d. aluminum tubing (alloy T6061),
30" long, wound axialy in a helical groove cut in the surface of a solid
copper cylinder. The 1/4" width groove was round bottomed (1/8" radius)
for good surface contact with the tubing. Heating was provided by a
cylindrical cartridge heater inserted in the center of the block. The
preheaters were designed to heat the entire recycle stream per pass, to
avoid operation of the bellows pump at the elevated reaction temperatures.

Tubing in all hot sections of the recycle loop was made of T6061
aluminum in order to minimize blank activity problems encountered
with stainless steel tubing. Connections between aluminum preheater
sections were welded, however a problem was encountered in mating
the aluminum tubing to the stainless steel fittings on the reactor.
A special fitting had to be developed for this purpose, since no
commercially available fitting tested would remain sealed under temperature
cycling.

Figure 2. Schematic of the reactor recycle loop
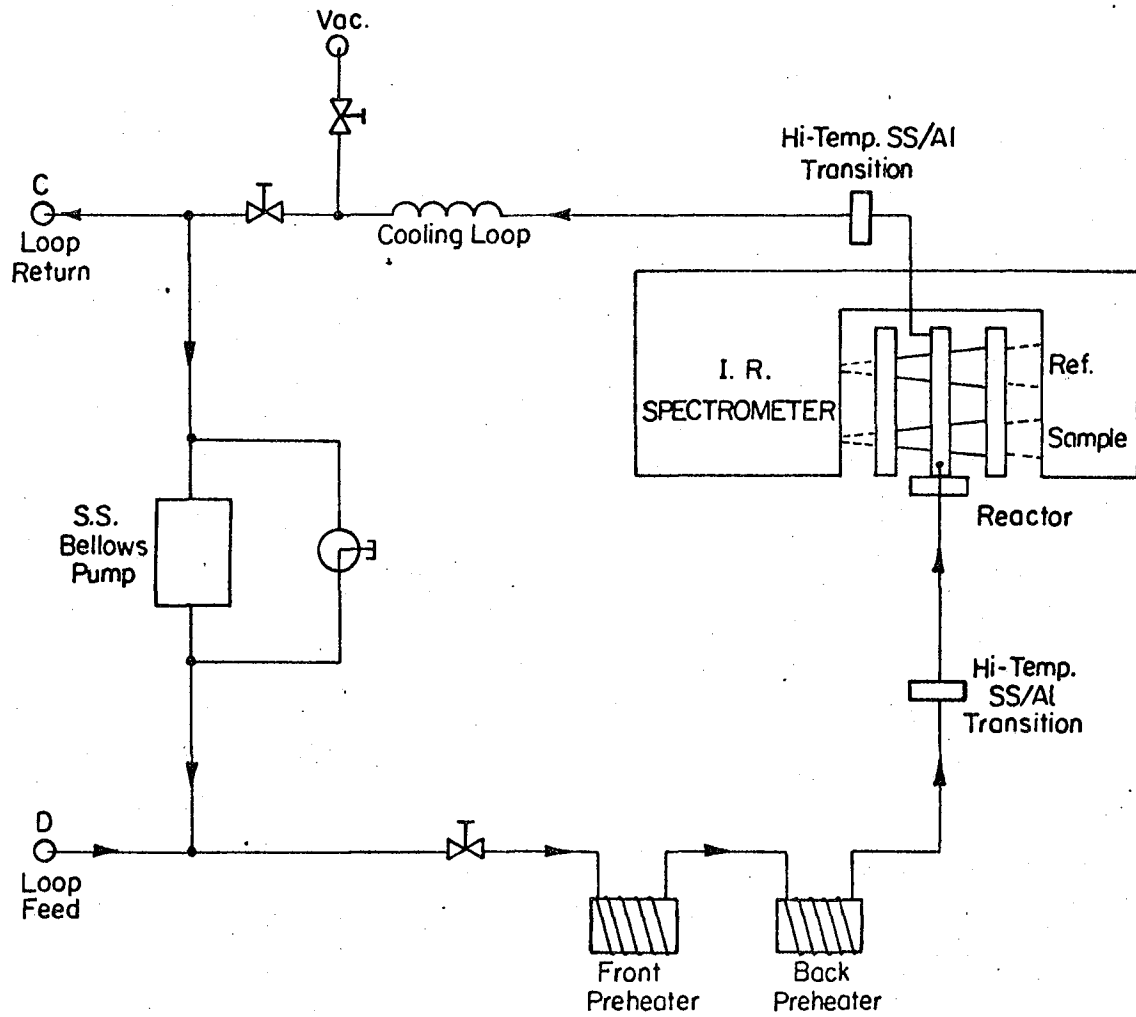
DIFFERENTIAL REACTOR RECYCLE LOOP

XBL 784-4814

Fig. 2

With 250 watt cartridge heaters installed in the preheaters, temperatures in excess of 400°C could easily be reached. This was the maximum practical limit, since the annealing point of the aluminum tubing is about 400°C, and significant softening becomes a problem at higher temperatures. Operation of only one preheater was sufficient to preheat the gas to a 300°C reaction temperature. The feed line between the preheaters and the reactor input was traced with a heating tape to minimize heat losses and provide a means for fine adjustment of the inlet gas temperature. Power for the heaters was provided by manually controlled variacs. A schematic of the power distribution system is shown in Figure 3.

Temperature measurement was made using chromel-constantan thermocouples distributed throughout the system. The output voltage of the thermocouples was fed to a digital panel meter which was capable of displaying either voltage (in mv) or temperature (in °C). Thermocouple location and switching circuitry, including the digital panel meter, are shown in Figure 4.

The reactor used for these studies was designed to allow infrared spectra of the catalyst to be taken under reaction conditions. This reactor was situated in the sample cavity of a Perkin-Elmer 457 infrared spectrometer and is shown schematically in Figure 5. The reactor was aligned so that converging sample and reference beams pass through the conical channels of the reactor, perpendicular to the catalyst and reference infrared disks and gas flow channel. Each of the beam channels was sealed via IR transparent windows and Viton 0-rings. The windows and 0-ring seals were maintained near room temperature

Figure 3. Schematic of heating power distribution system
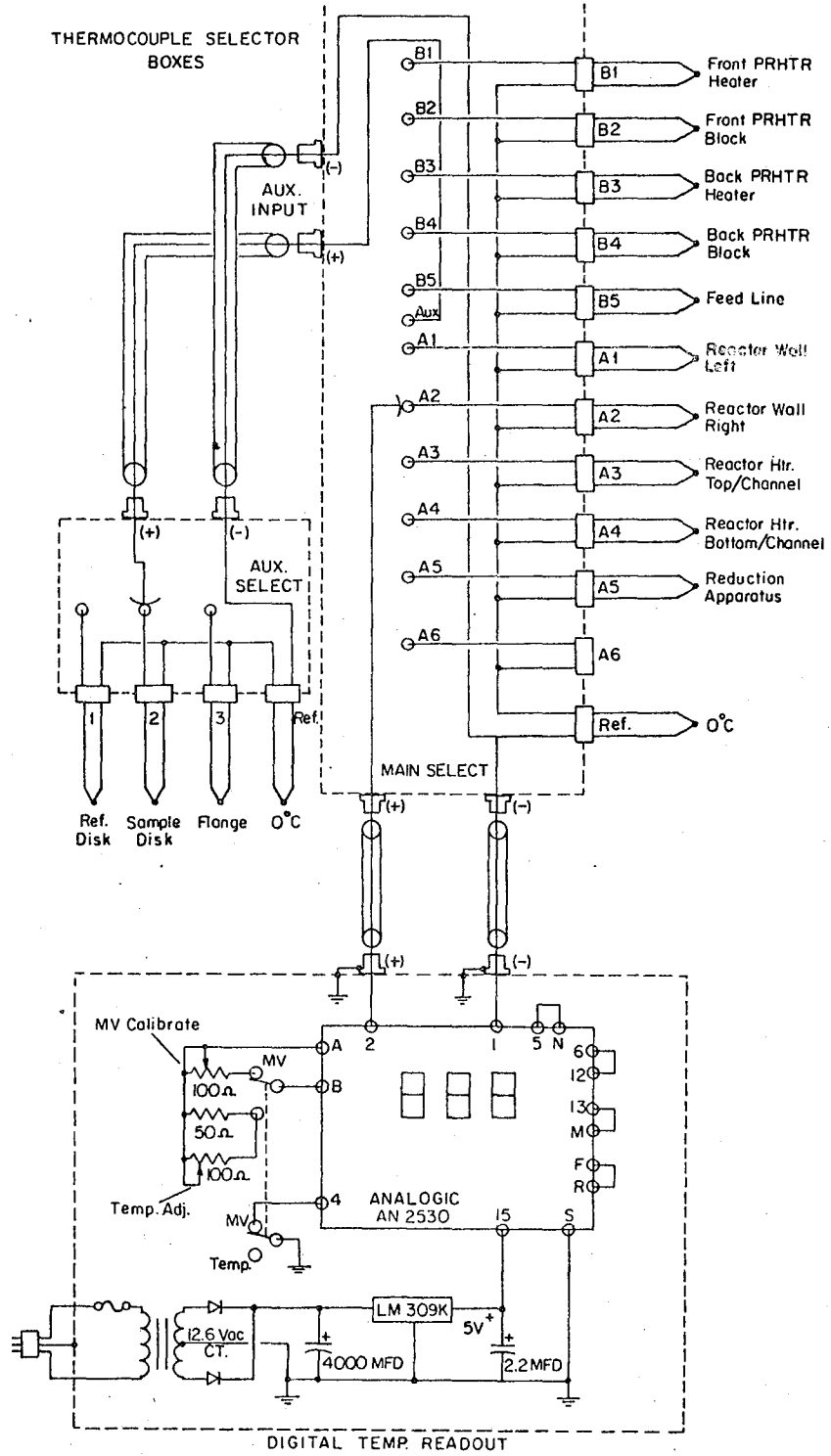
Fig. 4

Figure 5. Schematic of reactor

Reference
I R Beam

Sample
I R Beam

Top View
Mid Cross-section
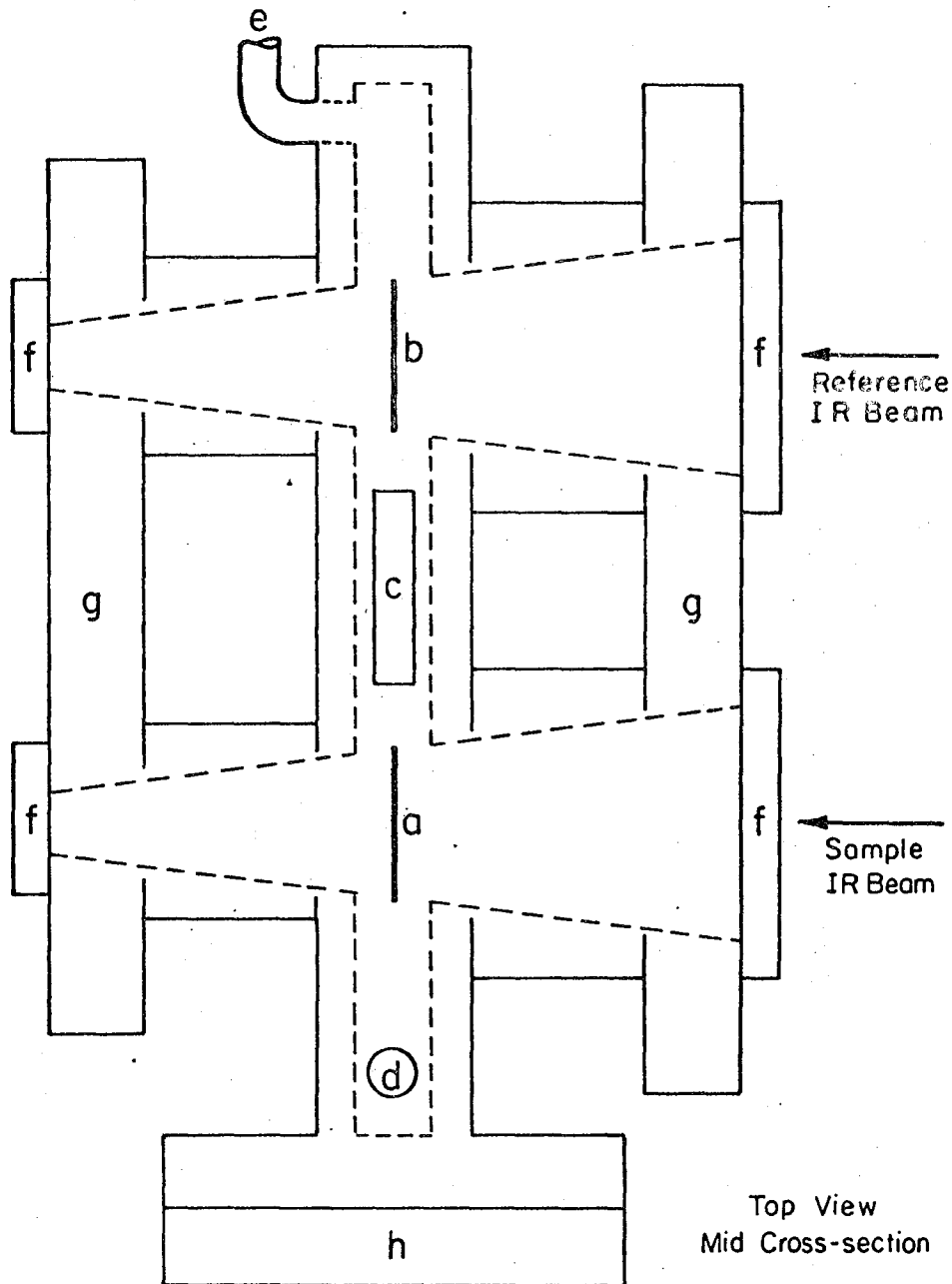
a	Catalyst Disk	e	Gas Outlet
b	Reference Disk	f	I R Windows
c	Center Holder	g	Water Cooled Flanges
d	Gas Inlet	h	Sealing Flange Assembly

REACTOR SCHEMATIC

XBL 784-4815

Fig. 5

by cooling water circulated through the slabs to which the windows were attached. The windows used in initial experiments were crystalline KBr, however these proved to be impractical due to frequent breakage. Both CaF_2 and polycrystalline NaCl were used for subsequent experiments.

A rectangular channel (1/2" x 1-1/2" x 7") milled in the central section of the reactor served as the primary reaction chamber containing the catalyst. Passage of gas through the reactor was facilitated by ports at both extremes of the channel. Sealing of the channel was accomplished by a weld seal at one end and a removable flange system at the other.

Heating of the channel was accomplished by cartridge heaters inserted in the top and bottom channel walls. Thermocouples were mounted outside the reactor on the channel walls to monitor wall temperatures. The sealing flange system was heated (to balance temperature gradients) by a fiberglass insulated heating tape wound around the flange circumference. Gas phase temperatures in the channel were limited to a maximum of 320°C due to thermal gradients and heat loss to the water cooled window mounting flanges.

Catalyst insertion, removal and alignment in the infrared beams was provided by mounting the catalyst to an assembly rigidly fixed to the removable sealing flange. This track assembly was inserted in the reactor channel during operation and is shown in Figure 6. The 1" diameter infrared catalyst and reference disks were mounted on this assembly via disk holders attached with small screws.

Between the disk holders an additional catalyst holder was placed, with an approximate capacity of 1 gram of catalyst. This holder

Figure 6.   Schematic of flange, track assembly, and

center catalyst holder

Sealing Flange

Disk Holders

Center Holder

Feed-throughs

Sample IR Disk

Reference IR Disk

Thermocouple
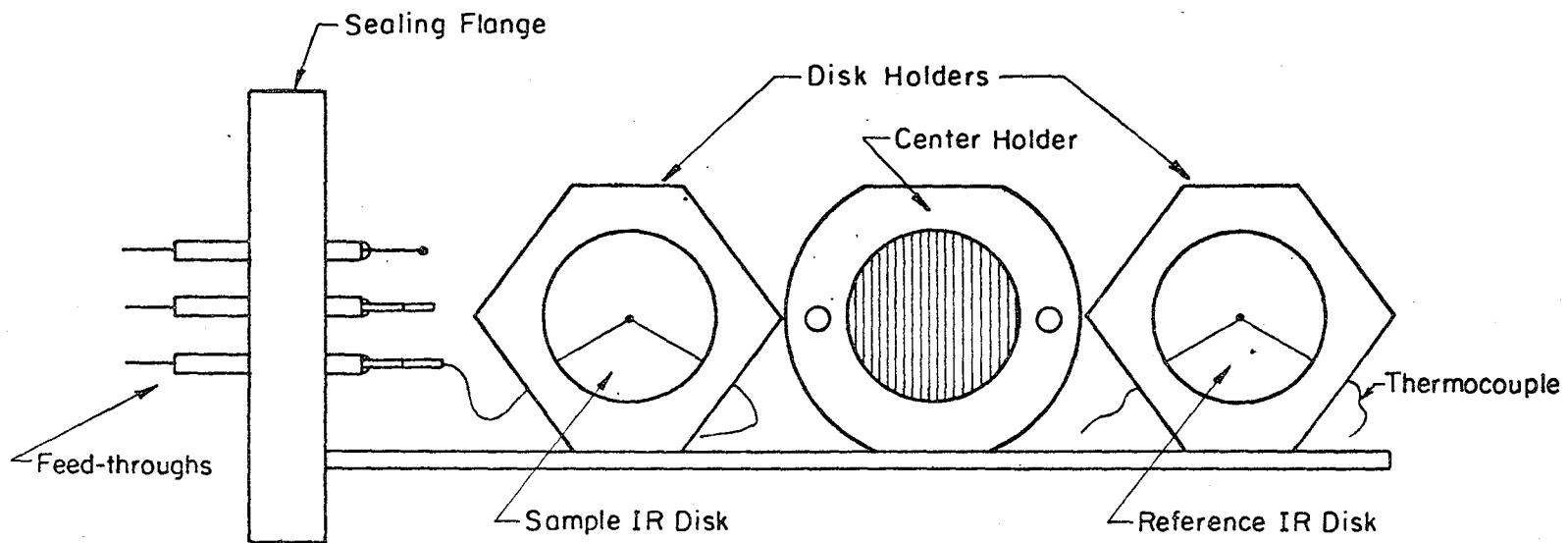
FLANGE AND TRACK ASSEMBLY

Catalyst Bed

Glass Cloth

Retaining Flange

Top View
Mid Cross-section

CENTER HOLDER

-22-
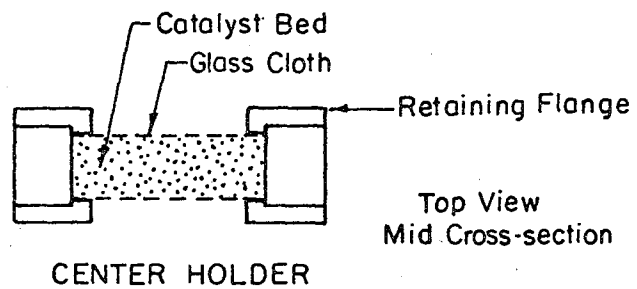
XBL 784-4816

Fig. 6

provided a cylindrical bed 1" in diameter and 1/4" deep. Containment of the catalyst was provided by fiberglass cloth stretched across both circular faces of the bed. When installed in the reactor channel, gas flow is parallel to the circular faces of the bed. Calculations indicated that bed diffusion would not be a problem for the feed rates studied. Bed permeability was aided by the significant channel blockage caused by the center holder, causing high gas velocities and turbulence at the bed faces. The pulsatile nature of the flow resulted in additional pressure fluctuations and turbulence.

The track assembly was attached to a sealing flange containing electrically isolated, gas tight feedthroughs. These provided electrical access to the thermocouples mounted on the infrared disk holders, in close proximity to the disks. A third thermocouple was placed at the gas flow entrance to the reactor. The electrical feedthroughs were constructed by brazing a ceramic disk to 1/8" Kovar tubes placed through holes drilled in the disk, then brazing the disk to the stainless steel sealing flange. Pin connectors and thermocouple wires silver soldered to the Kovar tubes completed the seal.

All parts of the track assembly (omitting feedthroughs and thermocouples), sealing flange, and reactor cell were machined from 304 or 316 type stainless steels. These parts were electroless nickel plated to remove surface roughness prior to the application of a special ion plated aluminum coating, described below.

Aluminum Coating

Because stainless steel is known to be active for the catalytic
reduction of NO by CO, the acquisition of rate data in a steel reactor
may be complicated by high background activity. This activity makes
it difficult to study the NO-CO system in apparatus constructed of
stainless steel. Peterson and coworkers (23) have shown that continual
cyclic oxidation and reduction of the stainless steel surface promotes
surface cracking and spalling. This cracking and spalling contributes
to a significant increase in the surface area of the steel. Initial
experiments performed with the reactor described here showed that
the blank activity could be quite significant and result in as much
as 40% NO conversion.

In the light of these problems, a considerable amount of effort
was expended to reduce the blank activity of the apparatus. Due to
the highly specialized construction of the reactor, it was considered
impractical to build a duplicate unit from another material. There
are very few materials that have the desired corrosion resistance,
machinability, weldability, mechanical strength, and are non-catalytic
as well. It was decided, therefore, that the most practical approach
would be to find a catalyticly inactive coating for the internal surfaces
of the reactor. An ideal coating should be: (1) noncatalytic, (2) stable
at temperatures up to 450°C in both oxidizing and reducing atmospheres,
(3) have low Cr, Ni, and Fe solubility to inhibit diffusion of these
metals to the surface, (4) be nonporous to prevent significant gas
diffusion to the underlying steel, (5) have low solubility in stainless

steel to prevent eventual loss of the film, (6) be physically durable
and (7) easy to apply.

Gold plating was considered due to the inert nature of gold,
however test strips of gold plated stainless steel showed very poor
high temperature stability. This can be explained by noting that
in order to electroplate gold on stainless steel, the steel must first
be plated with nickel and then copper, since the gold will not adhere
to the steel surface directly. As the temperature of the Au/Cu/Ni
plate is raised, the metals interdiffuse and a surface of copper oxide
is formed. The rate of diffusion is extremely slow at room temperature,
but increases rapidly at higher temperatures as a result of the ex-
ponential dependence of the diffusion rates on absolute temperature.
Calculations indicated a diffusion time constant of approximately
1 hr for a 1 mil (0.001 in.) thick Au/Cu plate at a temperature of
300°C. This time constant was confirmed by experiment.

One material which meets the ideal coating criteria quite well
is aluminum. Aluminum films form dense Al_2O_3 surfaces (24) that exhibit
low catalytic activity, excellent resistance to oxidizing and reducing
atmospheres at high temperatures, and good adhesion to stainless steel.
Aluminum has a low solubility in stainless steel, and Fe, Cr, and
Ni all have very low solubilities in aluminum. In addition, aluminum
is an easy material to apply by either vapor deposition or ion plating.
Since ion plating is capable of covering intricate shapes, this method
was selected.

The stainless steel parts to be coated were cleaned and electroless
nickel plated to help smooth any surface roughness. Two 2000Å ion

plated aluminum coatings were applied, with an oxidation step following the first coating and preceding the second. The purpose of the oxidation was to provide a diffusion barrier of Al_2O_3 to prevent diffusion of the top protective coating into the steel bulk. This barrier also prevents diffusion of any Fe, Ni, or Cr to the surface. It is beyond the scope of this work to give a detailed description of the ion plating process itself. However, a brief description is in order. The parts to be plated are placed in a vacuum chamber and charged to -1000 volts in the vicinity of a hot aluminum filament at ground potential. Aluminum ions leaving the filament are accelerated into the steel surface, resulting in good adhesion and dense coverage. After the application of the second coating, the coated steel parts were placed in an air oven at 400°C for 200 hr to grow a dense γ-Al_2O_3 crystalline film (24).

3. Analysis System

Analysis of the gas phase compositions was accomplished using two gas chromatographs connected in series. This approach made it possible to obtain a clean separation between NO, CO, N_2, N_2O, and CO_2 without the use of cryogenic temperatures or temperature programming. A schematic of this system is shown in Figure 7.

The first chromatograph (GC1) contained a Poropak R column to separate N_2O and CO_2. The components NO, CO, N_2 were eluted from the Poropak R column as a single unresolved peak prior to N_2O and CO_2. The combination peak was resolved in the second chromatograph (GC2) which contained a 5Å molecular sieve column. Column operating conditions are given in Table 1. Column temperatures were adjusted to prevent overlapping of N_2 (first peak from GC1) with N_2O (last

Figure 7.   Gas flow schematic for the chromatographic

analysis system
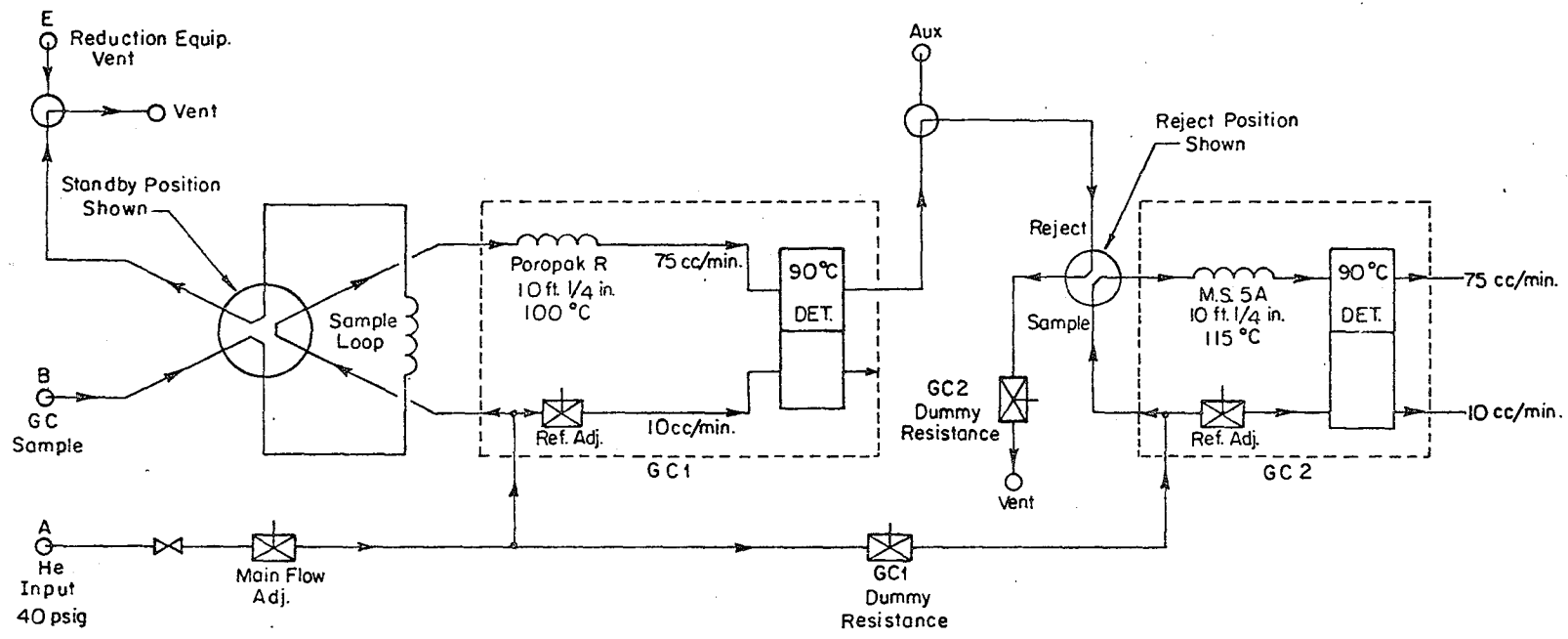
GC ANALYSIS TRAIN

XBL 784—4817

Fig. 7

-28-

Table 1. GC Column Operating Conditions

	GC1	GC2
Packing material	Porapak R	Mole Sieve 5A
Column dimensions	10 ft x 1/4" od stainless tubing	10 ft x 1/4" od stainless tubing
Column temperature	$100^{\circ}C$	$90^{\circ}C$
He carrier flow rate	75 cc/min	75 cc/min
Filament current	250 mA	250 mA
Detector temperature	$90^{\circ}C$	$90^{\circ}C$

peak from GC2), since only the one detector output could be observed at a time. Valving between the chromatographs was necessary to prevent the components CO_2 and N_2O from entering the mole sieve column and irreversibly adsorbing. This function was performed by a two position four-port ball valve. In the SAMPLE position the effluent from the Poropak column is introduced directly into the mole sieve column. After the passage of the combination (CO, NO, N_2) peak through GC1, the ball valve is manually switched to the REJECT position which vents succeeding components from GC1 while simultaneously providing He carrier flow for the column in GC2. Since thermal conductivity detectors are sensitive to carrier flow rate, needle valves were used to provide identical (within 1%) carrier flow rates for each column in both valve positions. A two position six-port sampling valve was used to fill and inject the contents of the sampling loop. In the STANDBY position, the sample stream is directed through the sample loop and then vented, while He carrier gas is routed directly to the column. In the SAMPLE position, the carrier stream purges the contents of the sample loop into the column, and the sample stream is vented.

The output of the chromatograph detectors (0 to 1 mV) was amplified (to 0 to 10V) and then fed to a chart recorder and a data acquisition system (Figure 8). The data acquisition system has been described elsewhere (25) and shall not be discussed.

Initial calibration of the chromotagraphs was performed using Primary Standard Certified gas mixtures obtained from Matheson. Three separate mixtures of N_2O, CO_2, and N_2 in He ranging in concentration from 0.5 mole% to 5.0 mole % per component were used (0.5% each CO_2,

Figure 8. Electrical signal processing schematic for

the chromatographic analysis system

Fig. 8

N_2O, N_2 in He). Calculation of the sample component concentrations was made by computing peak amplitudes from the digital printout and ratioing these to peak amplitudes obtained during calibration. Reproducability using the peak height method was within 1%. Quantitative analysis was not attempted for NO and CO due to difficulties in obtaining a reproducable separation in the mole sieve column. Calibration could be performed with reasonable reproducability for either NO or CO separately, but the response for NO-CO mixtures was often erratic. NO and CO compositions in the reactor product stream were determined by mass balance after analysis for N_2O, CO_2, N_2.

B. Procedures

1. Catalyst Preparation

The catalyst used in this study was a high dispersion platinum catalyst supported on silica. Two types of silica were used to support the Pt, corresponding to the different requirements of the two catalyst positions in the reactor. Catalyst in the center holder was supported on silica gel (Davidson type 70, -80+150 mesh), while catalyst making up the IR disk was supported on fumed silica (Cabot type HS-5 Cabosil). The preparation procedure was essentially the same for both types of silica support, and was based on the platinum ammine ion exchange technique described by Boronin et al (27) and Benesi et al (26). The heart of this process involves contacting the silica support with a platinum ammine solution at high pH ($\geqslant 9$).

To obtain the desired Pt catalyst loading of approximately 4 wt. %, 110 ml of a previously prepared chloroplatinic acid solution (4.988 gm $H_2PtCl_6 \cdot 6H_2O$ in 500 ml distilled H_2O) was added to 265 ml distilled

Figure 9.   Catalyst reduction apparatus
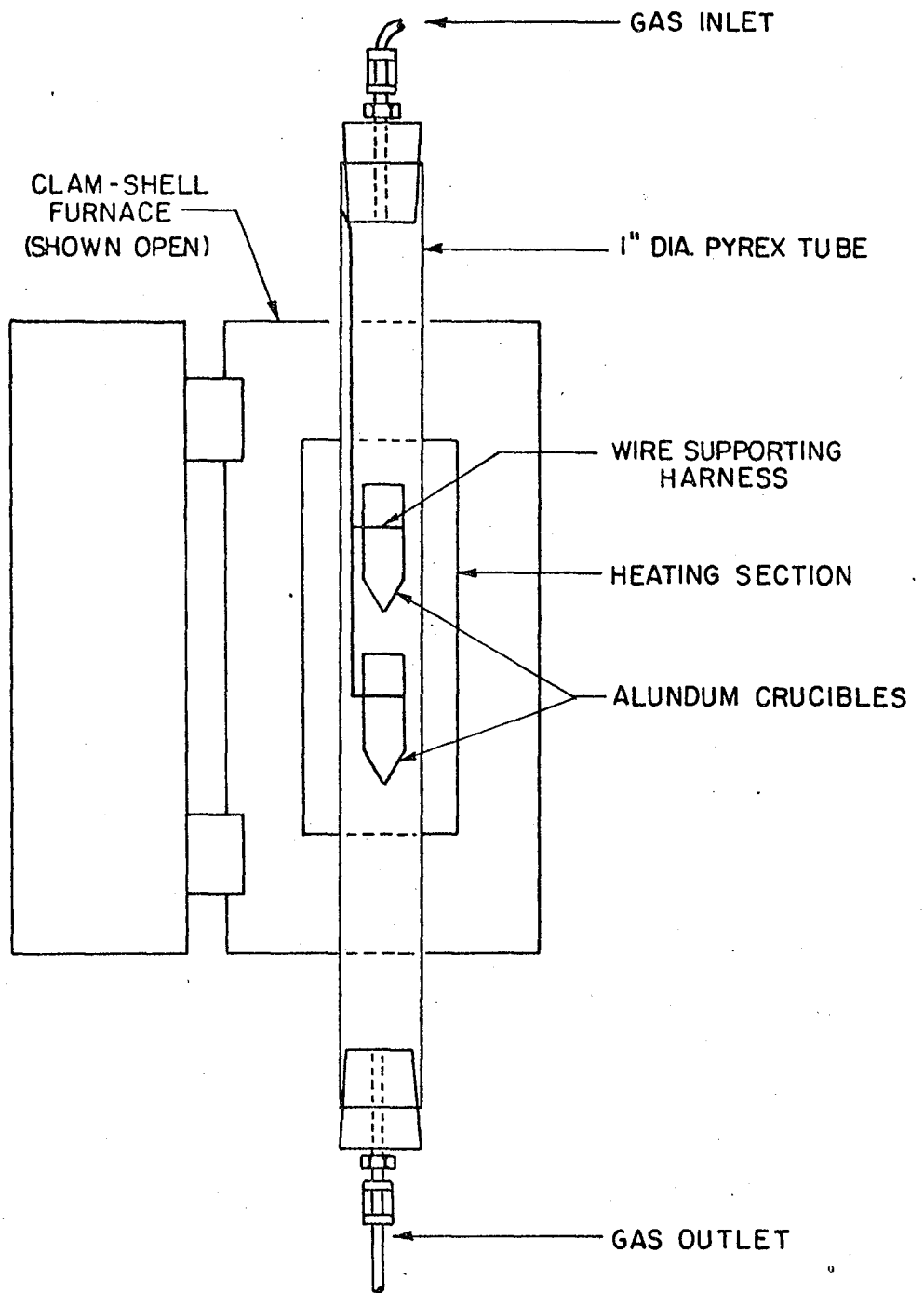
REDUCING APPARATUS

XBL 785-5070

Fig. 9

The reduction procedure was also carried out with the Cabosil
IR reference disk material, in order to remove any chlorine remaining
after manufacture.

The reduced catalyst was sieved in stainless steel screens by
mechanical vibration. The Cabosil supported catalyst and reference
material was sized to -325 mesh, and the silica gel supported catalyst
was sized to -80+150 mesh.

2. IR Disk Preparation

The catalyst was pressed into thin disks or wafers in order to
perform transmission infrared spectroscopy. This was accomplished
by compressing the finely powdered, supported catalyst in a steel
die at high pressure.

Many variables were optimized in this process in order to yield
disks of good infrared transparency and durability. The type of silica
support, mass of the disk, pressing procedure and pressure, and die
material and construction, all had an effect on the resulting IR disks.

Concerning the type of support, it was found that Cabosil disks
had better IR transparency than silica gel (-325 mesh) disks when
pressed under the same conditions.

The mass of the disk was optimized with respect to two competing
effects. Heavy disks contain more catalyst, and are desirable since
observed IR bands are more intense, and smaller amounts of an
adsorbed species are detectable. However, higher mass disks have
poorer transparency since they are thicker, and this is not desirable
since spectrometer response is sluggish leading to a corresponding
loss in resolution. If the disks are too light, they will break or

crack easily and are difficult to handle. The optimum mass was determined to be in the range of 160 to 200 mg.

The die used in this study was similar in design to that used by Ludvik (9), and was constructed of case hardened tool steel. The die faces were surface ground flat and parallel. Experimentally it was found that the tool steel die would produce durable, transparent IR disks at much lower pressures than the stainless steel die used by Ludvik. The die is shown schematically in Figure 10.

The disks were pressed at the lowest pressure consistent with acceptable IR transparency and good physical durability. High pressures yield disks of good IR transparency and physical durability, but there is a possibility that these disks may have poor mass transfer characteristics due to a "skin" produced at high compression. After loading approximately 200 mg in the die assembly, the pressure was raised to a maximum of 7700 psi (on disk) over a period of 3-4 minutes. This pressure was held for 6 to 7 minutes and then released gradually over a period of 8 to 10 minutes. Releasing the presence at a faster rate resulted in puckered and cracked disks.

Three catalyst disks and three reference disks were made and used in this study. The catalyst disks (designated C1, C2, and C3) weighed 168 mg, 157 mg, and 160 mg, respectively. The reference disks (designated R1, R2, and R3) weighed 203 mg, 171 mg, and 166 mg, respectively. Each of the three catalyst disks (as well as each of the three reference disks) were used interchangeably in later experiments.

Figure 10. Die for pressing catalyst disks

1-1/8"
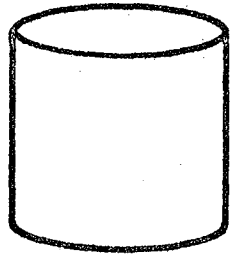
Piston
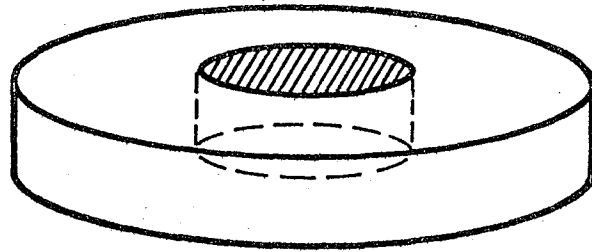
Ring
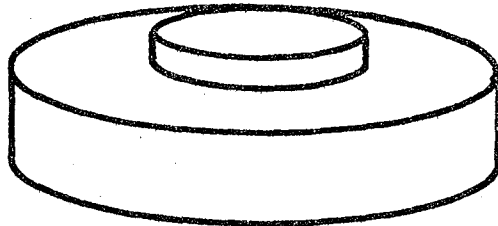
Base

XBL 786-9314

Fig. 10

3. Catalyst Characterization

Properties of the silica supported platinum catalyst used in this study are shown in Table 2. Also shown are the properties of the catalyst used by Ludvik (9) for comparison. Several analyses were performed in order to characterize the catalyst, including X-ray fluorescence, hydrogen chemisorption, and a semi-qualitative spectrographic analysis for trace metals.

Platinum weight loadings were determined by X-ray fluorescence and are accurate to ±5%. This analysis was performed by Mr. Bob Giaque at the Lawrence Berkeley Laboratory.

Metal surface area was determined by hydrogen chemisorption, performed by Pacific Sorption Service. Dispersion was calculated by multiplying the hydrogen chemisorbed (micro-moles/gm catalyst) by 2 and dividing by the total platinum present (micro-moles/gm catalyst). As can be seen in Table 2, dispersions are very high and in good agreement with the dispersion reported by Ludvik.

The average crystallite size was estimated from:

$$D = \frac{2n^2 + (n-2)(3n-2)}{n^3}$$

where: D = dispersion

n = # of Pt atoms per side of crysallite

In deriving this equation, a simple cubic lattice was assumed, and the crystal was assumed cubic as well. Corner atoms were counted only once in accounting for surface area, and it was assumed that the crystal is resting on a planar surface with five sides exposed to the gas phase. The equation predicts, for a catalyst of 90% dispersion,

Table 2. Catalyst Properties

	Batch #1	Batch #2	Batch #6	Ludvik
weight loading,%	4.57 ± 0.23	4.25±0.21	4.68±0.23	3.00
support	HS-5 Cabosil	Davidson 70 silica gel	Davidson 70 silica gel	M-5 Cabosil
hydrogen chemis. μmoles/g	106	100	101	69
dispersion	90%	91%	84%	90%
avg. crys. size, Å	14	14	15	17

that an average crystallite will contain between 3 and 4 Pt atoms per side. Assuming a diameter of approximately 4Å per Pt atom, the average crystallite size would be between 12 and 16Å. These estimates were not verified by direct measurement, however the estimates are in good agreement with the average crystallite size determined by electron microscopy in Ludvik's study.

4. Preliminary Experiments

Initial experiments were performed to determine the range of conditions which would yield accurate and reproducible kinetic information. These experiments were primarily concentrated in two problem areas: 1) minimizing the effect of reactor background activity and 2) obtaining consistent and reproducible catalyst activity from run to run. It should be noted, in the light of future discussion (see Results section), that initial experimentation was carried out under highly reducing $(P_{CO} > P_{NO})$ conditions. As a result, operating parameters were chosen with respect to the lowest catalytic activity and "worst case" conditions.

In order to minimize background activity, experimental results indicated that it was desirable to place as much catalyst in the reactor as possible, and operate at the maximum allowable reaction temperature. High reaction temperatures preferentially increased the activity of the platinum catalyst, with respect to that of the reactor walls, due to the higher activation energy associated with the platinum catalyzed reactions. The maximum allowable reaction temperature was limited to 300°C, and all kinetic data reported in this study were taken at this temperature. Operation at temperatures below 300°C did not yield data of acceptable accuracy due to low kinetic activity.

The maximum amount of catalyst which could be placed in the reactor was limited to approximately 1.2 gm, including the infrared catalyst disk and the catalyst in the center holder. Experiments were performed using both the Cabosil and the silica gel supported catalysts in the center holder. No difference in activity was detected between catalysts on the two types of support. In addition, since the Cabosil supported catalyst was in the form of broken IR disks ($\sim 1/4$" diameter), these experiments indicated that the IR disks were free of mass transfer limitations. The silica gel supported catalyst was used in the center holder because the broken IR disks were prone to dusting. The silica gel did not exhibit this problem and was easier to retain.

After the operating conditions had been established, the problem of reproducibility was addressed. Initial results revealed that, for feed ratios of CO/NO >1, the catalyst exhibited a time dependent deactivation (see the Results section for a more complete discussion on this point). This indicated that the catalyst was undergoing some type of poisoning, and a pretreatment procedure was developed to restore catalyst activity between runs. A pretreatment of a 2 hr oxidation (in 20% O_2 in He) followed by a 5 hr reduction (in H_2) at 300°C was found to restore the initial activity reproducibility. This pretreatment preceded every kinetic run unless otherwise noted.

The rather lengthy pretreatment procedure appeared to have no effect on the dispersion of the catalyst. This was determined by observation of the CO IR band. Under high CO partial pressures, a large percentage of the platinum surface will be covered with adsorbed CO. Since many of the experiments were run under high CO partial

pressures (5 to 70 torr), one would expect to see a change in the CO infrared absorbance over a series of runs if the catalyst surface area was changing significantly. Only small changes were noted, none of which were permanent or irreversible.

A summary of experimental conditions and procedures is given in Table 3.

5. Blank Activity

Despite all the effort expended in coating the reactor, background activity was still found to be significant and could not be ignored when analyzing the kinetic data. The blank activity was found to be transient in nature, and exhibited a time dependent decay over the time period of a run (3 hr). In addition, operation of the reactor over a long time span with many pretreatment and run cycles resulted in a gradual increase in activity. This activity could be reduced by recoating the internal surfaces of the reactor.

Experiments were performed in an attempt to isolate the cause of the reactor activity. During the preliminary experimentation period, the blank activity had risen to very high conversions, as can be seen in Figure 11, curve a. Removal of the track assembly reduced the activity significantly (curve b) and recoating the walls and track assembly with Vacseal (Space Environmental Labs) reduced the activity still further (curve c). From these results it is clear that the largest contribution to the background activity was due to the track assembly.

The cause of the high track activity is not understood. Flexing of the track during handling and temperature cycling resulted in some

Table 3. Summary of Procedures and Conditions

Experimental Conditions

Reaction temperature: 300°C

Total feed rate: 200 cc/min (25°C, 1 atm)

Range of feed concentrations: 1.0 to 10.0 mole %, NO and/or CO in He

Catalyst: 4.5 wt% Pt/silica, 1.2 to 1.3 gm

Mode: Recycle reactor, recycle ratio = 200:1, nominal volume of 300 cc

Procedures

Standard Pretreatment

    1) Reactor preheated to 300°C in He

    2) Feed 20% O_2 in He for 2 hrs

    3) Purge with He for 30 min

    4) Feed H_2 for 5 hrs

    5) Purge with He for 1 hr

Kinetic Run

    1) At t=0, feed reactants mixture; NO and CO in He

    2) Sample outlet concentrations at t=5, 15, 30, 60, and 180 min

    3) Record IR spectra at t=30, 90, and 150 min

    4) At t=180 min, disconnect feed, purge with He

Figure 11. Blank conversion as a function of time during preliminary

experimentation. Curve a: activity of track assembly

and reactor walls prior to recoating, curve b: activity

of reactor walls after track removal, curve c: activity

of track assembly and reactor walls after recoating with

Vacseal. Feed composition for all cases was %10 CO,

5% NO in He. Temp. = 300°C.
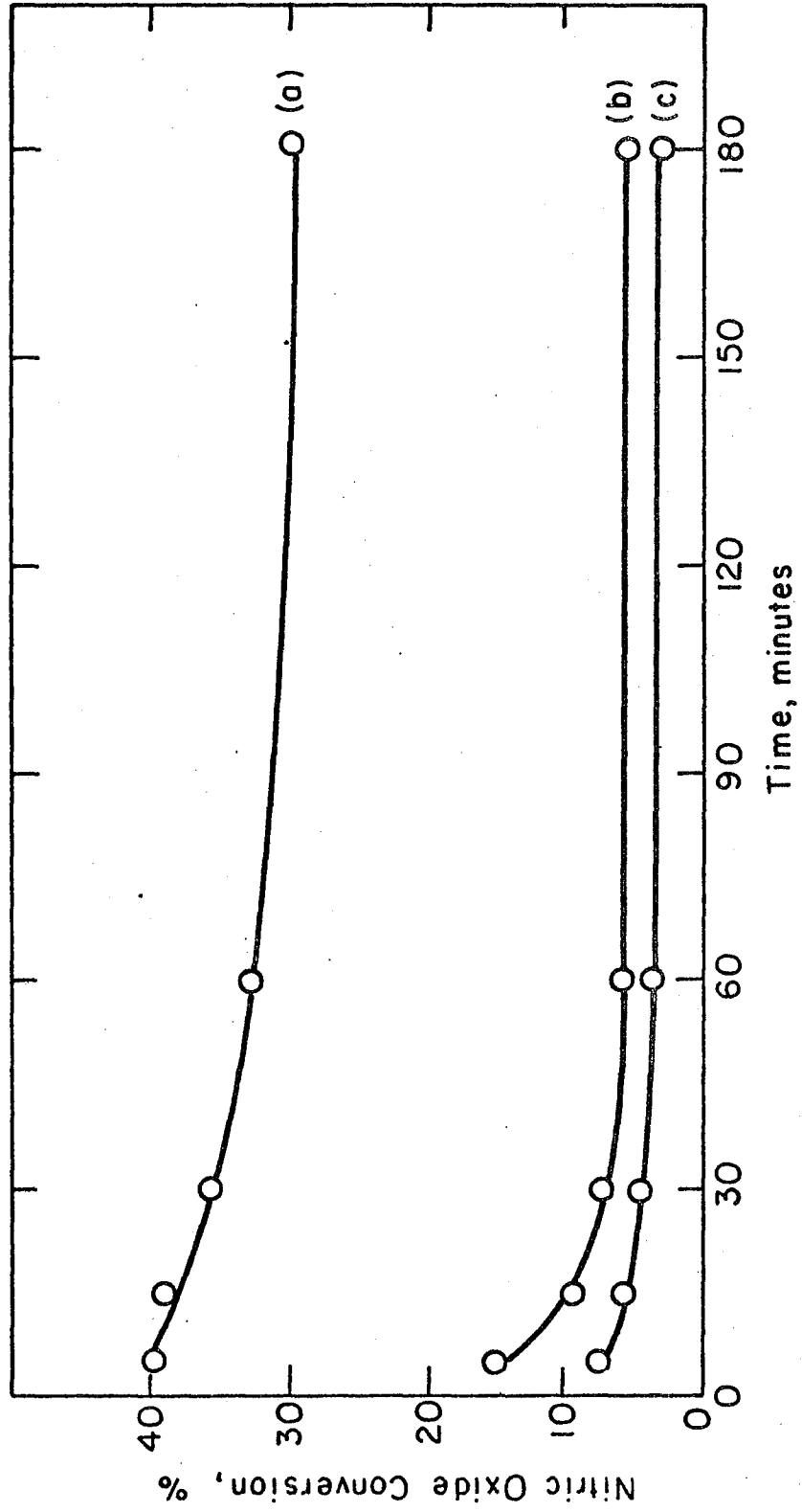
Fig. 11

XBL 785-5101

cracking and spalling of the aluminum coating. It is possible that the loss of integrity of the coating is responsible for the increase in activity, however the cracking did not appear to be severe, and it would be difficult to explain such a high degree of activity in terms of the small area of exposed steel. Impurities being fed to the reactor (such as metal carbonyls) were ruled out since they would probably decompose in the first hot section of the recycle loop they enter. This would cause a rise in activity of the preheaters, which was not observed. There is also no reason for a gas phase impurity to selectively decompose on or contaminate the track, unless perhaps it were being formed by the catalyst. There is, however, no evidence for the existence of such a species.

The transient nature of the blank activity required that the blank data be taken as close to the kinetic data as possible, and at the same concentrations, temperature, and pretreatment conditions. This was necessary in order to subtract the reaction rate contribution of the background, and obtain the true catalyst kinetic behavior.

Kinetic data was taken in a sequence of three or four runs before the corresponding blank data. Good reproducibility was obtained as long as the blank run sequence immediately followed the kinetic run sequence. This was done for convenience, since the reactor and recycle loop had to be cooled before catalyst removal, and reheated afterward. The lengthy heating and cooling period prohibited taking background data immediately after kinetic data for any given set of conditions in a single run.

It was not possible to duplicate kinetic run gas phase concentrations during the corresponding blank run, since this would involve a time consuming trial and error procedure due to the backmix nature of the recycle reactor. Instead, the blank data was corrected for the concentration differences by assuming a first order dependence of the reaction rate on NO concentration. This assumption was verified experimentally by comparing reaction rates for blank data at different concentrations. The background activity exhibited only a small dependence on CO concentration, and therefore no CO dependence was included in the corrections.

The behavior of the background activity over the course of kinetic runs reported in this study is summarized in Figure 12. This figure shows the corrected activity level for the background corresponding to the first and last experiments in the complete sequence of reported data (Runs KOR-20 to KOR-38).

Figure 12. Range of background activity for kinetic

data reported
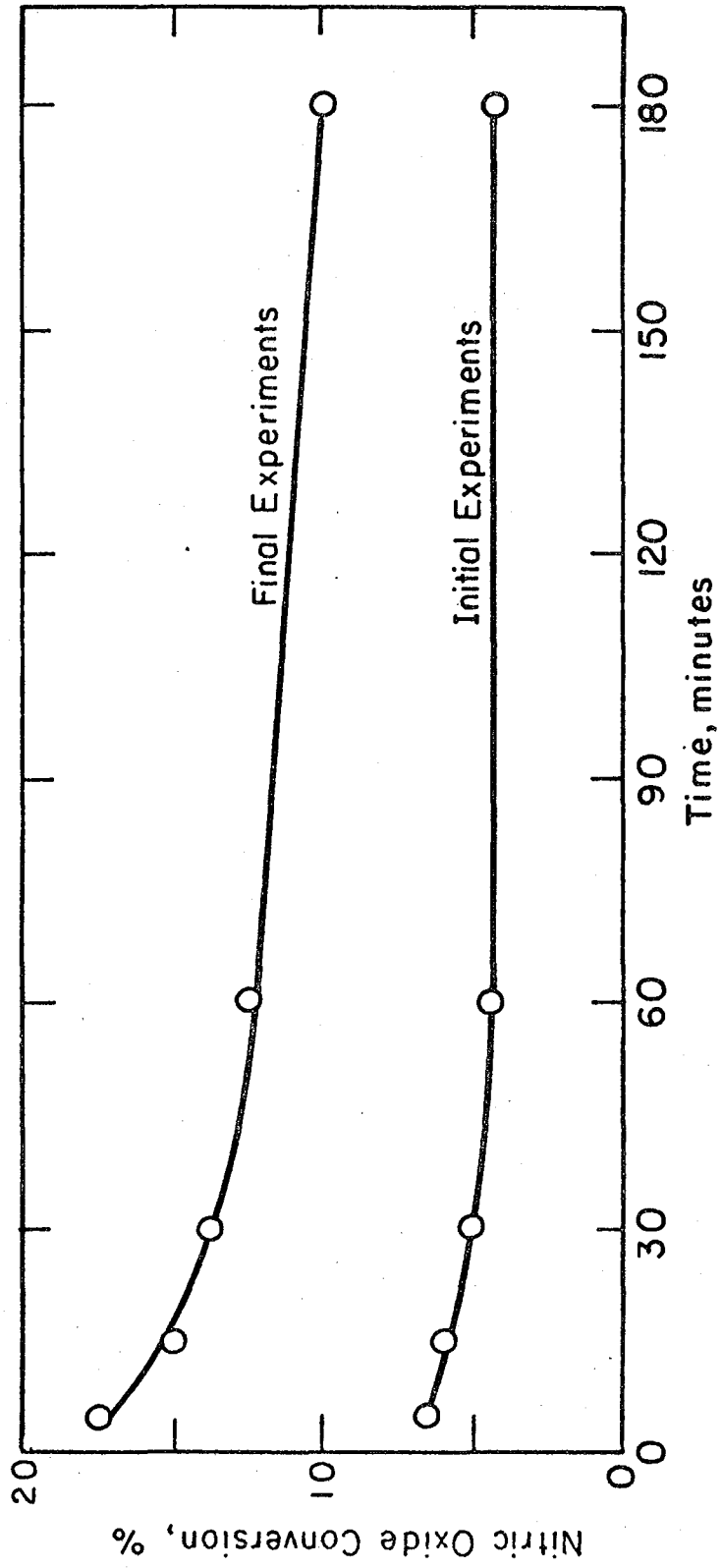
Fig. 12

XBL785-5102

III. RESULTS AND DISCUSSION

A. Introduction

The range of feed concentrations investigated in this study is shown in Figure 13. The kinetic behavior of the system was found to exhibit two distinct trends, depending on the ratio of the molar feed concentrations of NO and CO. Molar feed ratios of CO/NO greater than one shall be refered to as the reducing region (the region above the 1:1 line in Figure 13), and molar feed ratios of CO/NO less than one shall be refered to as the oxidizing region. Future discussion of results shall be organized with respect to these two regions.

The variables of interest in this study were reactant conversion, product selectivity and distribution, and the infrared spectra of the catalyst during reaction. Product selectivity and distribution were characterized by two parameters; nitrous oxide selectivity, S_{N_2O}, and the stoichiometric ratio, R_S, defined below:

$$S_{N_2O} = (R_{N_2O})/(R_{N_2O} + R_{N_2}) \tag{1}$$

$$R_S = (R_{N_2O} + 2R_{N_2})/R_{CO_2} \tag{2}$$

In the above equations, R_{N_2O}, R_{N_2}, and R_{CO_2} are the reaction rates of formation of the products N_2O, N_2, and CO_2, respectively.

R_S is derived from the stoichiometric relationships of the reaction products:

Figure 13. Range of feed concentrations

XBL 785-5072

Fig. 13

$$CO + NO \rightarrow CO_2 + 1/2N_2 \tag{3}$$

$$CO + 2NO \rightarrow CO_2 + N_2O \tag{4}$$
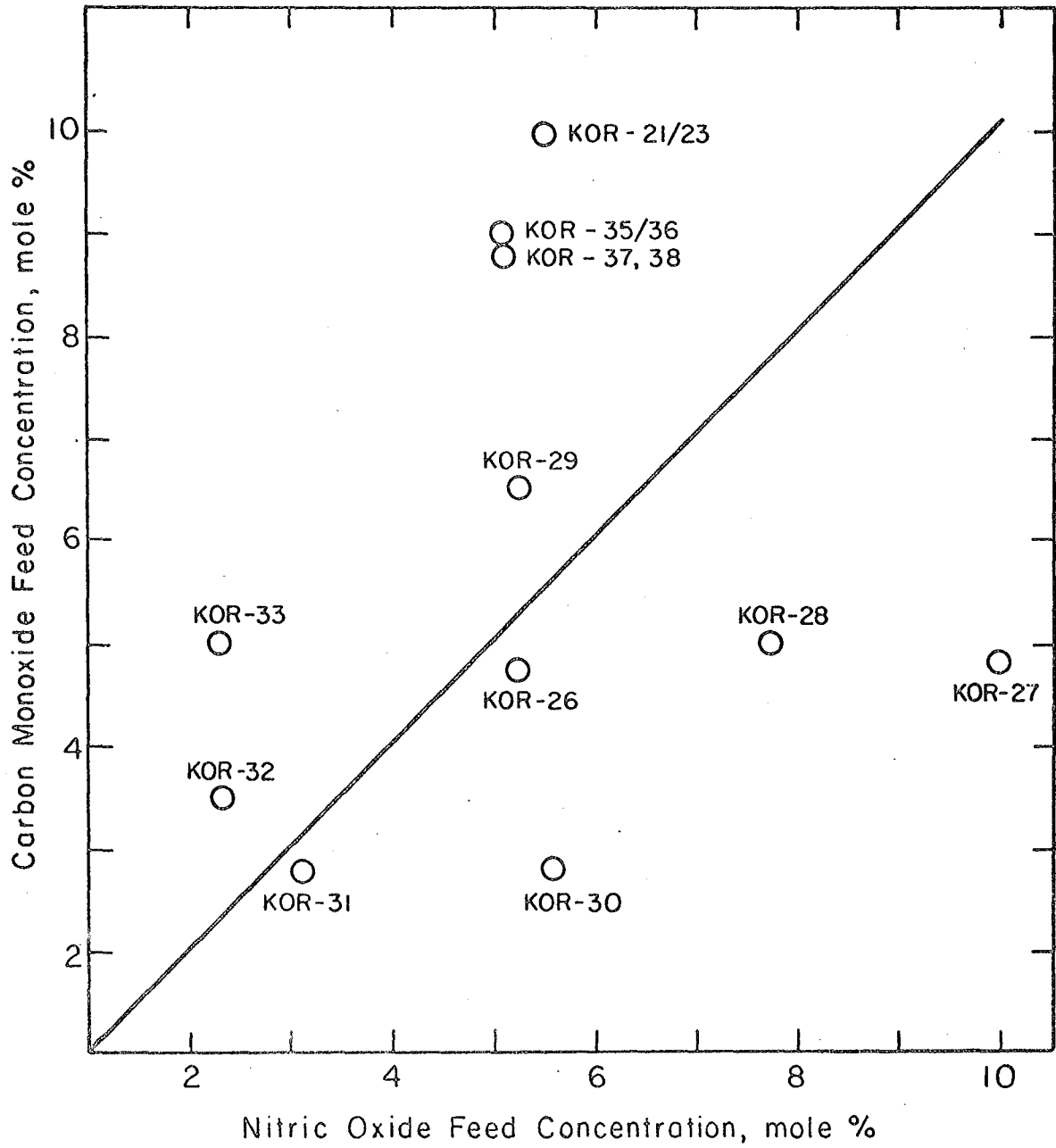
A value of R_s other than unity indicates the existence of a side reaction producing CO_2, N_2, or N_2O. Producton of excess nitrogen products results in a value of R_s greater than one. An example of such a side reaction would be the oxidation:

$$NO + M \rightarrow M-O + 1/2N_2 \tag{5}$$

Production of excess CO_2 would result in R_s values less than one, and an example of a side reaction producing CO_2 would be:

$$2 CO \rightarrow C_{(s)} + CO_2 \tag{6}$$

For values of R_s less than one, the excess CO_2 production rate can be determined from the definition of R_s:

$$R_{CO_2, \text{ excess}} = R_{CO_2} (1-R_s) \qquad R_s < 1 \tag{7}$$

where R_{CO_2} is the experimentally measured total rate of CO_2 production.

B. Kinetic Results

1. Reducing Region

Conversion as a function of time is shown in Figure 14 for runs made under reducing conditions. The accompanying reactor concentrations are given in Table 4. As can be seen in Figure 14, the catalyst exhibited a time dependent loss of activity, manifestd by a transient drop in conversion. The initial conversion level and the rate of decay of activity were functions of the NO and CO concentrations in the reactor. Run KOR-32 (refer to Figures 13 and 14) had the highest conversion

Figure 14. Nitric oxide conversion as a function of time for runs in the reducing region. Temperature = 300°C.
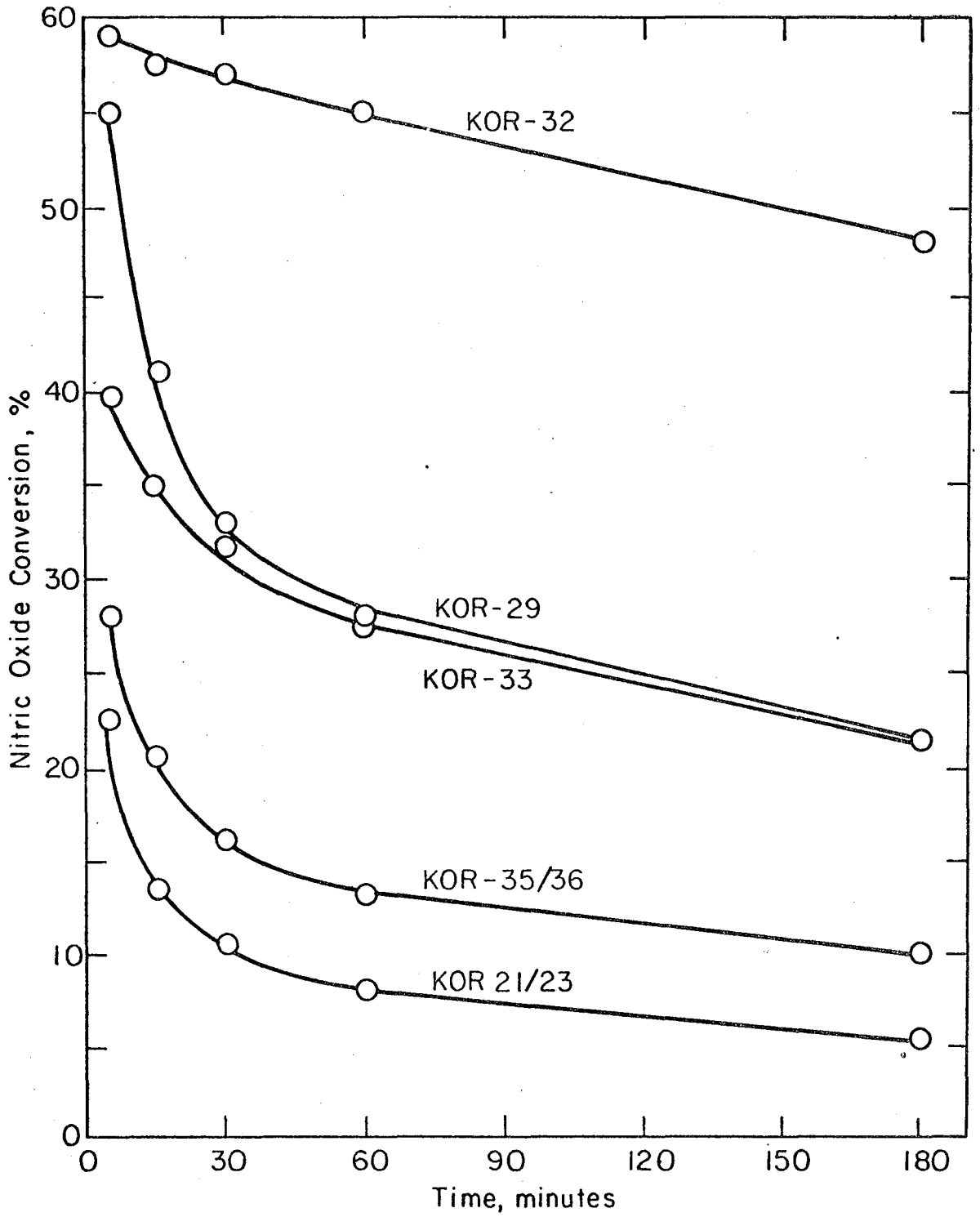
Fig. 14

XBL 785-5074

Table 4. Reactor Outlet Concentrations, Reducing Region

Run	C_{NO}, mole %				C_{CO}, mole %			
	t=5	t=15	t=30	t=60	t=5	t=15	t=30	t=60
KOR-21/23	3.88	4.40	4.63	4.81	8.69	9.16	9.34	9.49
KOR-29	2.00	2.69	3.06	3.52	4.26	4.87	5.14	5.44
KOR-32	0.73	0.78	0.82	0.89	2.18	2.40	2.46	2.54
KOR-33	1.06	1.18	1.27	1.40	4.00	4.19	4.29	4.40
KOR-35/36	2.82	3.30	3.53	3.75	7.28	7.67	7.86	8.00

level and the smallest percentage loss of activity. This run was made with the lowest concentrations of NO and CO, and a feed molar ratio of CO/NO close to 1:1. Holding the NO concentration approximately constant (at the level of KOR-32) and raising the CO concentration (KOR-33) resulted in a drop in initial activity and a faster rate of decay (compared to KOR-32). Increasing both NO and CO concentrations while keeping the feed stoichiometry close to 1:1 (KOR-29) resulted in high initial conversion, with an accompanying greater decay in activity (compared to KOR-33). Keeping the NO concentration at the level of KOR-29 and increasing the CO concentration (KOR-21/23, KOR-35/36) resulted in lower initial activity, with approximately the same percentage loss in activity (at 180 minutes).

From this limited data, two rough generalizations can be pointed out concerning the activity levels and the rate of deactivation. Runs made with the CO/NO ratio closest to 1:1 gave the highest initial conversion (KOR-29, KOR-32), while runs furthest from 1:1 having high CO concentrations exhibited the lowest initial activity (KOR-21/23). These trends indicate that the activity level exhibits an inverse dependence on the CO/NO ratio. Examination of the functional dependence of the reaction rate on NO and CO partial pressures (discussed in more detail below) confirms this observation. In addition, it appears that the rate of deactivation is soley linked to NO concentration. The run made at the lowest NO concentration (KOR-32) showed the smallest percentage loss in activity (or largest time constant), while the higher NO concentration runs (KOR-29, KOR-35/36, KOR-21/23) displayed the more rapid loss in activity (or smallest time constant). It is

interesting to note that runs KOR-29 and KOR-35/36, while having

approximately the same deactivation rate, had significantly different

CO partial pressures. This observation tends to confirm the lack

of dependence of the deactvation rate on CO concentration. In compar-

ing runs KOR-32 and KOR-33, one also notes that the made with the

higher NO concentration (KOR-33) has the higher deactivation rate.

The overall rate of reaction of nitric oxide (for times greater

than 60 minutes) was reasonably correlated with the simple rate exression:

$$R_{NO} = k \ P_{NO}/P_{CO}^2 \tag{8}$$

A plot of R_{NO} as a function of P_{NO}/P_{CO}^2 for t = 60 minutes is shown

in Figure 15. The slope of the best fitting straight line through

the origin, obtained by (least squares) linear regression, yielded

a value of $k = 1.22 \times 10^3$ micromoles-atm/sec/gm catalyst (or 5.63

molecules-atm/surface Pt/sec). The average deviation from the predicted

line was 17%. A similar analysis for t = 180 min gave a value of

k 76% of the value obtained at t = 60 min, with an average deviation

of 15%. The significant scatter of the data in Figure 15 most likely

reflects the influence of the deactivation process on the rate of

reaction, which of course is not accounted for in the simple rate

expression.

The NO and CO dependence in the rate expression above (Eq. 8)

can be derived by assuming that the rate of NO consumption is primarily

dependent on a rate limiting NO dissociation step. Such a process

is favored by calculations performed by Weinberg and Merrill (28)

Figure 15. Nitric oxide reaction rate as a function of P_{NO}/P_{CO}^2 for runs made under reducing conditions.

$$P_{NO}/P_{CO}^2, \text{ atm}^{-1}$$
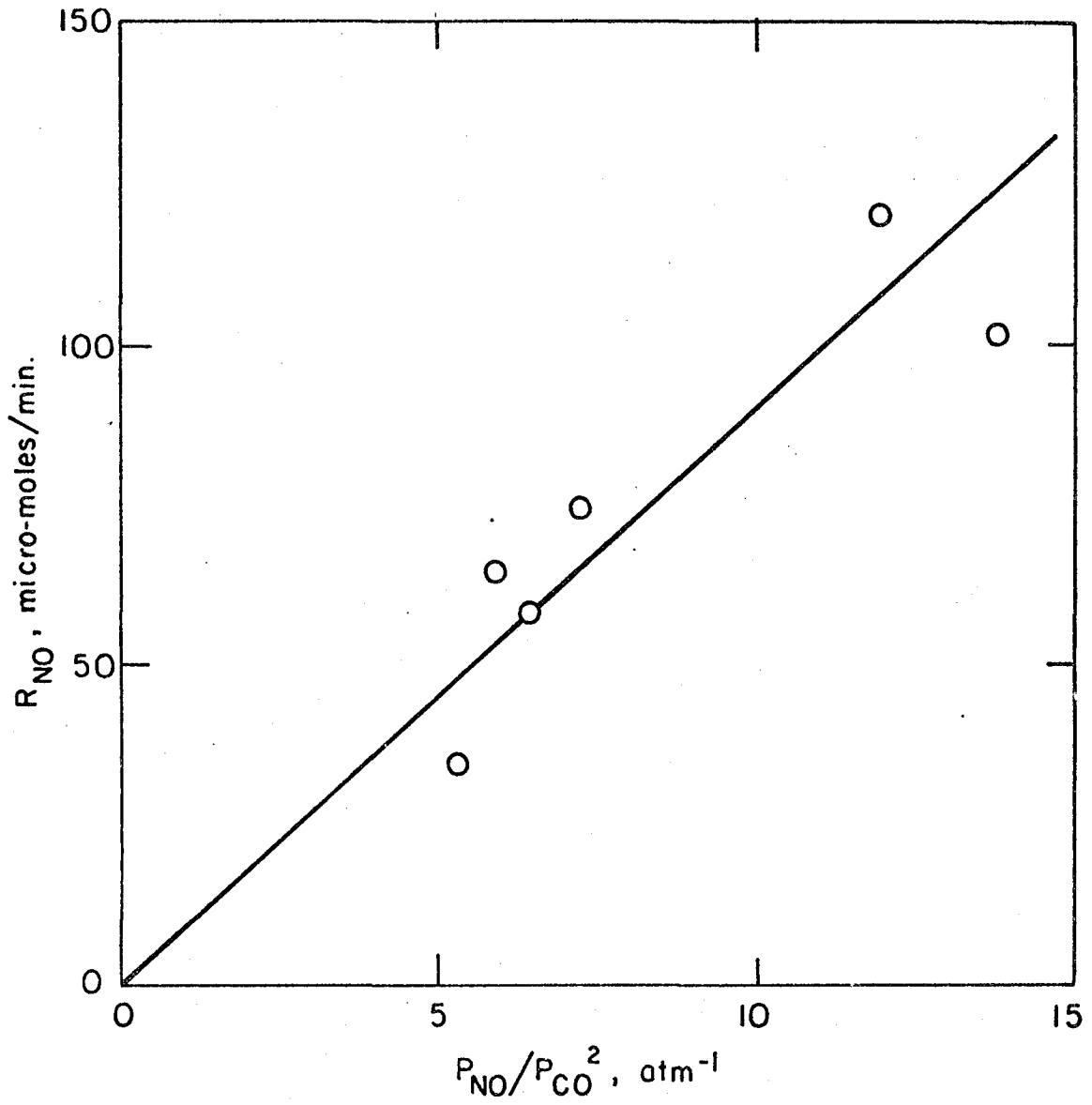
XBL 785-5071

Fig. 15

and studies done by Lambert and Comrie (3) and Cant et al (1). Rate limiting NO dissociation leads to a rate expression of the form:

$$R_{NO} = \frac{k' \, P_{NO}}{(1 + K_1 P_{NO} + K_2 P_{CO})^2} \qquad (9)$$

For the reducing conditions being considered, $K_2 P_{CO} \gg K_1 P_{NO}$ and $K_2 P_{CO} > 1$, since CO adsorbs more strongly than NO, and will cover a large percentage of the surface. This leads to:

$$R_{NO} = k' \, P_{NO} / (K_2 P_{CO})^2 \qquad (10)$$

which is indentical to Eq. 8 for $k = k'/K_2^2$. A more complete discussion of the molecular mechanism is presented in a later section dealing with selectivity.

The behavior of the stoichiometric ratio (R_s) in the reducing region is shown in Figure 16 for the runs KOR-21/23 and KOR-32. The data shown define the range of observed R_s values, with all other runs having values falling in the region between the two curves. R_s was found to be less than one in all cases, the lowest values corresponding to highly reducing conditions and low activity. Conditions leading to the highest conversion and smallest loss in activity (KOR-32) exhibited R_s values closest to one.

Excess carbon dioxide production is shown in Figure 17 for runs KOR-21/23, KOR-33, and KOR-32. Similar behavior was observed for the other runs as well. The rate of excess CO_2 production decreased rapidly from its initial value over the first 15 to 30 minutes, declining more slowly as time progressed. In some cases, the rate was observed to rise slightly between 50 to 180 minutes. The highest rates of excess

Figure 16.   Stoichiometric ratio as a function of time for

two runs made under reducing conditions. Curve

A: run KOR-32. Curve B: run KOR-21/23.
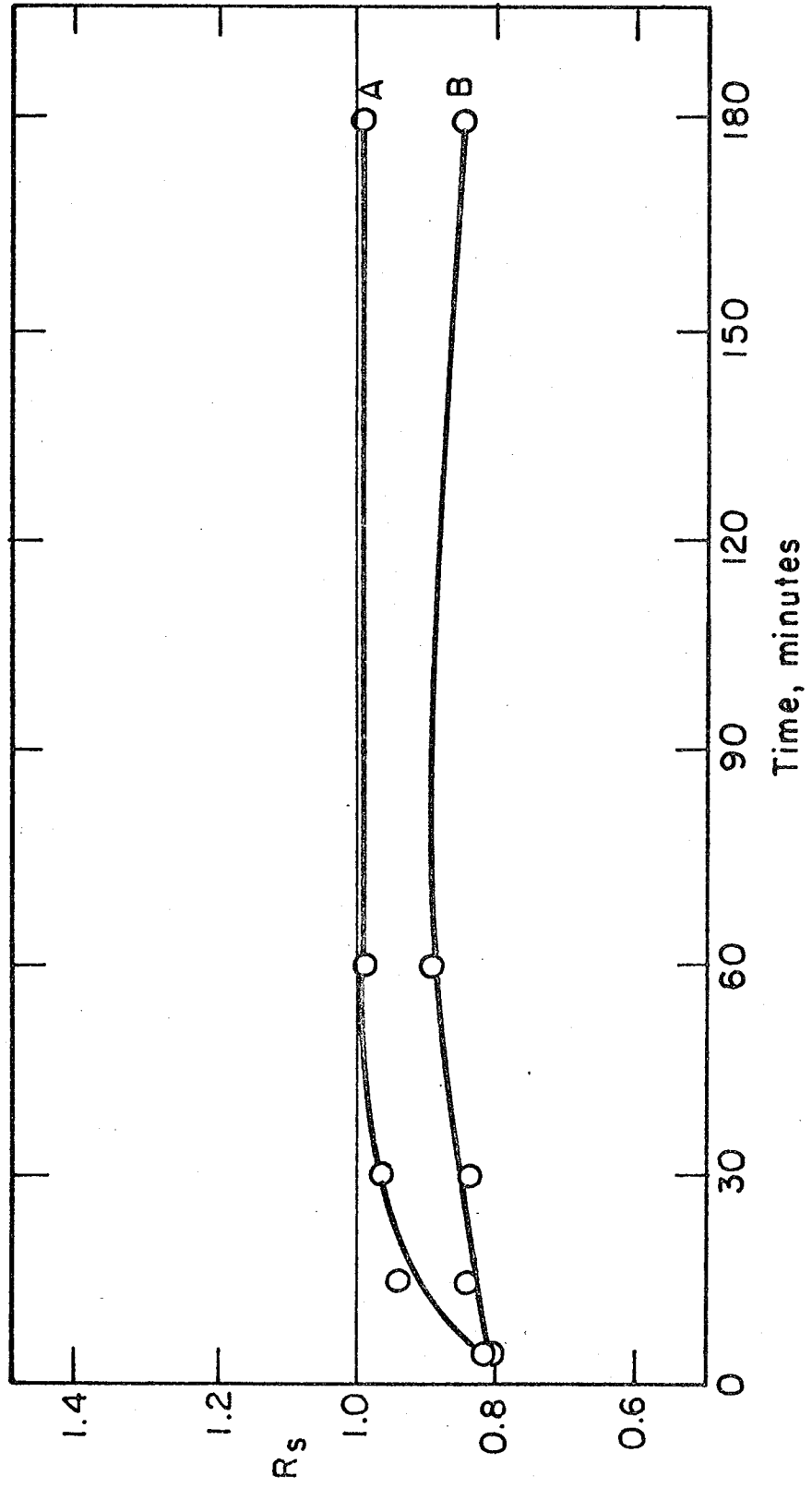
XBL 785-5079

Fig. 16

Figure 17.   Excess carbon dioxide production as a function

of time for three runs in the reducing region.

Curve A: run KOR-32. Curve B: run KOR-33. Curve

C: run KOR-21/23.
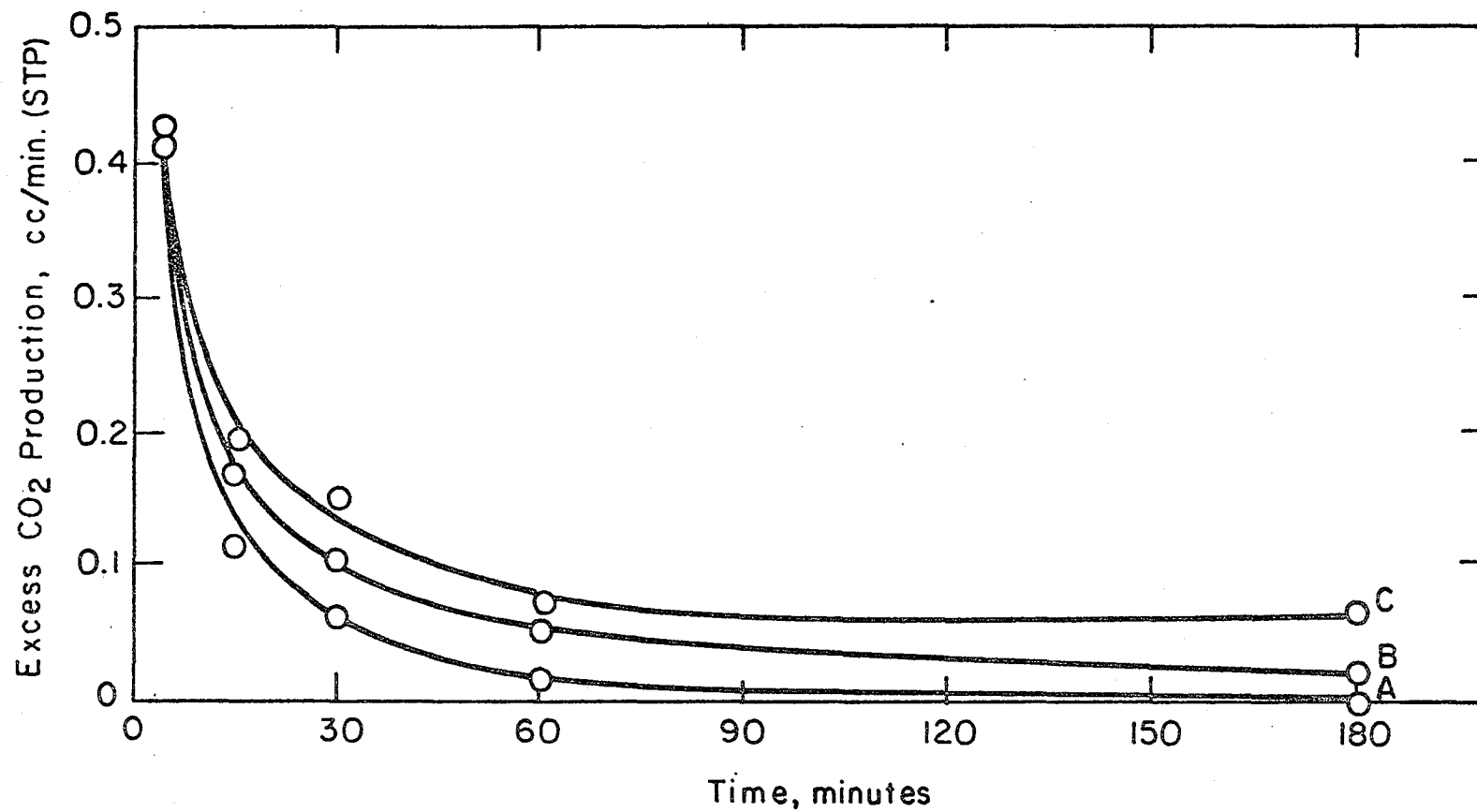
XBL 785-5103

Fig. 17

Table 5. Excess CO_2 Production

Run	Total excess CO_2 t=5 to 180 min	Equivalent monolayers of surface Pt
KOR-21/23	707 micromoles	2.7
KOR-29	248 micromoles	0.95
KOR-32	264 micromoles	1.0
KOR-33	497 micromoles	1.9
KOR-35/36	1280 micromoles	4.9

Calculations based on 260 micromoles total surface Pt

CO_2 production were found for runs made under highly reducing conditions. The lowest rates were observed for low concentration runs close to 1:1 stoichiometry, exhibiting high activity and the smallest rate of deactivation. These trends are also reflected in the total integrated excess CO_2 production figures given in Table 5. In all cases, the accumulated excess CO_2 was greater than or approximately equal to monolayer coverage.

Nitrous oxide selectivity as a function of time is shown in Figure 18 for three typical runs. The selectivity was found to be in the range of about 0.6 to 0.95, and was approximately constant during any single run, final values (at t = 180 min) being roughly 20% greater than initial values (at t = 0 min). A more complete discussion concerning trends and mechanism is presented below in section C.

2. Oxidizing Region

The kinetic behavior of the system for feed ratios of CO/NO less than one was distinctly different from that observed for reducing conditions. The conversion levels (based on CO) of all runs were very high, ranging from 95 to 100%. Since the gas feed system was operating near maximum capacity, conversion levels could not be reduced by increasing the feed rate of the reactants or the He diluent. The temperature was held at $300^{\circ}C$ in order to make comparisons between data taken in the oxidizing and reducing regions more valid.

R_s values were found to be slightly greater than one, and therefore no excess CO_2 was produced. Typical conversion and R_s data can be seen in Figures 19 and 20.

Figure 18.　Nitrous oxide selectivity as a function of time

for three runs made under reducing conditions.

Curve A:　run KOR-35/36.　Curve B:　run KOR-33.

Curve C:　run KOR-32.
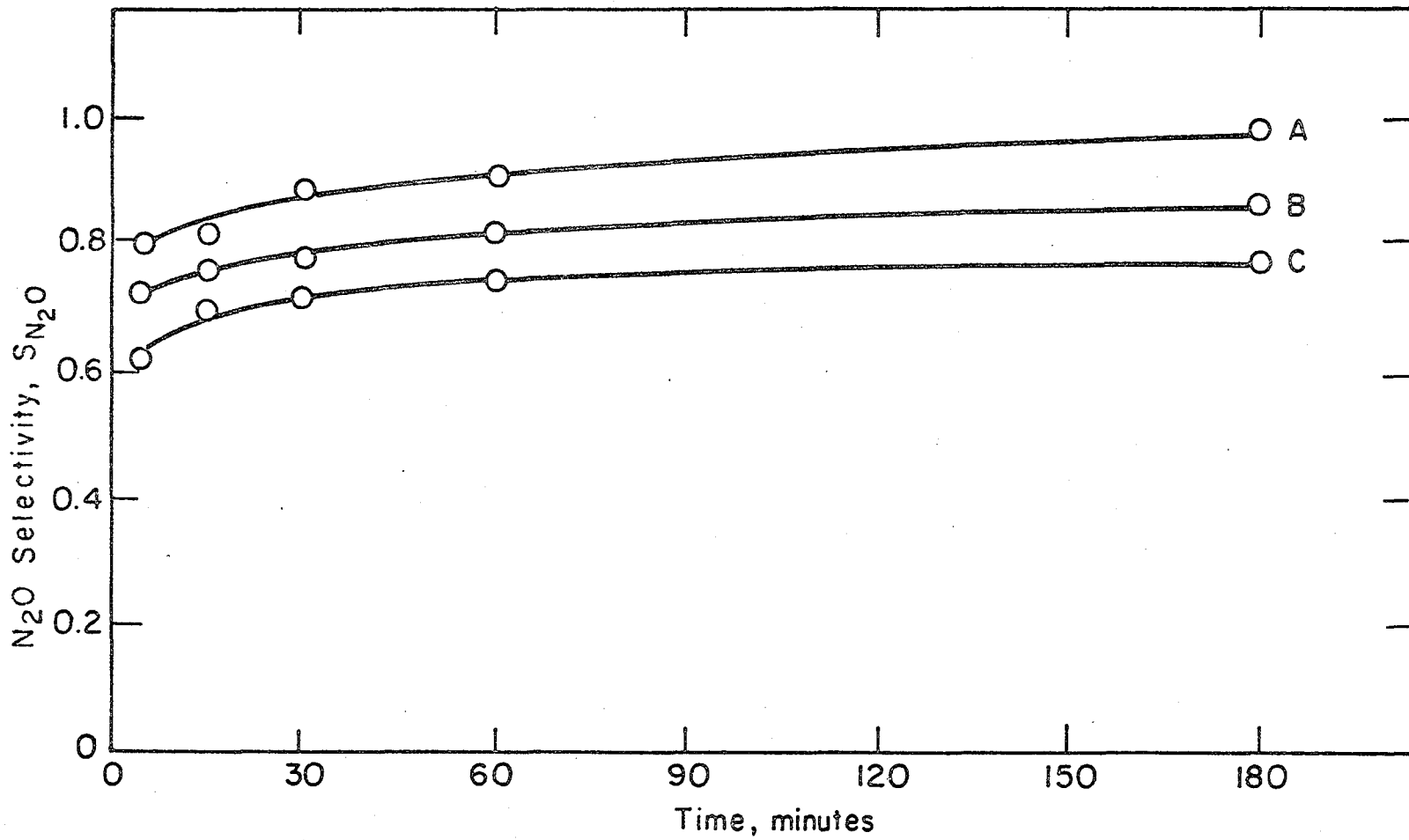
Fig. 18

XBL 785-5078

Figure 19.   Typical carbon monoxide conversion data as a function

of time for runs made in the oxidizing region.

Data from run KOR-28.

Fig. 19

XBL785-5077

Figure 20.   Typical stoichiometric ratio data as a function

of time for runs made in the oxidizing region.

Data from run KOR-28.
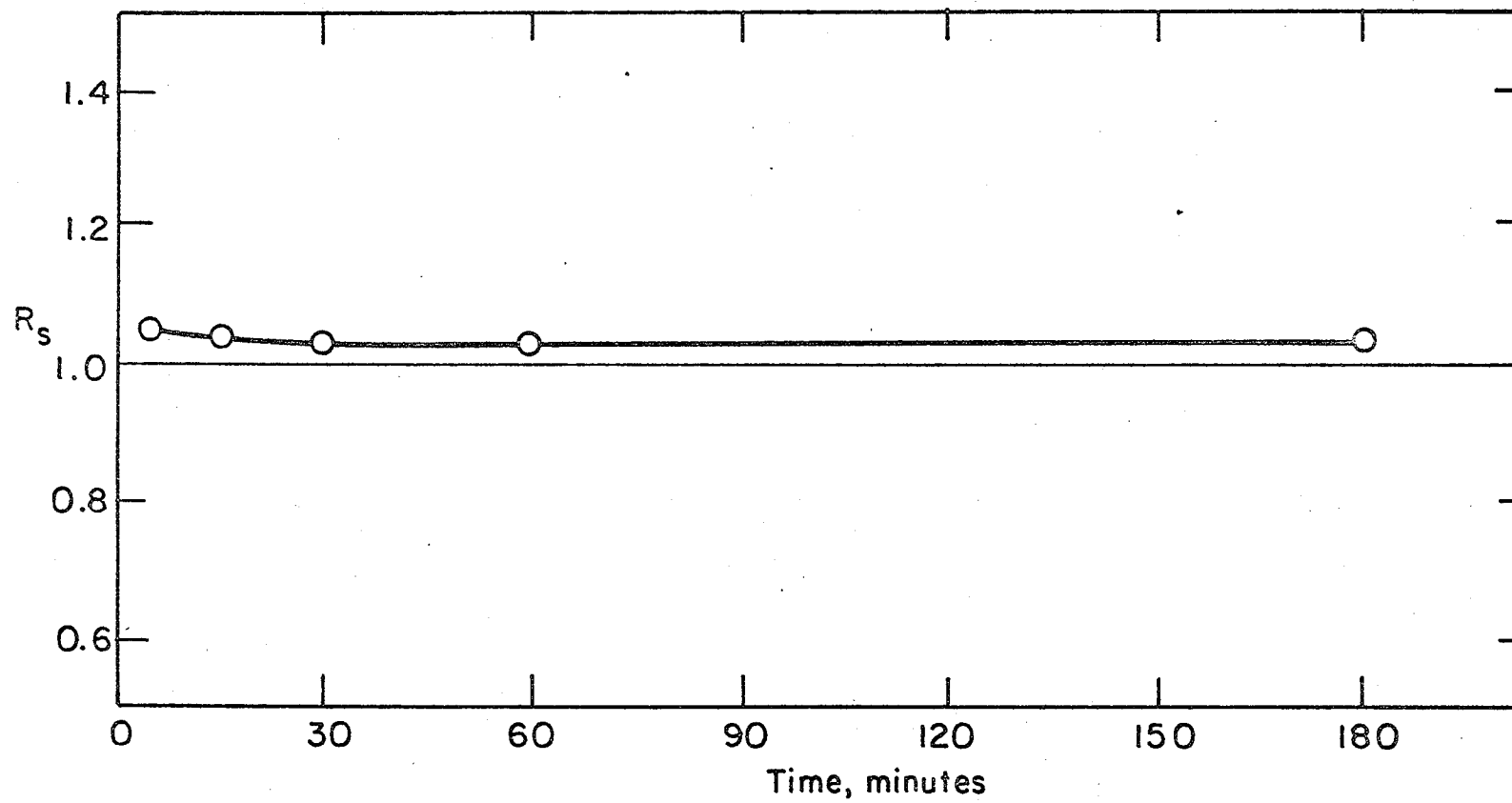
XBL 785-5076

Fig. 20

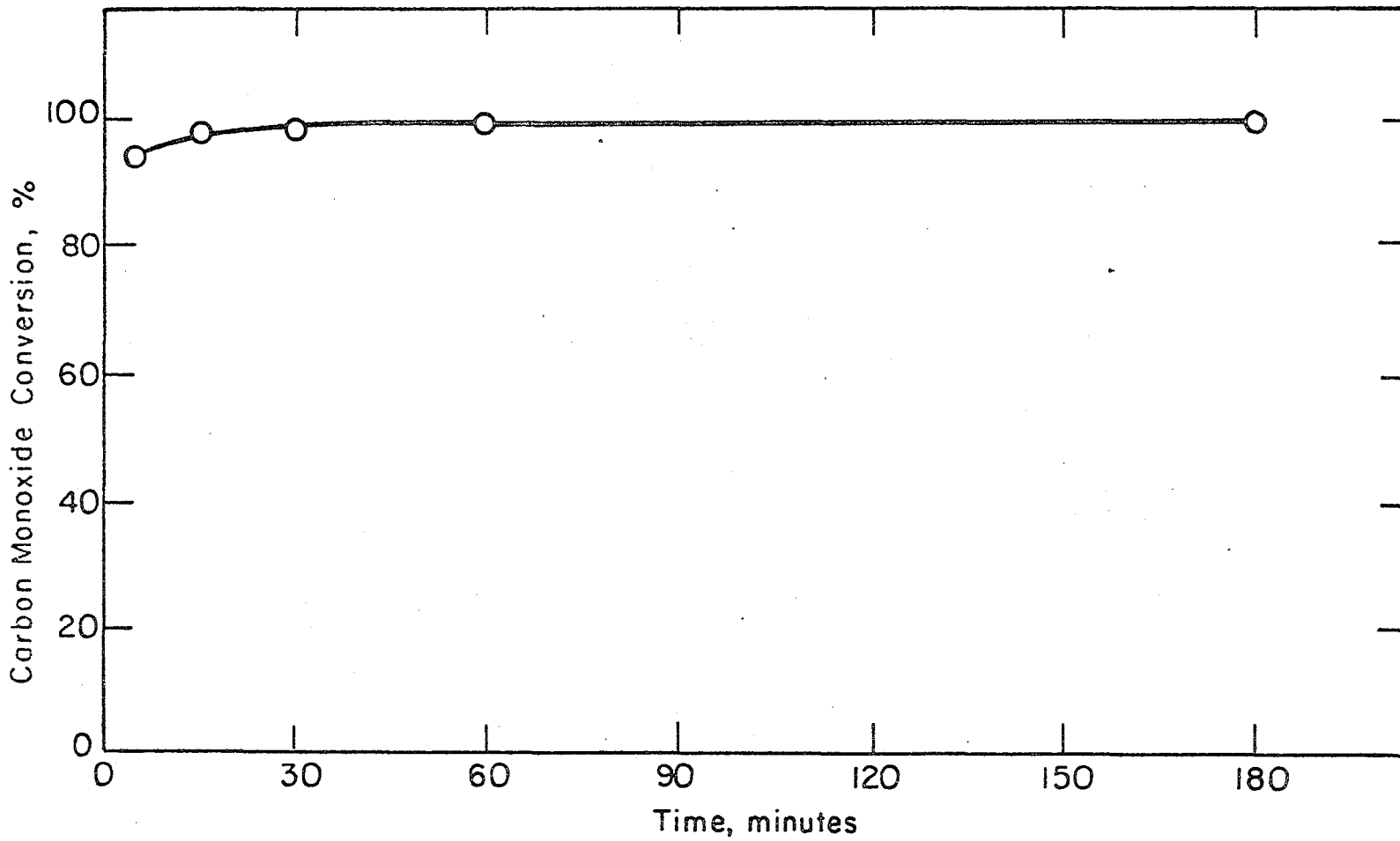Due to the high conversion levels, the very low CO concentrations in the reactor could not be accurately determined. Mass transfer limitations may not be negligable under these conditions, however claculations made using the criterion presented by Weisz and Prater (29), indicated that conversion levels greater than 95% could be attained without diffusional limitation. Thus, in order to detect the importance of mass transfer effects, a precision of at least 1% (or better) would be needed in measuring CO conversions. Experimental error associated with CO conversion measurements in this study limited precision to about 5%. As a result, the importance of mass transfer effects could not be determined within the limits of experimental error. No attempt was made to fit the data to an overall rate expression.

Nitrous oxide selectivity for four typical runs is shown in Figure 21. The range of values varied from approximately 0.0 to 0.5. The lowest N_2O selectivities were found for runs with molar feed ratios (CO/NO) close to 1:1 (KOR-31, KOR-26). It is worth moting, that for complete CO conversion at unity molar feed ratios, nitrogen is the only allowed product. This is a result of the stoichiometric relationships (Eq. 3 and 4) of NO and CO. Increasing the nitric oxide content of the feed (lowering the CO/NO ratio) resulted in an increase in N_2O formation, with the largest N_2O selectivity observed in run KOR-27. Due to the high CO conversions, increasing the NO/CO feed ratio resulted in a direct increase in the NO partial pressure in the reactor. The selectivity data is replotted in Figure 22 as a function of NO partial pressure in the reactor for the condition of very low accompanying

Figure 21.   Nitrous oxide selectivity as a function of time

for runs made under oxidizing conditions.   Curve A:

run KOR-27.   Curve B: run KOR-28.   Curve C: run

KOR-26.   Curve D: run KOR-31.
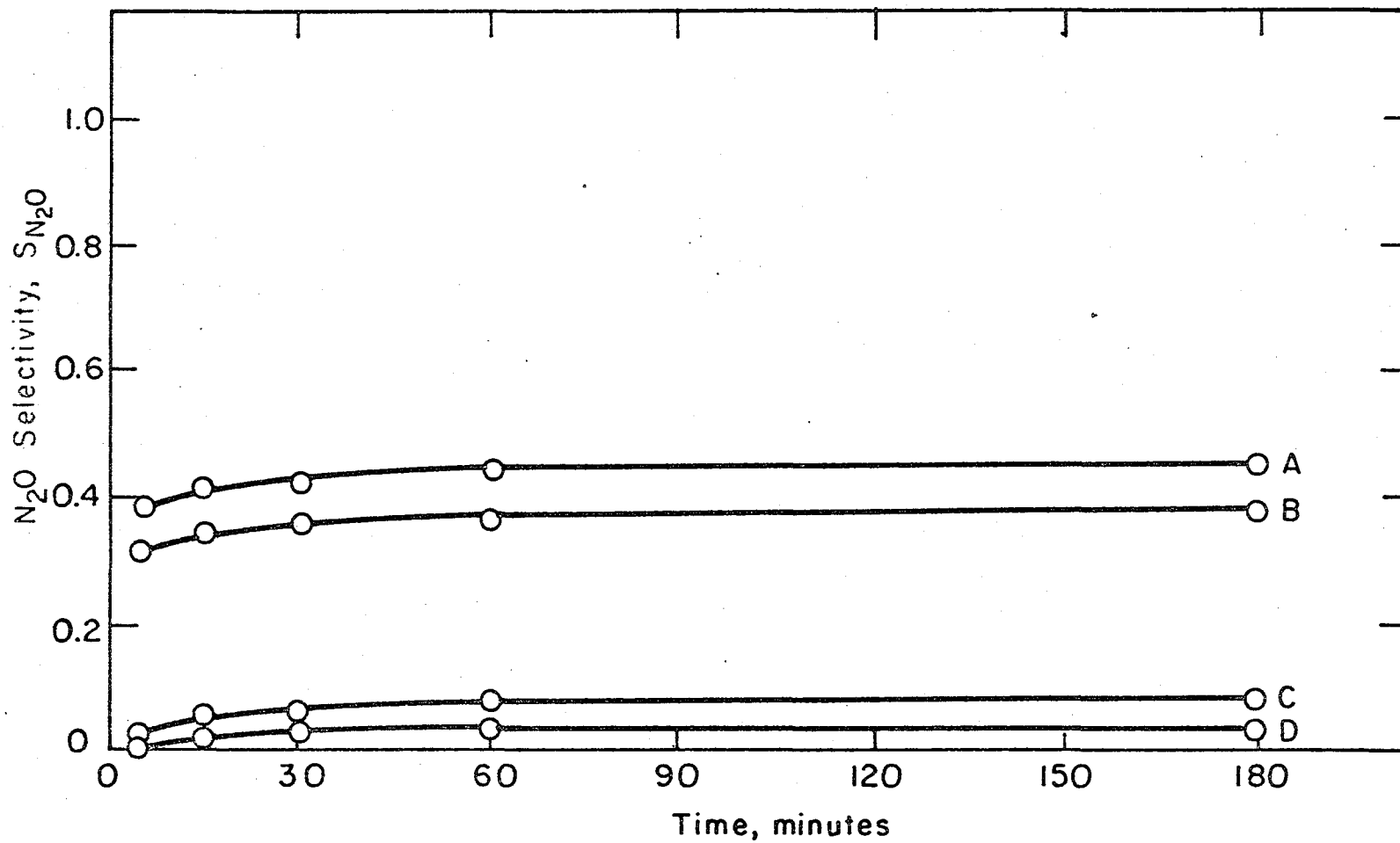
XBL 785-5075

Fig. 21

Figure 22.   Nitrous oxide selectivity as a function of nitric

oxide concentration for runs in the oxidizing region.
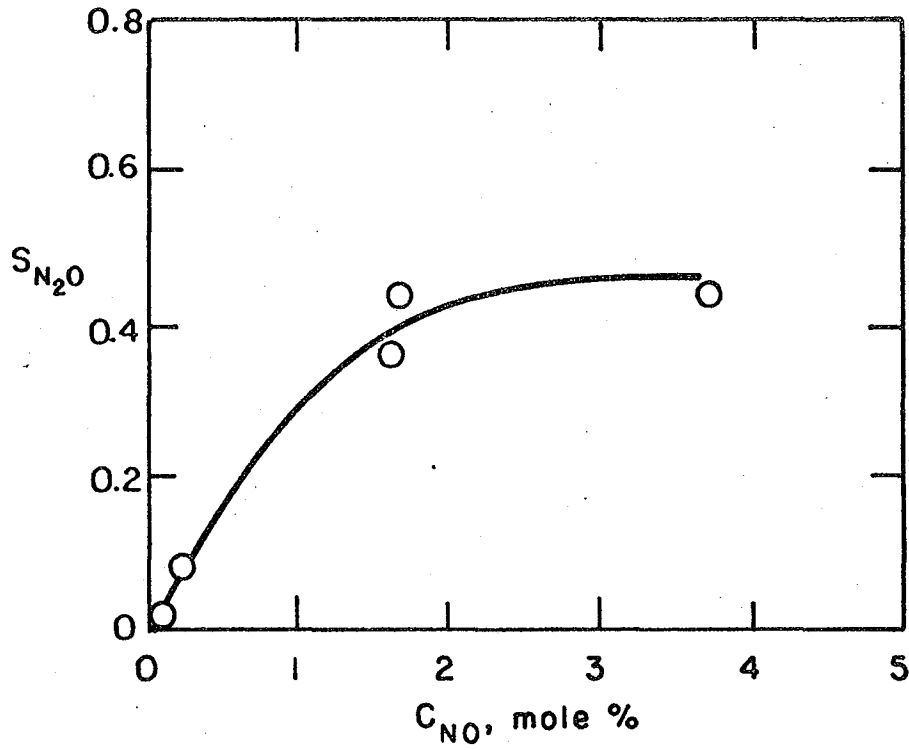
XBL785-5073

Fig. 22

CO partial pressures. Each point in this figure represents data from a single run.

C. Infrared Spectra

Typical infrared spectra taken under both oxidizing and reducing conditions are shown in Figure 23. The only observable peaks appeared in the region between 2500 and 2000 cm^{-1}. In most of the spectra, two major bands were observed; one at 2070 cm^{-1} and one at 2300 cm^{-1}. In addition, another band usually much smaller in magnitude, was observed at 2200 cm^{-1}. For the sake of the following discussion, the 2300 and 2200 cm^{-1} bands shall be assigned to an isocyanate and a cyanide species, respectively. Further discussion concerning the specific assignments of the 2300 and 2200 cm^{-1} bands is treated in section E. The band at 2070 cm^{-1} was identified as CO adsorbed on Pt (5).

The important features of the experimentally observed infrared spectra are summarized in the following discussion.

1. Reducing Region

Under reducing conditions the CO band (2070 cm^{-1}) absorbance varied within a range of about 0.3 to 0.4. A value of 0.4 represents saturation coverage of CO at 300°C, and is the value obtained by exposing the catalyst to a mixture of 10% CO in He. The lowest value (0.3) was reported for KOR-32. The absorbance trends can be clearly seen in Figure 24 where CO absorbance is plotted as a function of the CO concentration in the reactor. During any single run, the CO band intensity was not a function of time, and achieved its steady value immediately upon introduction of the reactants. In addition, no frequency shifts were observed for this band under any conditions.

Figure 23.   Typical infrared spectra. Curve a: He at 300°C.

Curve b: run made under oxidizing conditions (from

KOR-27).   Curve c: run made under reducing conditions

(from KOR-21). Spectra represented by curves b

and c taken approximately 30 min after start of

feed to reactor.
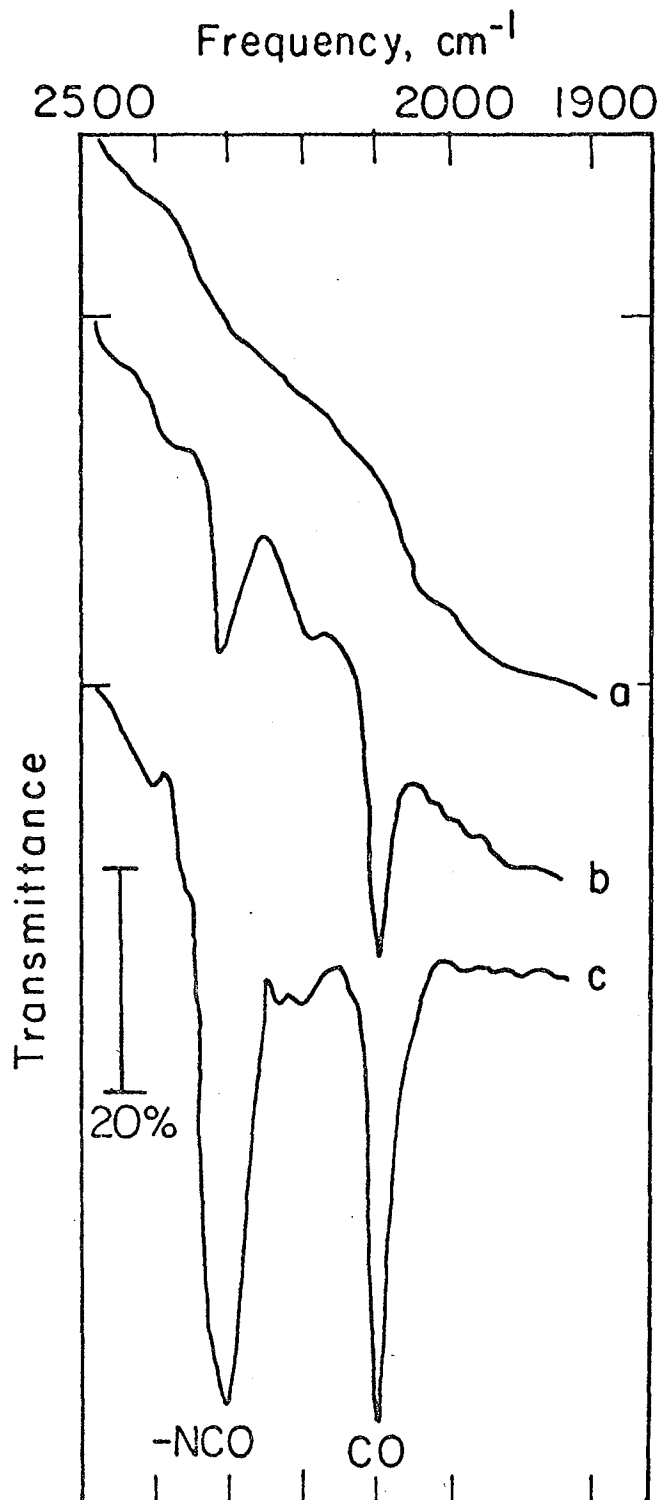
Fig. 23

Figure 24.   Carbon monoxide (2070 cm^{-1}) infrared band absorbance

as a function of carbon monoxide concentration

in the reactor for runs made in the reducing region.

IR absorbance was calculated from

$$\text{absorbance} = \log \frac{\text{baseline transmittance, \%}}{\text{peak transmittance, \%}}$$
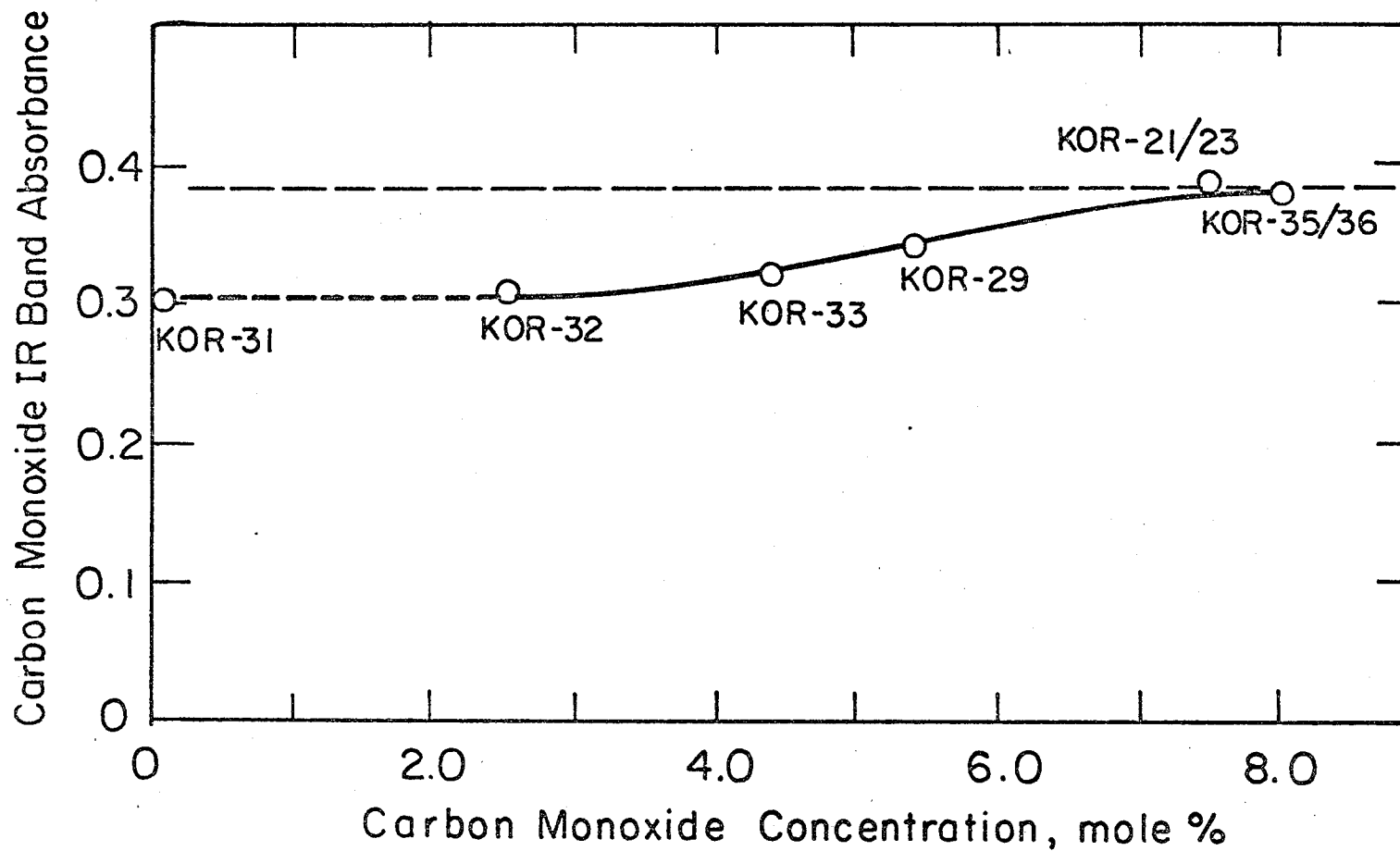
Fig. 24

XBL 786-5127

The formation and growth of the isocyanate (2300 cm^{-1}) and cyanide

(2200 cm^{-1}) bands were time dependent and very complex. On a fresh

catalyst disk, most of the isocyanate band growth took place during

the 30 to 60 minutes of exposure to the reactants, in a manner similar

to tht observed by Niiyama et al (16). Once formed, the isocyanate

band was very stable and could not be removed by prolonged periods

of heating in He at $300^{\circ}C$ or by the standard pretreatment process.

Because of this stability, repeated runs made under reducing conditions

induced additional band growth during each run, resulting in very

large accumulated bands (Figure 25). The growth of these very large

isocyanate bands did not affect the intensity of the CO band.

The isocyanate band exhibited some rather puzzling growth trends,

which were observed for most of the runs made in reducing atmospheres.

One of these trends was the growth of isocyanate band between successive

runs. This growth often amounted to a significant increase in band

size, and took place (very slowly) during tne 8 to 10 hr He purge

at $300^{\circ}C$ after the reactants were shut off, prior to the pretreatment

of the next run. Another puzzling but consistent trend was the apparent

temporary decrease in the isocyanate band intensity upon introduction

of the reactants. In one case (KOR-32, Figure 26) negative bands

were observed. Treatment of a large (absorbance=0.41) isocyanate

band (previously in He at $300^{\circ}C$ for 8 hrs) with a mixture of 10% CO

in He resulted in a 3% absorbance reduction after 15 minutes and an

8% reduction after 30 minutes. These changes were similar in magnitude

to isocyanate absorbance changes seen under reaction conditions.

Figure 25.   Infrared spectra for run KOR-22. Curve a: He
             purge following last step (H_2 reduction) of stand-
             ard pretreatment. Band at 2300 cm^{-1} results from
             accumulation of previous runs (KOR-20, 21). Curve
             b: 2 hrs after feed introduction, KOR-22.
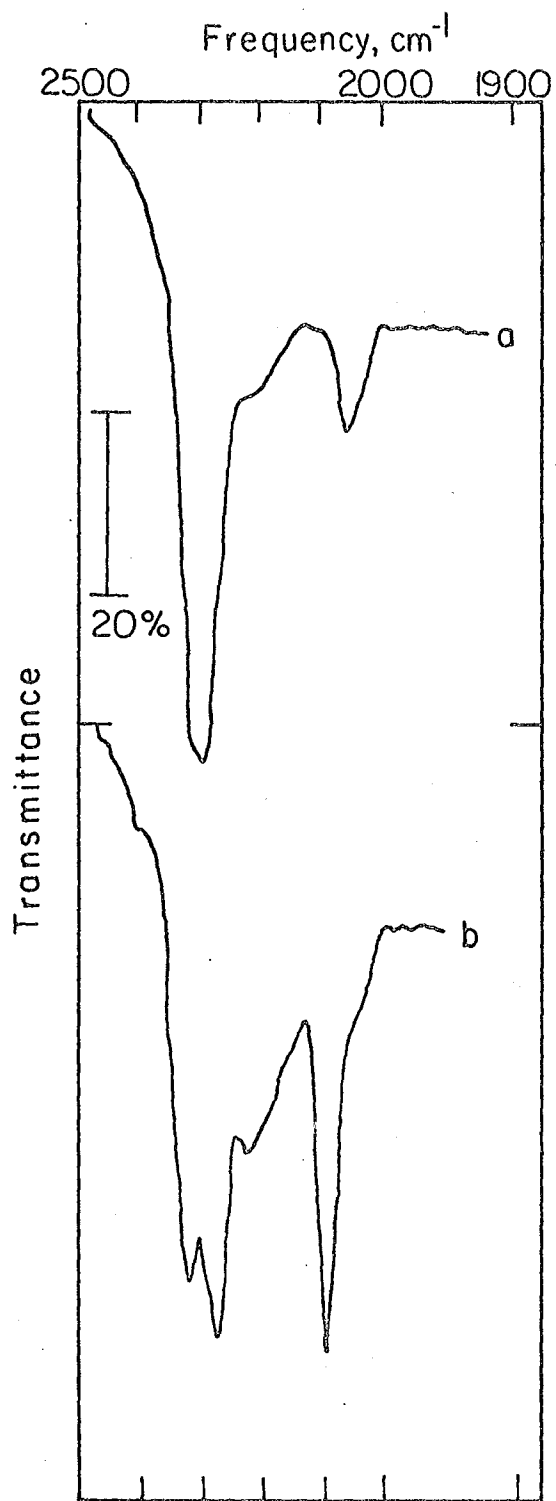
XBL 786-5123

Fig. 25

Figure 26.   Infrared spectra recorded during run KOR-32.   Curve a:

He purge prior to feed.   Curve b: 30 min after intro-

duction of feed.   Curve b':   45 min after introduction

of feed.   Curve c: 150 min after introduction of

feed.
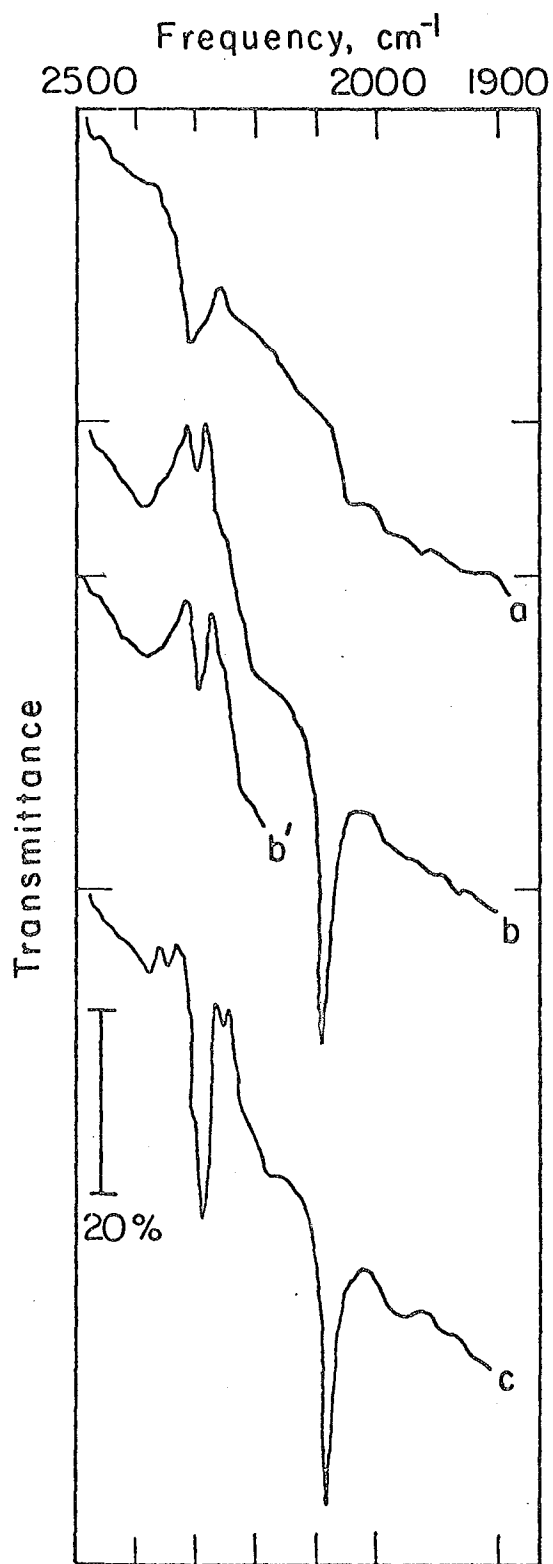
Fig. 26

XBL 786-5126

Treatment of the isocyanate band with NO mixtures resulted in no observable changes.

Interpretation of the isocyanate absorbance changes was complicated by the discovery that this species could be transferred to the reference IR disk. Evidence for this is clearly indicated in the form of negative bands near 2300 cm^{-1} (Figure 26). Solid confirmation for the presence of the isocyanate species on the reference disk was obtained by direct observation, by placing a reference disk (previously exposed to reactants under reducing conditions) in the sample IR beam, with an unused reference disk in the reference beam. This observation is important because it indicates that the isocyanate species is not only capable of bonding to the silica support, but it is also capable of transferring itself through the gas phase to the reference disk and perhaps the reactor walls. As a result, caution must be exercised in interpreting isocyanate band absorbance changes, since the recorded spectra is indicative only of the difference in the amount of this species between the two disks.

The isocyanate band was easily removed by exposure to water vapor (~20% relative humidity) at 25°C. This process is illustrated in Figure 27. It is interesting to note that some cyanide (2200 cm^{-1}) band growth accompanies the removal of the isocyanate band. This indicates that the cyanide species may be a by-product of the isocyanate hydrolysis. In addition, the isocyanate species on the reference disk appears to be more resistant to removal by water at room temperature than the isocyanate species on the catalyst disk. This is evident by the negative band at 2300 cm^{-1} in curve d, Figure 27. Complete

Figure 27.　　Removal of the isocyanate (2300 cm^{-1}) band with

H_2O. Curve a: band prior to treatment. Curve

b: 30 min after introduction of approximately 5

torr H_2O in He (1 atm total pressure, $25^{\circ}C$). Curve

c: 1 hr after introduction of H_2O/He mixture.

Curve d: 4 hrs after introduction of H_2O/He mixture.

Curve e: after heating in He at $300^{\circ}C$ for 2 hrs.

that this approach would lead to a more complete understanding of the system behavior than regression to a power law type expression.

The mechanism utilized in the selectivity analysis is illustrated in Figure 28. These reactions were chosen as those "most likely to proceed", and were based on results published in recent literature and experimental trends observed in this study. Many of the arguments supporting the mechanism have been presented by Ludvik (9) and shall not be discussed in detail here.

For simplicity, the deactivation process was not considered in the selectivity analysis, and therefore is not included in the mechanism. Since the selectivity does not change to a large extent during deactivation (see Figure 18), the omission of the deactivation mechanism is justified, considering the scope of the selectivity analysis.

Step (1) in Figure 28 describes the strong molecular chemisorption of carbon monoxide. This process is well known and direct evidence is reported in this study in the form of an intense infrared band at 2070 cm^{-1}.

Figure 28.   Reaction mechanism used in the analysis of nitrous oxide

selectivity data.

Reaction Mechanism:

(1) $CO_{(g)} + s \xrightleftharpoons{K_1} CO_{(a)}$

(2) $NO_{(g)} + s \xrightleftharpoons{K_2} NO_{(a)}$

(3) $NO_{(a)} + s \xrightarrow{k_3} N_{(a)} + O_{(a)}$

(4) $2N_{(a)} \xrightarrow{k_4} N_{2(g)} + 2s$

(5a) $N_{(a)} + NO_{(g)} \xrightarrow{k_{5a}} N_2O_{(g)} + s$

(5b) $N_{(a)} + NO_{(a)} \xrightarrow{k_{5b}} N_2O_{(g)} + 2s$

(6) $CO_{(g)} + O_{(a)} \xrightarrow{k_6} CO_{2(g)} + s$
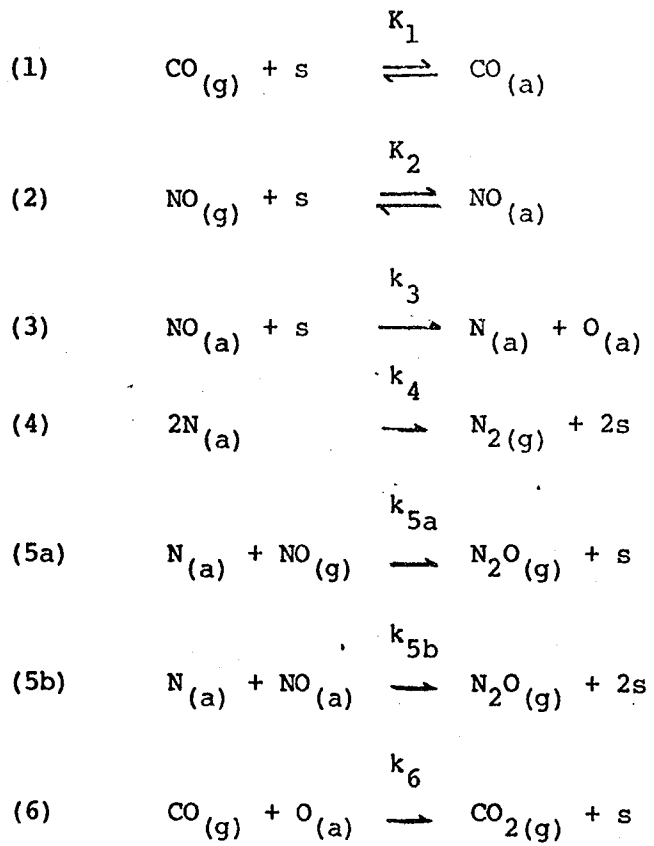
Fig. 28

Step (2) represents the molecular chemisorption of nitric oxide. Evidence in support of adsorbed NO molecules on Pt has been reported in thermal desorption studies performed by Lambert and Comrie (3) and others (6, 7, 8).

The dissociation of adsorbed NO molecules into adsorbed nitrogen and oxygen atoms is represehted in step (3). Experimental evidence for this process has been reported in work done by Lambert and Comrie (3), Pirug and Bonzel (6, 7), and Solymosi et al (8). The dissociation of adsorbed NO has also been suggested in a kinetic analysis reported by Cant et al (1). Calculations performed by Weinberg and Merrill (28) indicate that this process has an estimated activation energy between zero and 11.3 kcal/mole, however this is somewhat lower than the experimentally measured value of 28 kcal/mole reported by Pirug and Bonzel (8).

The route to N_2 production is accounted for by step (4), which represents the recombination of adsorbed nitrogen atoms. Experimental evidence for this reaction process has been presented in studies done by Wilf and Dawson (30) and Schawaha and Bechtold (31), as well as the previously mentioned studies (6, 7, 3). The production of N_2 via gas phase N_2O:

$$s + N_2O_{(g)} \rightarrow O_{(a)} + N_{2(g)} \qquad (11)$$
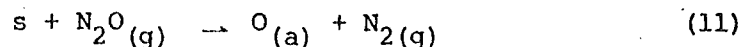
was not included in this mechanism since it is not considered the primary route to nitrogen. This reaction path does not permit S_{N_2O} values close to zero (or very low P_{N_2O}) since the rate of N_2 production must

be proportional to P_{N_2O}, and therefore is not in agreement with experimental results obtained in this study ($S_{N_2O} \sim 0$ for $P_{NO} > P_{CO}$, $P_{NO}/P_{CO} \simeq 1$).

Steps (5a) and (5b) represent two possible paths to nitrous oxide production. Step (5) is the Eley-Rideal process in which an adsorbed nitrogen atom reacts with a gas phase NO molecule. This reaction path is favored by BEBO calculations performed by Weinberg and Merrill (28), and is estimated to have an activation energy of approximately 20 kcal/mole. Step (5b) represents the Langmuir-Hinshelwood process in which adsorbed NO reacts with adsorbed nitrogen atoms to produce N_2O. This process is favored by Cant et al (1). Both steps (5a) and (5b) were considered in the selectivity analysis presented below.

The final step (6) represents the process by which adsorbed oxygen is removed from the surface. This process is estimated to have an activation energy very close to zero (32). The reaction:

$$O_{(a)} + CO_{(a)} \rightarrow CO_{2(g)} + 2s \tag{12}$$
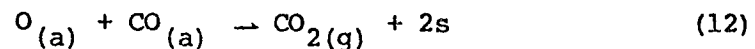
was not considered due to its high activation energy of 27 kcal/mole (32). Preferential reduction via an Eley-Rideal process is also consistent with experimental results reported by Bonzel and Ku (33).

1. Reducing Region

Utilizing the proposed reaction mechanism along with some simplifying assumptions, expressions for R_{N_2}/R_{N_2O} were obtained for both the Eley-Rideal and Langmuir-Hinshelwood N_2O production steps. These are shown in final form in Table 6. The primary assumption made in deriving the expressions was that nitric oxide dissociation was rate limiting. Experimental support for this assumption has been presented

previously (section B-1), where the overall rate was correlated assuming NO dissociation. Reactions (4), (5), and (6) in Figure 28 were assumed irreversible and fast compared to reaction (3). Reactions (1) and (2) were assumed to be at equilibrium; i.e., the surface concentrations (θ_{NO} and θ_{CO}) were set equal to the product of θ_v times the gas phase partial pressure multiplied by an equilibrium constant. In addition, it was assumed that under reducing conditions, CO surface coverage will be larger than any other species, reducing the site balance to:

$$1 \simeq \theta_v + \theta_{CO} \qquad (13)$$

where θ_v and θ_{CO} are fractional coverages of vacant sites and CO covered sites, respectively. The complete derivation of the expressions for R_{N_2}/R_{N_2O} is given in Appendix 2.

Using equation (1), the ratio R_{N_2}/R_{N_2O} can be related to S_{N_2O}. Algebraic rearrangement yields the expressions (presented in Table 6) which can be plotted to test the fit of the data to each particular mechanism. For the Eley-Rideal nitrous oxide production step, a plot of

$$\left\{ P_{NO} \left[(2/S_{N_2O} - 1)^2 - 1 \right] \right\}^{-1/2} \qquad (14)$$

versus P_{CO} should yield a straight line. For the Langmuir-Hinshelwood mechanism, a plot of $(2/S_{N_2O} - 1)^2$ versus $1/P_{NO}$ should result in a straight line which passes through the origin.

TABLE 6

Reducing Region, P_{CO} P_{NO}

Assumed (3) NO dissociation rate limiting

Eley-Rideal N_2O production step:

$$R_{N_2}/R_{N_2O} = \frac{1}{2}\left[\left(1 + \frac{4k_4 k_3 K_2}{k_5^2 (1 + K_1 P_{CO})^2 P_{NO}}\right)^{\frac{1}{2}} - 1\right]$$

$$\left(\frac{1}{P_{NO}\left[(2/S_{N_2O} - 1)^2 - 1\right]}\right)^{\frac{1}{2}} = \frac{k_5}{4k_4 k_3 K_2}(1 + K_1 P_{CO})$$

Langmuir-Hinshelwood N_2O production step:

$$R_{N_2}/R_{N_2O} = \frac{1}{2}\left[\left(1 + \frac{4k_4 k_3}{k_5^2 K_2 P_{NO}}\right)^{\frac{1}{2}} - 1\right]$$

$$(2/S_{N_2O} - 1)^2 - 1 = \frac{4 k_4 k_3}{k_5^2 K_2}(1/P_{NO})$$

In Figure 29 the data is plotted utilizing the expression obtained

for the Langmuir-Hinshelwood mechanism. An attempt to plot the data

in accordance with the Eley-Rideal mechanism resulted in an excessive

amount of scatter and no apparent correlation.

As can be seen in Figure 29, the data fit is reasonably good

(except for a single point) over the range of values studied. These

results tend to confirm the dominance of the Langmuir-Hinshelwood

mechanism for nitrous oxide production and are in agreement with those

of Cant et al (1). It is worth noting, however, that BEBO estimations

of activation energies (28) combined with absolute rate theory would

have favored an Eley-Rideal process for N_2O formation.

The scatter introduced by the one point (KOR-29) illustrates

the difficulty in obtaining reproducible results for runs made (under

reducing conditions) at different times with different pre-run histories.

The data closest to the line in Figure 29 were taken from runs KOR-

32 to KOR-38, all of which were made in a continuous sequence (without

an intervening oxidation run). Run KOR-29 was preceded by three runs

made under oxidizing conditions. In addition, the value of S_{N_2O} was

found to be significantly lower for a fresh catalyst, compared to

that for an aged catalyst tested under the same conditions. The causes

of these effects are not known, and consequently caution must be exer-

cised in interpreting the results presented.

2. Oxidizing Region

In the oxidizing region, the rate limiting step was assumed to

be (6) in Figure 28, due to the high conversions and very low CO partial

pressures. The infrared CO bands indicated that, even under highly

Figure 29.   Test of selectivity data for runs made under reducing

conditions.   Langmuir-Hinshelwood mechanism.

Reducing Region, $P_{CO} > P_{NO}$

S_{N_2O} at $t = 60$ min.

Langmuir-Hinshelwood
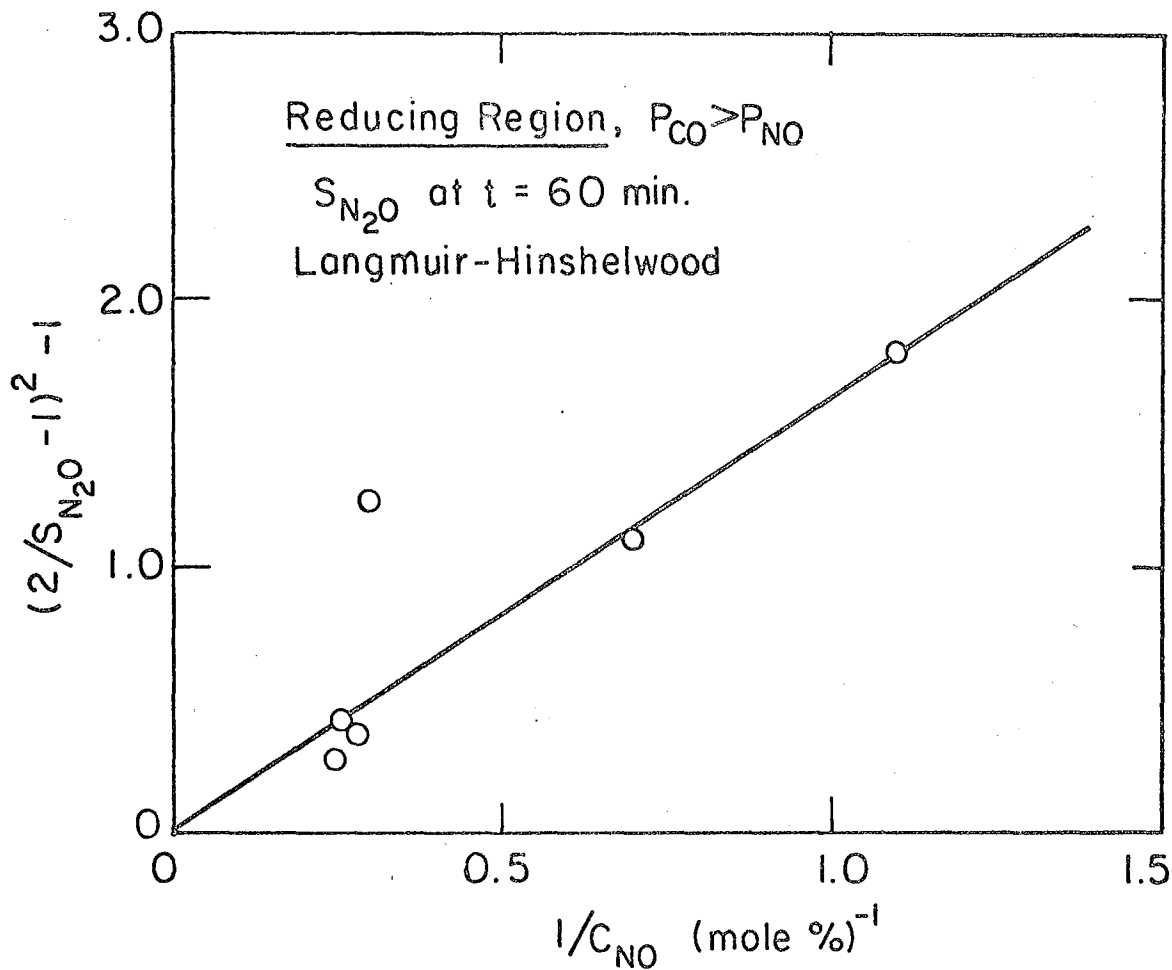
XBL 786-5120

Fig. 29

TABLE 7

Oxidizing Region, P_{CO} P_{NO}

Assumed (6) CO oxidation rate limiting

Eley-Rideal N_2O production step:

$$R_{N_2}/R_{N_2O} = \tfrac{1}{2}\left[\left(1 + \frac{4k_4k_6\ P_{CO}}{k_5^2\ P_{NO}^2}\right)^{\tfrac{1}{2}} - 1\right]$$

$$(2/S_{N_2O} - 1)^2 - 1 = \frac{4k_4k_6\ P_{CO}}{k_5^2\ P_{NO}^2} \doteq \frac{4k_4\ F_{CO}^o}{k_5^2\ P_{NO}^2}$$

Langmuir-Hinshelwood N_2O production step:

$$R_{N_2}/R_{N_2O} = \tfrac{1}{2}\left[\left(1 + \frac{k_4\ k_3}{k_5^2\ K_2\ P_{NO}}\right)^{\tfrac{1}{2}} - 1\right]$$

$$(2/S_{N_2O} - 1)^2 - 1 = \frac{4\ k_4\ k_3}{k_5^2\ K_2}\ (1/P_{NO})$$

oxidizing conditions, the surface was still covered with roughly 50 to 75% of the CO equilibrium coverage. As a result, the CO coverage was considered approximately constant, and the site balance was made over the remaining sites. This is equivalent to assuming that 1/2 to 3/4 of the surface, being covered with CO, is inactive toward the NO reduction reactions. Mathematically similar results would have been obtained for constant θ_{CO} (between 0.5 and 0.75) with the site balance made over the entire surface.

Two mechanisms for N_2O formation were considered, as was done in the reducing region. The results are summarized in Table 7 and derived in Appendix 3. The expression for R_{N_2}/R_{N_2O} for the Langmuir-Hinshelwood mechanism was obtained without additional assumptions. The Eley-Rideal mechanism, however, required additional simplifying assumptions. For this mechanism the site balance was reduced to:

$$1 \simeq \theta_O + \theta_V \qquad (15)$$

where θ_O and θ_V are fractional coverages of adsorbed oxygen atoms and vacant sites, respectively. Under highly oxidizing conditions, for small P_{CO} and large P_{NO}, θ_O was assumed to be the dominant surface species. In this case θ_V will be small compared to 1, and θ_O will be on the order of 1. The rate of CO reaction can be simplified to:

$$R_{CO} = k_6 \, _O P_{CO} \simeq k_6 P_{CO} \qquad \text{for } \theta_O \simeq 1 \qquad (16)$$

In a CFSTR at 100% CO conversion,

$$F_{CO}^{O} = R_{CO} \qquad (17)$$

where F_{CO}^{O} is the input molar feed rate of CO. This allows the

replacement of the group $k_6 P_{CO}$ by F_{CO}^{O} (combining (16) and (17)

above) in the expression for $R_{N_2}/R_{N_2}O$ in Table 7, since under highly

oxidizing conditions P_{CO} is not known accurately.

Algebraic rearrangement of the expressions obtained for the ratio

R_{N_2}/R_{N_2O} yield equations which can be plotted to test the data. The

quantity $(2/S_{N_2O} - 1)^2 - 1$ is plotted versus $1/P_{NO}$ in Figure 30 and

versus F_{CO}^{O}/P_{NO}^2 in Figure 31, corresponding to the Langmuir-Hinshelwood

and Eley-Rideal mechanisms, respectively. The large range of numerical

values required use of a log-log scale. As can be seen in Figures

30 and 31, neither mechanism results in a correlation of the data

along a straight line. In particular, at low P_{NO} the experimental

values of the quantity plotted on the ordinate are larger than antici-

pated by the model. Failure of the model in this regime may be associated

with a breakdown in the assumption that CO oxidation represents the

rate limiting step, since as P_{NO} declines it eventually becomes comparable

in magnitude with P_{CO}. When this becomes true, it is likely that

the kinetics will undergo a transition to the rate limited NO dissociation

process. It should be noted further that at low P_{NO} the measurements

of S_{N_2O} become inaccurate due to the very low rates of N_2O formation

that must be measured. In conclusion, then, since neither model appears

Figure 30.   Test of selectivity data for runs made under oxidizing

conditions.   Langmuir-Hinshelwood mechanism.
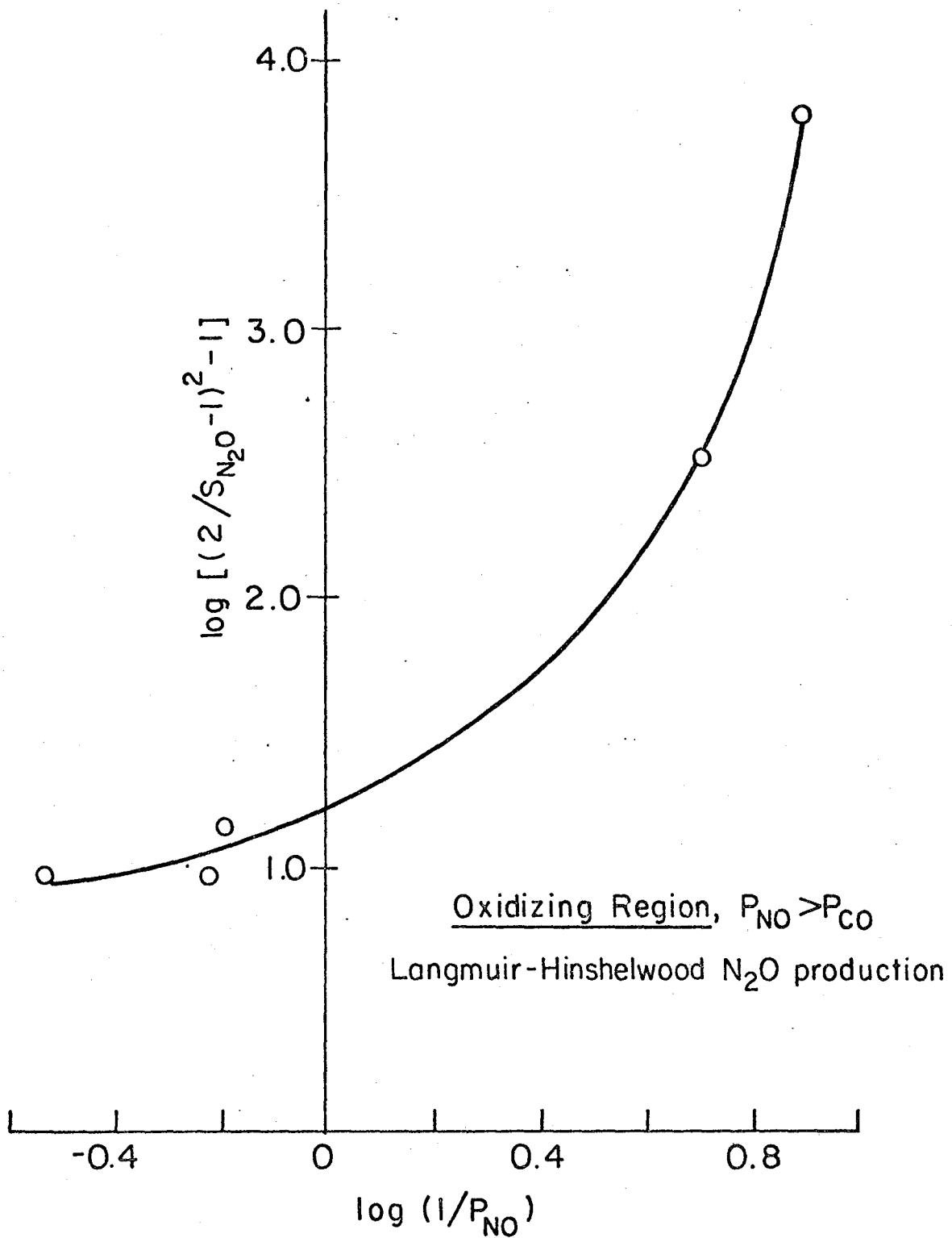
Fig. 30

XBL786-5121

Figure 31.   Test of selectivity data for runs made under oxidi-

zing conditions.   Eley-Rideal mechanisms.

Oxidizing Region, $P_{NO} > P_{CO}$

Eley-Rideal N_2O production

Y-axis: $\log \left[\left(2/S_{N_2O} - 1 \right)^2 - 1 \right]$

X-axis: $\log \left(F^{\circ}_{CO} / P^2_{NO} \right)$
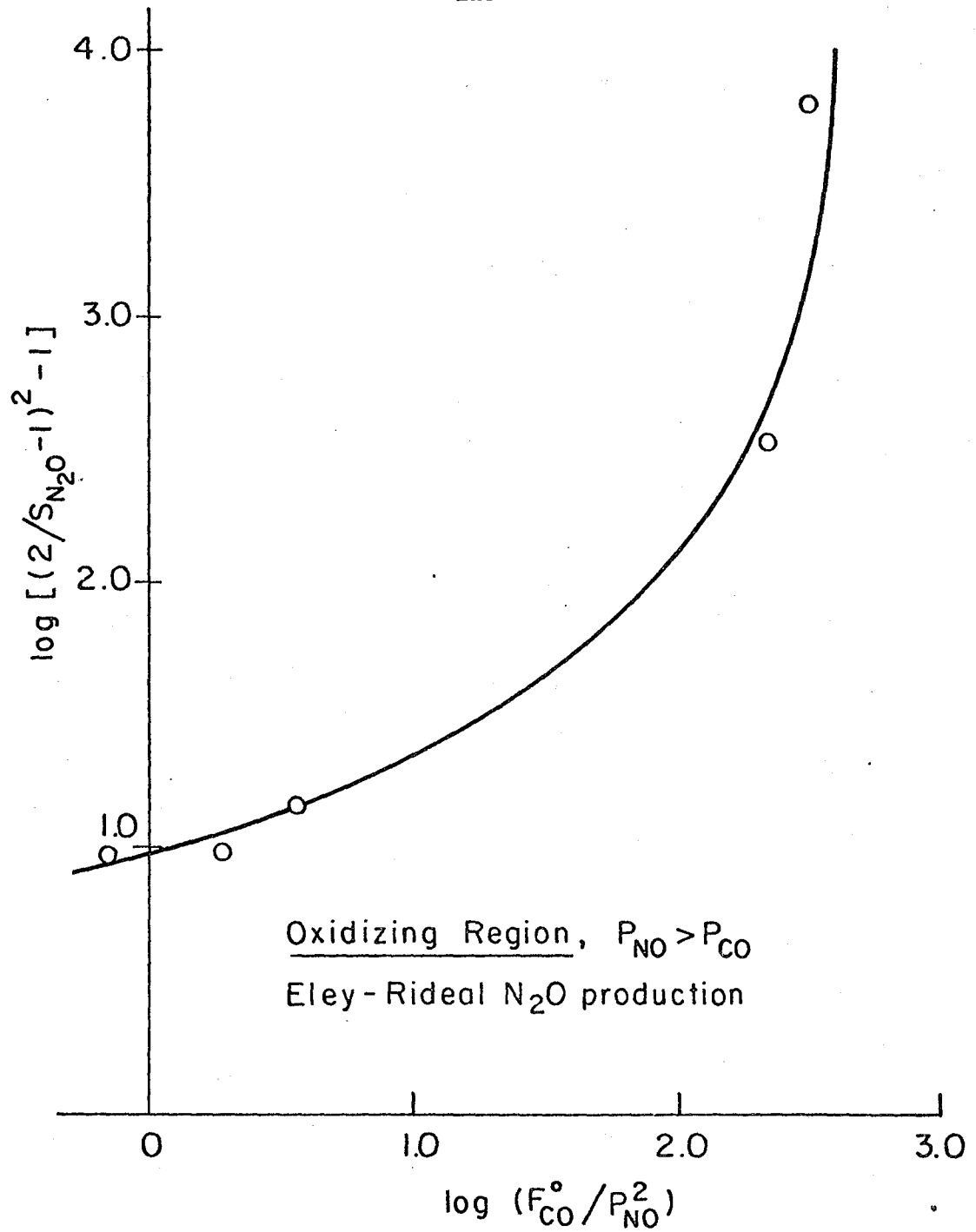
XBL 786-5122

Fig. 31

to correlate the data, no distinction can be made regarding the importance

of the two reaction paths.

E.   Investigation of the Deactivation Process

One of the more interesting aspects of this study involved the

investigation of the catalyst deactivation. Three chemical species

were considered as possible contributors to the deactivation process.

These were adsorbed oxygen atoms, adsorbed carbon atoms and the isocyanate

species (NCO). The extent to which each of the three contributes

to the deactivation is discussed in detail below.

1.   Oxygen

Katzer (34) observed significant catalyst deactivation in a study

of NH_3 oxidation by NO, which was attributed to the formation of a

very stable Pt-O species. In this study, it was found that the catalyst

could be reactivated by reduction in H_2, even though the deactivation

process proceeded under highly reducing conditions.

The stability of the Pt-O species and the behavior of oxygen

on Pt surfaces has been the subject of many recent publications.

Stable platinum oxide species have been observed by Monroe (35) and

others (36, 37, 38). Nitric oxide adsorption and decomposition studies

reported by Pirug and Bonzel (6) and Amiranazmi and Boudart (39) conclude

that adsorbed oxygen inhibits NO dissociation through the formation

of a stable surface oxide. Since NO dissociation appears to be the

rate limiting step in the reducing region, the possibility of the

Pt-O species being responsible for the deactivation is quite realistic

in the light of the previously mentioned literature.

To test the susceptibility of the catalyst to deactivation by a surface oxygen species, attempts were made to poison the catalyst surface by pretreatment with NO and O_2 prior to the introduction of the reactants. In each case, a 5 hr pretreatment with either NO (at a concentration of 5 mole% in He) or oxygen (20 mole% in He) at $300^{\circ}C$ failed to deactivate the catalyst. Upon introduction of reactant mixture (10% CO, 5% NO in He) following the pretreatment, the catalyst exhibited a deactivation very similar to that observed for runs made with the standard oxidation/reduction pretreatment. This behavior is shown in Figure 32.

The results of the oxidation pretreatment experiments strongly suggest tht the Pt-O species cannot be responsible for the catalyst deactivation. If this species were indeed the poison, the NO pretreatment should have deactivated the catalyst via the same process (i.e. NO dissociation) that occurs under reaction conditions. In addition, further experiments (explained in detail below) indicate that catalyst reactivation can be accomplished without reduction, and that therefore it is highly unlikely that the deactivation is caused by an adsorbed oxygen or Pt-O species.

Furthermore, if NO dissociation were responsible for the formation of an oxide adspecies, then an excess of nitrogen containing products should have been observed (i.e., R_s values greater than one). Thus it is difficult to explain the large excess CO_2 production observed experimentally. It is conceivable, however, that excess CO_2 is produced by a side reaction in which the activity declines in a manner

Figure 32.   Effect of nitric oxide pretreatment on catalyst

deactivation.
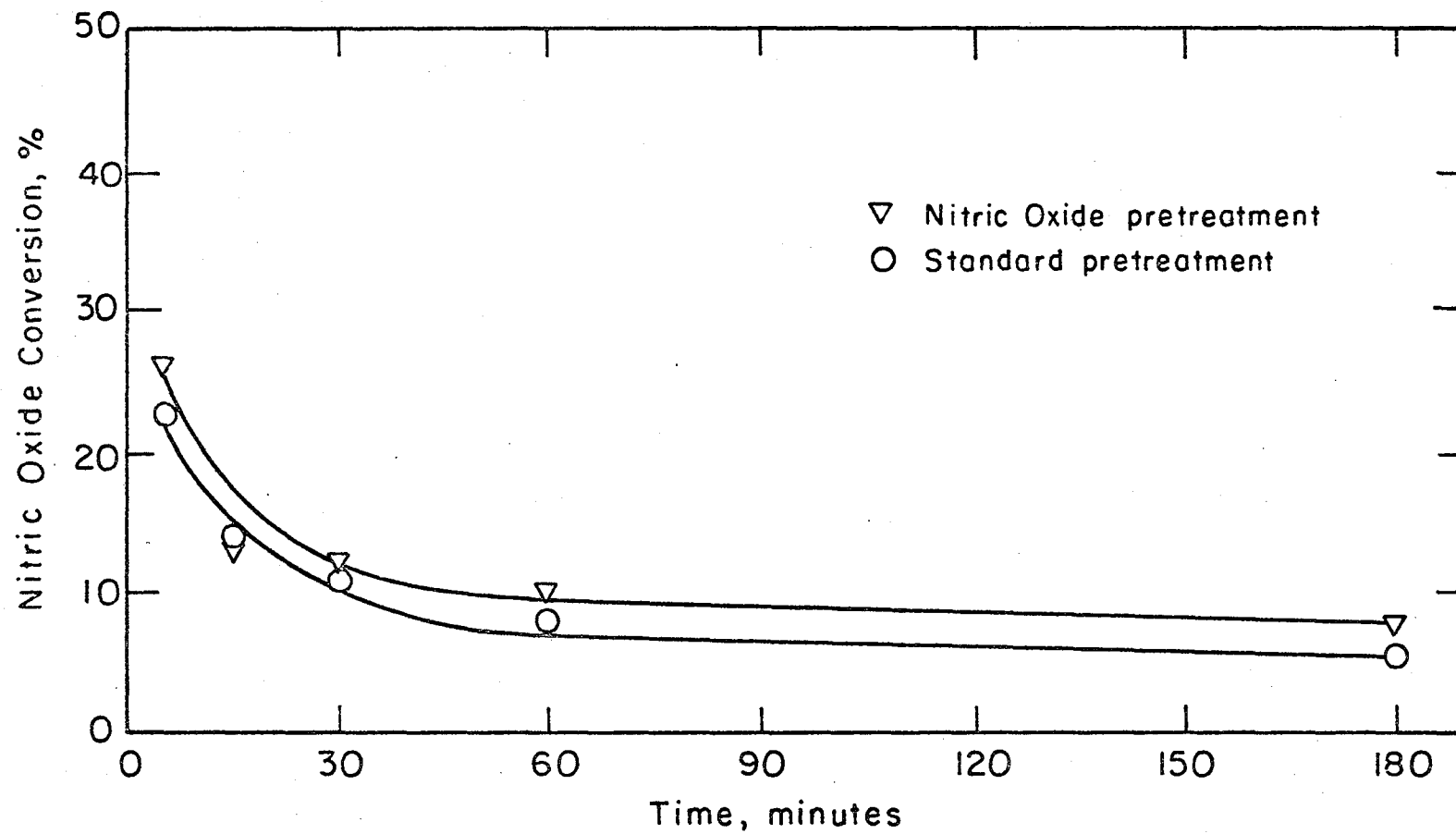
XBL 786-5199

Fig. 32

similar to the main NO reactions. In this case the large amount of excess CO_2 would tend to overwhelm any observable oxide formation. This is more likely to be true if the same sites are responsible for both the main (NO) and side (excess CO_2) reactions, and if these sites are small in number compared to the total number of surface sites. Under these conditions the poisoning could occur by an oxidation process and not be detected via product distributions, but one would still expect to be able to poison these sites by prior NO pretreatment.
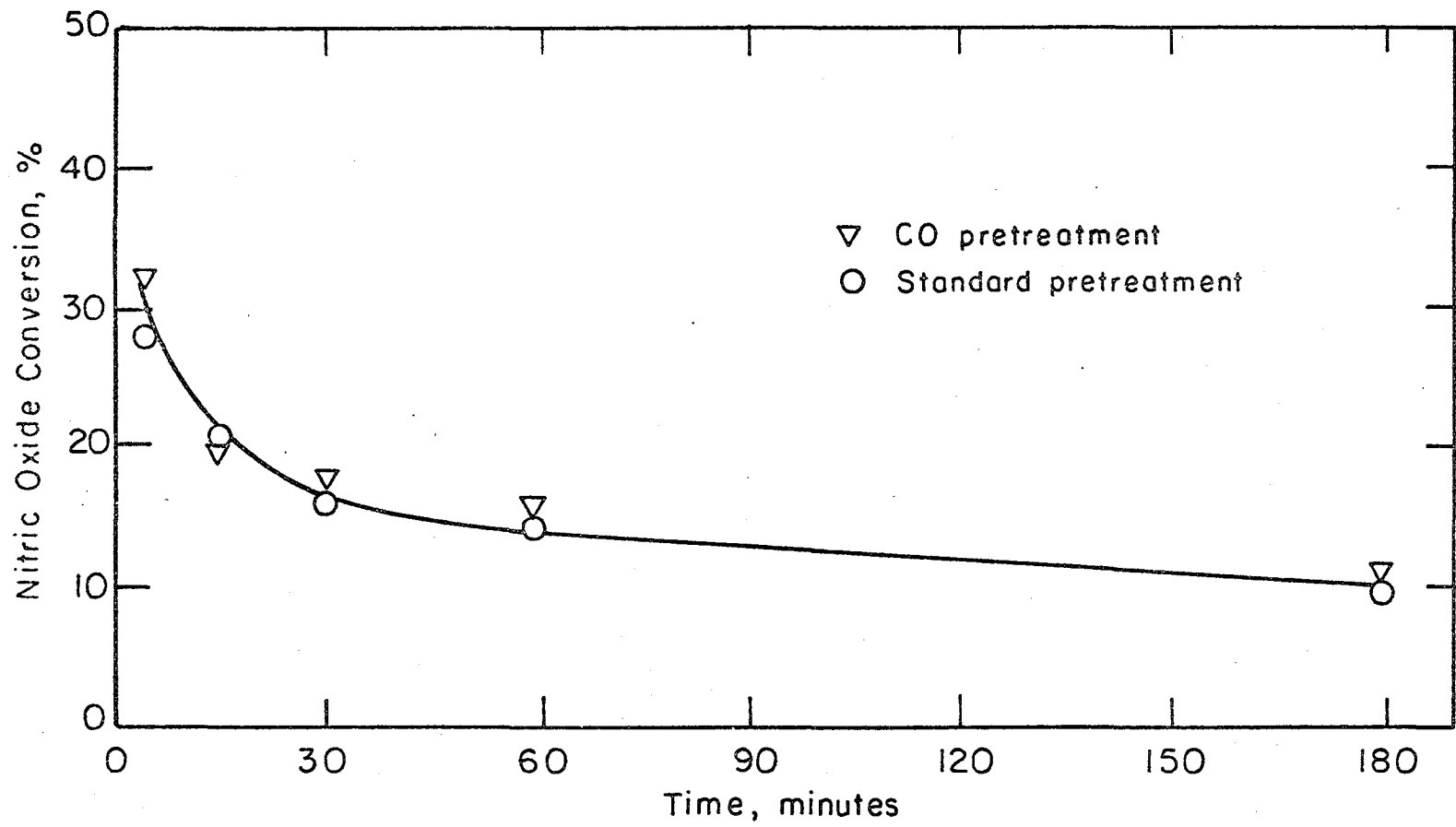
2. <u>Carbon</u>

The second species considered with respect to its role in the deactivation process was carbon. Production of surface carbon via CO dissociation would result in excess CO_2 formation according to equation (6). Somorjai et al (4) have reported CO dissociation at coordinately unsaturated (step and kink) sites on a platinum surface.

In order to test the susceptibility of the catalyst to deactivation by CO dissociation, an attempt was made to deactivate the catalyst by CO pretreatment. Prior to the CO pretreatment, two reference runs (KOR-35, 36) were made for comparison. After these runs, the catalyst was pretreated in the usual manner, followed by a two hour pretreatment of 10 mole% CO in He at $300^{O}C$. The CO pretreatment was followed by a 30 min He purge, prior to introduction of the reactants (10% CO, 5% NO in He).

The results of this experiment are shown in Figure 33, in which NO conversion is plotted as a function of time for the reference runs (KOR-35/36) and the CO pretreatment run (KOR-37). The results shown in this figure indicate that the pretreatment had very little effect

Figure 33.   Effect of carbon monoxide pretreatment on catalyst

deactivation.

XBL 786-5200

Fig. 33

on the initial activity of the catalyst. This evidence suggests that
the deactivation process is not due to the build up of a carbon species
formed by CO dissociation.

One of the main reasons for considering the possibility of carbon
formation was the observed excess CO_2 production. However, the data
presented in Table 5 indicate that significant amounts (at least one
monolayer) of surface carbon would have to be produced to account
for the total integrated excess CO_2 production. This is not likely
since no change in the CO infrared band intensity was observed, which
indicates that a large percentage of the Pt surface was still covered
with adsorbed CO. In order to reconcile both the infrared observations
and the integrated excess CO_2 quantities, it would be necessary to
propose a carbon structure that could grow to large (up to 5 monolayers)
proportions and still occupy very little Pt surface. Additionally,
this carbon structure would have to be reactive enough to be removed
by the rather mild standard pretreatment conditions, in order to keep
from eventually clogging up the catalyst. The existence of such a
structure is highly unlikely, and as a result the evidence presented
here does not support the production of excess CO_2 via CO dissociation
and surface carbon formation.

Further evidence suggesting that carbon deposition does not contri-
bute to the cause of the deactivation was contributed by the following
set of experiments. Following the 3 hr run KOR-37 mentioned above,
the flow of CO was discontinued, while feeding a mixture of approximately
5 mole % NO in He to the reactor (at 300°C). This condition was maintained
for three hours, while montoring the infrared spectra to observe the

effect of NO on the isocyanate band. Following the NO treatment period, the system was purged with He for 8 to 10 hours. Next, the reactant feed mixture (approximately 10% CO, 5% NO, in He) was introduced, omitting the standard pretreatment. The results of this run (labeled KOR-38A) are shown in Figure 34. The conditions in run KOR-38A were monitored for 60 minutes, at which time the CO was turned off, allowing the 5% NO in He stream to continue for 20 minutes. At the end of this period, the reactor was purged with pure He for 20 minutes, then the same reactant feed mixture (used in KOR-38A) was reintroduced. This run (labeled KOR-38B) is also shown in Figure 34.

The main conclusion to be drawn from Figure 34 is that even though KOR-38A underwent a typical deactivation, the brief 20 minute 5% NO purge was sufficient to reactivate the catalyst. The excess CO_2 produced in the 60 minute period (KOR-38A) was over 260 micromoles. It is unlikely that this much carbon could have been removed in such short time and under relatively mild oxidation conditions.

3. Isocyanate Species

The results of the previously described reactivation experiments along with infrared observations prompted a consideration of the isocyanate species as a possible contributor to the deactivation process. The proposition that the isocyanate species contribute to a loss in activity during NO reduction by CO had been noted by Niiyama et al (16) previously. These authors observed the transient deactivation of a Pt/Al_2O_3 catalyst and the reactivation of the catalyst in a short (<30 min) period of time by H_2O injection. The authors also recorded infrared spectra in which they observed the increasing intensity of a band near 2300 cm^{-1}

Figure 34.   Nitric oxide conversion as a function of time for
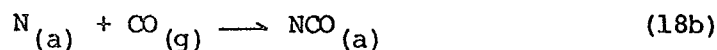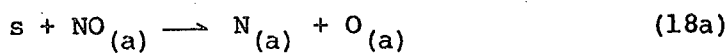
runs KOR-38A and KOR-38B.
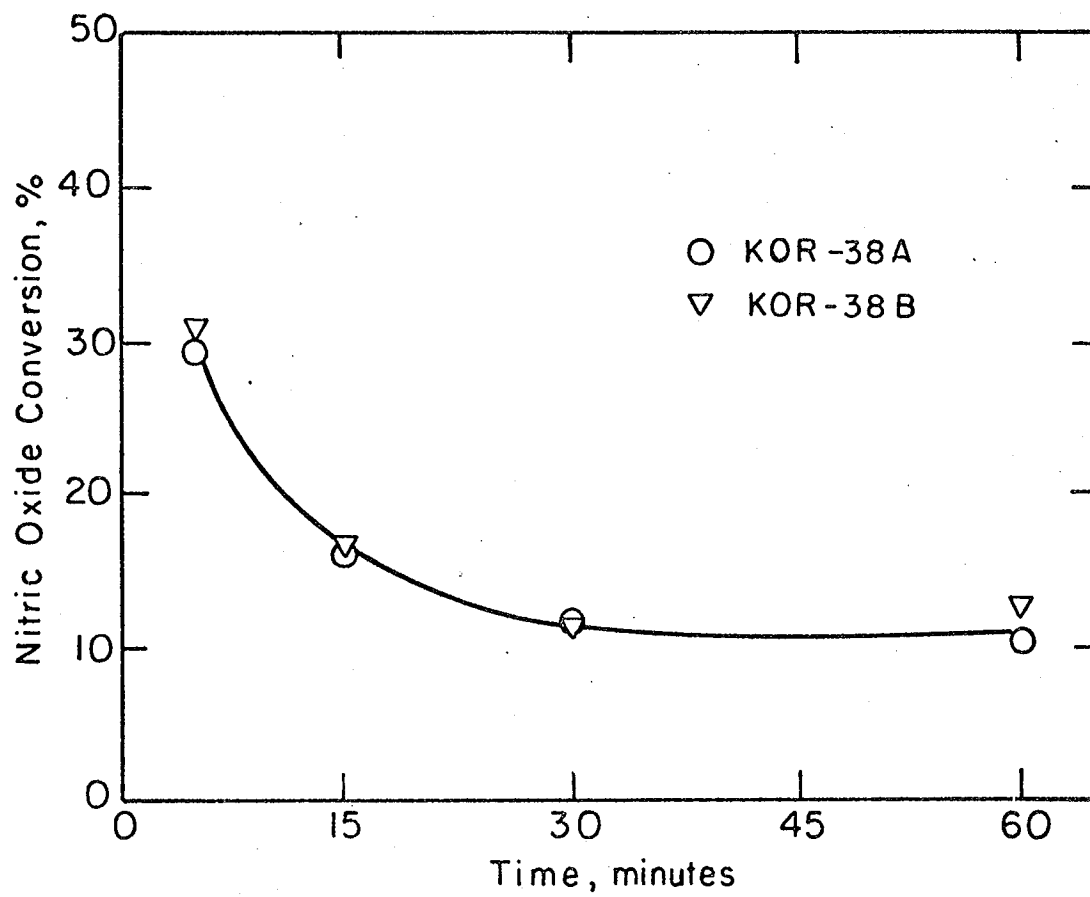
XBL786-5198

Fig. 34

(identified as Pt-NCO) as the deactivation proceeded. As a result
of these and other observations, Niiyama and coworkers concluded that
the poisoning was due to the formation of a Pt-NCO species.

Formation of the isocyanate species on the Pt surface is believed
to occur according to the reactions:

$$s + NO_{(a)} \longrightarrow N_{(a)} + O_{(a)} \qquad (18a)$$

$$N_{(a)} + CO_{(g)} \longrightarrow NCO_{(a)} \qquad (18b)$$

If the removal of the adsorbed oxygen atoms is taken into account,
then the overall stoichiometry for isocyanate formation is:

$$Pt + NO + 2CO \longrightarrow Pt\text{-}NCO + CO_2 \qquad (19)$$
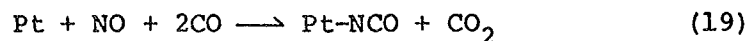
The reaction sequence (18a, b) has been proposed by Unland (17) for
isocyanate formation on Pt and is consistent with the mechanism presented
earlier (Figure 28). An altnerative mechanism has been proposed by
Harrison and Thornton (40) for isocyanate production over a tin oxide/
copper oxide catalyst:

$$CO_{(g)} \longrightarrow C_{(a)} + O_{(a)} \qquad (20)$$

$$C_{(a)} + NO_{(g)} \longrightarrow s\text{-}CNO_{(a)} \qquad (21)$$

$$s\text{-}CNO \longrightarrow s^{+}\text{-}C \underset{O}{\overset{N}{\underset{|}{<}}}^{-} \longrightarrow s\text{-}NCO \qquad (22)$$
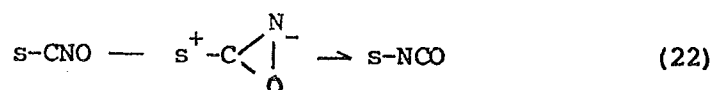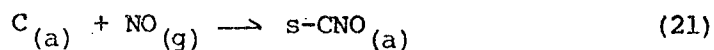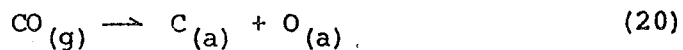
which proceeds via dissociation of CO followed by the reaction of

the adsorbed carbon fragment with NO (Eq. 21) and a rapid isomerization

of the resultant fulminate to the stable isocyanate structure, via

a cyclic oxaziranyl intermediate (Eq. 22). This mechanism is not

likely to be important for a Pt catalyst due to the necessity of CO

dissociation.

An important consequence of the Pt-NCO formation is the production

of excess CO_2 (Eq. 19). Since for every NCO molecule formed a molecule

of CO_2 is produced, one is faced with a dilemma similar to that considered

in the case of carbon formation. Judging by the excess CO_2 production,

the large amounts of NCO formed make it difficult to rationalize that

this material remains on the Pt surface, since the growth of the infrared

isocyanate band does not affect the CO band intensity or frequency.

If signifcant quantities of the NCO species were present on the Pt

surface, not only would one also expect to see a decrease in CO band

intensity, but one also expect to see a frequency shift due to the

interaction of the NCO species on the adsorbed CO (41). The

very large accumulated NCO infrared band intensities are consistent

with the greater than monolayer excess CO_2 formation, and cannot be

due to a species adsorbed on the Pt surface, since the size of the

2300 cm^{-1} band is often larger than the corresponding CO band (assuming

comparable extinction coefficients).

The dilemma concerning the site of adsorption of the isocyanate

species can be resolved if we consider that this structure is not

on the Pt surface, but rather on the silica support. The support has

many times the surface area of the catalyst, and could provide a large

reservoir for any species with which it could bond. Direct evidence for the existence of a stable isocyanate species bonded to the silica support has been obtained in this study (section C-1), and this observation is supported by work published by Eley et al (21) and others (42, 43, 22, 20), described in detail below.

Eley, et al. (21) have published infrared spectra following the dissociative adsorption of ethyl isocyanate on silica. They observed very intense bands at 2308 cm^{-1} and 2210 cm^{-1} and attributed these bands to Si-NCO and surface cyanide (CN) groups, respectively. Isotopic substitution experiments and calculations performed by Morrow and Cody (42) confirm the frequency assignments made by Eley et al Eley and co-workers have also observed the removal of 2308 cm^{-1} and 2210 cm^{-1} bands by exposure to water vapor at $25^{o}C$.

Guillet et al (22) have published a similar study involving the dissociative adsorption of n-butyl isocyanate on both silica and alumina surfaces. Also reported are infrared spectra of HNCO adsorption on silica and alumina. Intense infrared bands observed at 2300 cm^{-1} to 2310 cm^{-1} on silica and 2270 cm^{-1} on alumina were attributed to adsorbed NCO species. These findings (for alumina) are in good agreement with studies of Pt/Al_2O_3 catalysts, reported by Dalla Betta and Shelef (20) and Solymosi et al (44), who have identified infrared bands at 2260 cm^{-1} and 2267 cm^{-1}, respectively, as belonging to a support bonded isocyanate species. Dalla Betta and Shelef (20) have also reported an isocyanate band for Pt/SiO_2 at 2304 cm^{-1}, and attribute this band to an isocyanate species bonded to the silica support.

Under some conditions, very large NCO bands appeared to split, resolving into bands at 2330 cm^{-1} and 2290 cm^{-1}. Such a split (see Figure 25) is not evident in spectra published by Eley et al (21), however a shoulder at approximately 2350 cm^{-1} is present. After replacement of the reactants (NO and CO) with He, the split peaks merged into a single peak at 2300 cm^{-1}. No infrared data has been published for Pt-NCO on an unsupported metal, although the frequency (ν_a(NCO)) for $\left[(C_6H_5)_3P \right]_2 Pt(NCO)_2$ has been reported (45) to be 2234 cm^{-1}. At this time the explanation of the splitting is not clear, and it is not known whether the splitting is associated with species solely on the support, or whether perhaps isocyanate species on the Pt surface are involved. It is not likely that small amounts of Pt-NCO would be observable against the large background intensity of the Si-NCO.

A model for the catalyst deactivation under reducing conditions can now be proposed. The deactivation is believed to involve the transient build-up of the isocyanate species on the Pt crystallites. Due to the high CO gas phase partial pressures, a large percentage of the catalyst surface will be covered with CO, leaving only a small fraction of the surface sites remaining for NO adsorption and dissociation. Since the rate of NO dissociation (and therefore the overall rate) is proportional to the vacant site concentration (θ_v), the build-up of the relatively non-reactive NCO species will cause a drop in observed catalytic activity through the occupation of vacant sites. As a result of the small number of vacant sites present under reducing conditions, very small NCO surface coverages can have a significant effect on the overall rate.

The transient activity of the catalyst can be explained by considering the transient formation and diffusion of the isocyanate. The problem is much too complex to be treated analytically, without knowledge of NCO diffusion coefficients, reaction rates, or site concentrations. Only a qualitative description can be offered at this time. Initially, the rate of NCO production will be at a maximum, since the concentration of NCO on the support near the crystallites wll be close to zero. This is true, assuming that the diffusion on the silica is much slower than diffusion on the Pt. As the concentration of NCO builds up on the support near the crystallites, the NCO concentration will begin to rise on the crystallites (decreasing θ_v), resulting in a drop in activity and a subsequent drop in NCO formation. This process will continue until the rate of formation equals the overall rate of diffuson away from the crystallite. At this time, the activity will reach a steady state value.

Experimental observation of the isocyanate production rate can be derived from the excess CO_2 production rates, assuming that all the excess CO_2 is due to NCO formation. In this case, the rate of excess CO_2 production equals the rate of NCO production. Interpretation of Figure 17 in this manner indicates that the NCO production behavior is consistent with the proposed diffusion model. It is interesting to note that the maximum NCO formation rate ($t=5$ min) is roughly 20% of the total NO conversion ($t=5$ min, based on the nitrogen products N_2 and N_2O). This indicates that isocyanate production is not a major competitor for adsorbed nitrogen atoms, however it may have an effect on N_2O selectivity, especially at times close to zero.

The experimentally observed reactivaton of the catalyst also can be explained by the proposed deactivation mechanism. Once the reactants NO and CO have been removed from contact with the catalyst, the NCO formation ceases, and the NCO species continue to diffuse until the concentration has equilibrated on the silica support. The higher chemical stability of the Si-NCO species provides the driving force for the diffusion off the Pt crystallites. This process may explain why the initial activity can be regained independent of whether oxidizing or reducing conditions are used during pretreatment.

It is also suspected that the Pt-NCO species may react with NO (in absence of CO) to give N_2 and CO_2:

$$Pt-NCO + NO \longrightarrow Pt + CO_2 + N_2 \qquad (23)$$
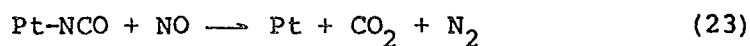
even though the Si-NCO species is non-reactive toward NO. This reaction was proposed by Unland (17) to explain the lack of NCO infrared bands when mixtures of excess NO were dosed over Pt/Al_2O_3. It is likely that reaction 23 above is much slower than NCO production (reaction 18b) in the presence of CO. In the oxidizing region investigated in this study, where CO partial pressures were very low and NO partial pressures high, reaction 23 may be responsible for the much lower levels of NCO observed.

It is interesting to note that Niiyama et al (16) observed the deactivation in 3% NO, 1% CO reaction mixture. In this case, the CO partial pressure is probably still high enough to maintain the NCO production faster than the decomposition. The CO partial pressure

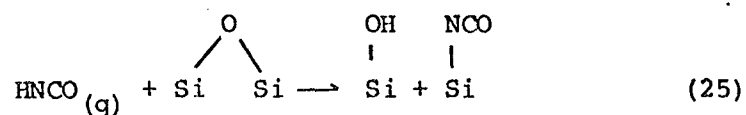under these conditions is sufficient to keep the majority of the Pt surface covered with adsorbed CO. As a result, Θ_v will be small and any Pt-NCO build-up will reduce activity, as was observed in this study for reducing conditions. It must be emphasized that the oxidizing conditions in this study were highly oxidizing, and the high catalyst activity was most likely a result of the decreased CO surface coverage as well as reduced Pt-NCO formation. Unland (17) dosed by filling a constant volume reactor with 100 torr of reaction mixture for a period of 30 minutes prior to observing the infrared spectra. Examination of the spectra published in (17) shows a very small CO band for an initial dose of 10% NO, 5% CO in N_2, indicating that the CO partial pressure was very small at the time the spectrum was taken. As a result, Unland's conditions were much closer to the oxidizing conditions in this study than those of Niiyama et al (16). The important point to be made here is that the isocyanate formation is dependent on the ratio and magnitude of P_{NO} and P_{CO} for oxidizing conditions over the catalyst, not the stoichiometry of the feed or the initial composition of a dosing mixture.

Thus far no explanation has been given to account for the gas phase transport of the NCO species. The observation of the Si-NCO band on the reference IR disk definitely indicates that some type of gas phase transport does occur. The most likely species to be found in the gas phase is isocyanic acid (HNCO), or its trimer forms:

$$
\begin{array}{ccc}
& H & \\
O & N & O \\
\diagdown & \diagup\diagdown & \diagup \\
C & & C \\
| & & | \\
HN & & NH \\
\diagdown & & \diagup \\
& C & \\
& \| & \\
& O &
\end{array}
\quad \rightleftharpoons \quad
\begin{array}{ccc}
HO & N & OH \\
\diagdown & \diagup\diagdown & \diagup \\
C & & C \\
\| & & | \\
N & & N \\
\diagdown & & \diagup \\
& C & \\
& | & \\
& OH &
\end{array}
\qquad (24)
$$
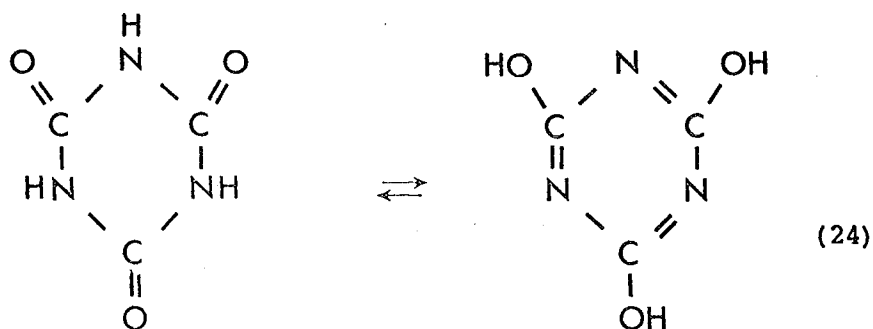
isocyanuric acid $\rightleftharpoons$ cyanuric acid

The trimer form converts to HNCO at approximately 330°C (46). Formation of HNCO might occur through reaction of Si-NCO with hydrogen supplied by a hyroxyl group on the silica surface, since the reverse process, adsorption of HNCO on silica, has been observed (18):

$$
\mathrm{HNCO}_{(g)} + \underset{\underset{\displaystyle Si\quad\quad Si}{\diagup\diagdown}}{\overset{\displaystyle O}{}} \longrightarrow \underset{\underset{\displaystyle Si}{|}}{\overset{\displaystyle OH}{}} + \underset{\underset{\displaystyle Si}{|}}{\overset{\displaystyle NCO}{}} \qquad (25)
$$

To what extent the formation of HNCO occurred in this study is not known, and it is likely that the amounts of HNCO produced were dependent on the concentration and reactivity on th OH groups on the Si surface. However, the formation and decomposition of HNCO is not expected to represent a major NCO transport mechanism due to the stability of the observed infrared isocyanate bands. Long periods under constant He purge at 300°C appeared to have little effect on the intensity of the 2300 cm^{-1} bands. Eley et al (21) observed the desorption of the 2300 cm^{-1} and 2210 cm^{-1} bands at high temperatures and found very little decrease in the infrared band intensities at temperatures up to 500°C in vacuo.

Many authors (17-19, 20, 47, 48) have recently pondered the role

of isocyanate formation in the production of NH_3 over noble metal

catalysts. The results presented in this study in conjunction with

work reported by Voorhoeve et al (48) may help to shed some additional

light on this subject. Voorhoeve et al (48) have studied the reaction

of H_2, CO, and NO over supported and unsupported Pt catalysts, and

have obtained some very interesting results. These authors found

that reaction of a mixture of 0.3% NO, 0.5% H_2, and 5% CO in He over

an unsupported Pt catalyst resulted in 100% NO conversion to ammonium

cyanate (NH_4 OCN). Exposure of the same reactant mixture to an alumina

supported Pt catalyst produced no NH_4OCN, only NH_3. The authors concluded

that NCO groups formed on the Pt surface were converted to NH_3 by

hydrolysis after migration to the alumina support. Evidence and mechanisms

concerning the migration of NCO groups described in the present work

strongly support this hypothesis.

Hydrolysis of the silicon isocyanate species was observed in

this study at $25^\circ C$. The formation of ammonia is described in the

following overall reaction:

$$Si\text{-}NCO + 2H_2O \longrightarrow NH_3 + CO_2 + Si\text{-}OH \qquad (26)$$
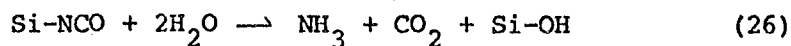
In addition to ammonia, HNCO can also be formed according to reaction

25 mentioned above:

$$Si\text{-}NCO + Si\text{-}OH \longrightarrow HNCO + Si\text{-}O\text{-}Si \qquad (25)$$
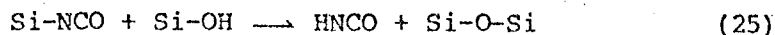
The production of cyanide groups during hydrolysis, as observed by the growth of the 2200 cm^{-1} in Figure 27, indicates that the following reaction may be occurring:

$$2 \text{ Si} + H_2O + \text{Si-NCO} \longrightarrow \text{Si-CN} + 2 \text{ Si-OH} \qquad (27)$$
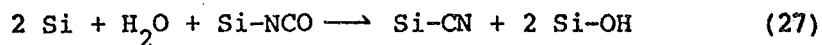
The cyanide groups formed in reaction 27 can react further and produce ammonia according to:

$$\text{Si-CN} + 3 \text{ Si-OH} \longrightarrow NH_3 + CO_2 + 2 \text{ Si} + \text{Si-O-Si} \qquad (28)$$
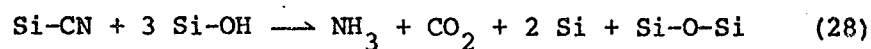
This reaction does not appear to proceed to a large extent at $25^{\circ}C$, since the spectra (in Figure 27) do not reveal a decrease in the 2200 cm^{-1} band intensity during prolonged exposure to water. It is likely, however, that reaction 28 does proceed upon heating. This would account for the removal of the 2200 cm^{-1} band in the spectrum represented by curve e, Figure 27. The importance of reaction 25 in comparison to reaction 26 was not determined in this study, since neither of the products (NH_3 and HNCO) could be detected with the chromatographic analysis system.

IV. CONCLUSIONS

The following conclusions can be stated with regard to the kinetics

and product selectivities observed in this study. Under reducing

conditions, the overall nitric oxide reaction rate was found to be

first order in P_{NO} and inverse second order in P_{CO}. A reaction mechanism

based on the dissociation of nitric oxide as the rate limiting step

was used to correlate nitric oxide reaction rates and product selectivities.

As a part of the mechanism, the assumption of a Langmuir-Hinshelwood

process for the formation of nitrous oxide was found to correlate

the selectivity data. The Langmuir-Hinshelwood process involves the

reaction of an adsorbed nitrogen atom with an adsorbed nitric oxide

molecule. Under highly oxidizing conditions, the overall rate becomes

positive order in P_{CO}. It was not possible to correlate either rate

or selectivity expressions for the oxidizing regime.

The transient catalyst deactivation observed under reducing con-

ditions can be qualitatively described utilizing a simple model.

The essential part of the model is the formation of an isocyanate

species on the Pt crystallites and the subsequent diffusion of these

species to the silica support. The deactivation is the result of

a transient isocyanate build-up on vacant Pt sites, thereby inhibiting

the dissociation of nitric oxide. This process is aggravated by the

high CO coverages present under reducing conditions. The isocyanate

deactivation mechanism points out the importance of the catalyst support

in the reduction of NO by CO over Pt. Since the hydrolysis of silicon

isocyanate produces ammonia and is easily accomplished at $25^{\circ}C$, the

catalyst support may also have an important role during the formation

of ammonia in the presence of water and hydrogen.

ACKNOWLEDGMENTS

APPENDICES

Appendix 1

Flow System Calculations

Flow in a capillary can be described with the Hagen-Poiselle equation:

$$Q = \frac{\pi R^4}{8 \, L\mu} \Delta P \tag{1-1}$$

where

Q = volumetric flow rate, cm^3/sec

R = capillary radius, cm

L = capillary length, cm

P = pressure drop across capillary, $dynes/cm^2$

μ = viscosity, poise

For constant R, L, and μ, the volumetric flow rate is proportional to the pressure drop across the capillary,

$$Q = K \, \Delta P \tag{1-2}$$

where

K = flow factor

= $\pi R^4/8 \, L\mu$

If the capillary is at a pressure other than atmospheric, then the flow rate at atmospheric pressure, Q_o, is related to ΔP by:

$$Q_o = K \, \Delta P (1 + P'/P_o) \tag{1-3}$$

where

P_o = barimetric pressure

P' = capillary pressure

Calibration of the capillary was performed by experimentally determining
K for a reference gas such as He, then the value of K for other gases
such as NO and CO was calculated using:

$$\mu_i \, K_i = \mu_{He} \, K_{He}$$

$$K_i = \frac{\mu_{He}}{\mu_i} \, K_{He}$$

(1-4)

Equation 1-4 can also be used to correct the flow factors for temperature,
if values of $\mu_i(T)$ are available.

Appendix 2

Derivation of R_{N_2}/R_{N_2O} Selectivity Relationships, Reducing Region

A. Eley-Rideal N_2O Production, $P_{CO} > P_{NO}$

The reactions pertaining to the following development are reactions 1-4, 5a, and 6 in Figure 28.

The site balance including all surface species is:

$$1 = \theta_v + \theta_O + \theta_{NO} + \theta_{CO} + \theta_N \qquad (2-1)$$

where the fractional surface concentrations are denoted by:

θ_v = vacant site concentration

θ_O = adsorbed oxygen atom concentration

θ_{NO} = adsorbed NO molecule concentration

θ_{CO} = adsorbed CO molecule concentration

θ_N = adsorbed nitrogen atom concentration

Assuming θ_O, θ_{NO}, and θ_N are small compared to θ_{CO}, equation (2-1) reduces to:

$$1 \simeq \theta_v + \theta_{CO} \qquad (2-2)$$

From Figure 28, reactions 4 and 5a, the ratio of N_2 to N_2O production rates is:

$$\frac{R_{N_2}}{R_{N_2}} = \frac{k_4\theta_N}{k_5 P_{NO}} \qquad (2-3)$$

Assuming there is no build-up of adsorbed nitrogen atoms on the surface, the production rate must equal the reaction rate, therefore:

$$k_3\theta_{NO}\theta_v = k_4 \theta_N^2 + k_5 \theta_N P_{NO} \qquad (2-4)$$

Assuming reactions 1 and 2 in Figure 28 are at equilibrium, the following expressions are obtained:

$$\frac{\theta_{NO}}{P_{NO}\theta_v} = K_2, \quad \theta_{NO} = K_2 P_{NO}\theta_v \tag{2-5}$$

$$\frac{\theta_{CO}}{P_{CO}\theta_v} = K_1 \tag{2-6}$$

Combining equations 2-2 and 2-6;

$$\theta_v = \frac{1}{1 + K_1 P_{CO}} \tag{2-7}$$

Combining equations 2-5 and 2-7 and substituting into 2-4 yields:

$$k_4\theta_N^2 + k_5 P_{NO}\theta_N - \frac{k_3 K_2 P_{NO}}{(1 + K_1 P_{CO})^2} = 0 \tag{2-8}$$

Solving the quadratic equation above for θ_N yields:

$$\theta_N = \frac{k_5 P_{NO}}{2k_4}\left[\left(1 + \frac{4k_4 k_3 K_2}{k_5^2(1+K_1 P_{CO})^2 P_{NO}}\right)^{1/2} - 1\right] \tag{2-9}$$

Substitution of 2-9 into 2-3 results in the final expression for R_{N_2}/R_{N_2O}:

$$\frac{R_{N_2}}{R_{N_2O}} = \frac{1}{2}\left[\left(1 + \frac{4k_4 k_3 K_2}{k_5^2(1+K_1 P_{CO})^2 P_{NO}}\right)^{1/2} - 1\right] \tag{2-10}$$

The N_2O selectivity can be expressed in terms of this R_{N_2}/R_{N_2O} ratio:

$$S_{N_2O} = \frac{1}{R_{N_2}/R_{N_2O} + 1} ,$$ (2-11)

$$\frac{R_{N_2}}{R_{N_2O}} = \frac{1}{S_{N_2O}} - 1$$

The relationship presented in Table 6 is derived by the combination and rearrangement of equations 2-10 and 2-11:

$$\left\{ \frac{1}{P_{NO}\left[\left(\frac{2}{S_{N_2O}} - 1\right)^2 - 1\right]} \right\}^{1/2} = \frac{k_5}{4k_4k_3K_2} (1 + K_1P_{CO})$$ (2-12)

B. Langmuir-Hinshelwood N_2O Production, $P_{CO} > P_{NO}$

The reactions pertaining to the following derivation are 1-4, 5b, and 6 in Figure 28. From this figure, by inspection of reactions 4 and 5b, the ratio of N_2 to N_2O production rates is:

$$\frac{R_{N_2}}{R_{N_2O}} = \frac{k_4\theta_N^2}{k_5\theta_N\theta_{NO}} = \frac{k_4}{k_5} \frac{\theta_N}{\theta_{NO}}$$ (2-13)

Assuming that nitrogen atom surface concentration is at steady-state, the rate of production equals the rate of reaction, and:

$$k_3 \theta_{NO} \theta_v = k_4\theta_N^2 + k_5 \theta_N\theta_{NO}$$ (2-14)

Dividing through by θ_{NO}^2 and rearranging yields:

$$k_4\left(\frac{\theta_N}{\theta_{NO}}\right)^2 + k_5\left(\frac{\theta_N}{\theta_{NO}}\right) - k_3 \frac{\theta_v}{\theta_{NO}} = 0$$ (2-15)

Solving equation 2-5 for θ_v/θ_{NO} and substituting into 2-15 above yields:

$$k_4 \left(\frac{\theta_N}{\theta_{NO}}\right)^2 + k_5 \frac{\theta_N}{\theta_{NO}} - \frac{k_3}{K_2 P_{NO}} = 0 \qquad (2-16)$$

Using the quadratic equation to solve for θ_N/θ_{NO}, one obtains:

$$\frac{\theta_N}{\theta_{NO}} = \frac{k_5}{2k_4} \left[\left(1 + \frac{4k_4 k_3}{k_5^2 K_2 P_{NO}}\right)^{1/2} - 1\right] \qquad (2-17)$$

Substituting 2-17 into 2-13 yields:

$$\frac{R_{N_2}}{R_{N_2O}} = \frac{1}{2} \left[\left(1 + \frac{4k_4 k_3}{k_5^2 K_2 P_{NO}}\right)^{1/2} - 1\right] \qquad (2-18)$$

Substituting 2-18 into 2-11 and re-arranging produces the expression:

$$\left(\frac{2}{S_{N_2O}} - 1\right)^2 - 1 = \frac{4k_4 k_3}{k_5^2 K_2} \left(\frac{1}{P_{NO}}\right) \qquad (2-19)$$

presented in Table 6.

Appendix 3

Derivation of R_{N_2}/R_{N_2O} Selectivity Relationships, Oxidizing Region

A. Eley-Rideal N_2O production, $P_{NO} > P_{CO}$

The site balance for the entire Pt surface is:

$$S_T = S_{NO} + S_{CO} + S_N + S_O + S_V \qquad (3-1)$$

where:

S_T = total number of surface sites

S_{NO} = number of sites occupied by NO

S_{CO} = number of sites occupied by CO

S_N = number of sites occupied by nitrogen atoms

S_O = number of sites occupied by oxygen atoms

S_V = number of vacant sites

Assuming that S_{CO} is approximately constant, then $S_T - S_{CO}$ is constant,

$$S_T - S_{CO} = S_N + S_O + S_{NO} + S_V \qquad (3-2)$$

Dividing by $S_T - S_{CO}$:

$$1 = \theta_N + \theta_O + \theta_{NO} + \theta_V \qquad (3-3)$$

where the θ's are fractional coverages based on $S_T - S_{CO}$ number of sites. Under highly oxidizing conditions, reaction 6 in Figure 28 is assumed rate limiting and the site balance 3-3 is reduced to:

$$1 \approx \theta_O + \theta_V \qquad (3-4)$$

The expression for the ratio R_{N_2}/R_{N_2O} is the same as equation 2-3 presented earlier in Appendix 2:

$$\frac{R_{N_2}}{R_{N_2O}} = \frac{k_4}{k_5} \frac{\theta_N}{P_{NO}} \tag{3-5}$$

Assuming no build-up of adsorbed nitrogen atoms, we obtain:

$$k_3 \theta_v \theta_{NO} = k_4 \theta_N^2 + k_5 \theta_N P_{NO} \tag{3-6}$$

Assuming no buildup of adsorbed oxygen atoms,

$$k_3 \theta_{NO} \theta_v = k_6 P_{CO} \theta_v \tag{3-7}$$

Assuming reaction 2 in Figure 28 is at equilibrium,

$$\theta_{NO} = K_2 \theta_v P_{NO} \tag{3-8}$$

Solving equation 3-4 for θ_O and substituting into 3-7 yields:

$$k_3 \theta_{NO} \theta_v = k_6 P_{CO} (1 - \theta_v) \tag{3-9}$$

Substituting 3-8 into 3-9:

$$k_3 K_2 \theta_v^2 P_{NO} = k_6 P_{CO} (1 - \theta_v) \tag{3-10}$$

$$\theta_v^2 = \frac{k_6 P_{CO}}{k_3 K_2 P_{NO}}$$

If θ_v is assumed small compared to 1,

$$\theta_v^2 = \frac{k_6 P_{CO}}{k_3 K_2 P_{NO}} \tag{3-11}$$

If equation 3-10 is solved for θ_v,

$$\theta_v = \frac{k_6 P_{CO}}{2k_3 K_2 P_{NO}} \left[\left(1 + \frac{4k_3 K_2 P_{NO}}{k_6 P_{CO}} \right)^{1/2} - 1 \right] \tag{3-12}$$

Subsituting 3-8 and 3-10 into 3-6, one obtains:

$$k_4 \theta_N^2 + k_5 \theta_N P_{NO} = k_6 P_{CO} (1 - \theta_v) \tag{3-13}$$

Solving 3-13 for θ_N via the quadratic formula leads to:

$$\theta_N = \frac{k_6 P_{NO}}{2k_4} \left[\left(1 + \frac{4k_4 k_6 P_{CO}(1-\theta)}{k_5^2 P_{NO}^2} \right)^{1/2} - 1 \right] \tag{3-14}$$

Substituting 3-14 into 3-5, the ratio $R_{N_2}/R_{N_2 O}$ is obtained:

$$\frac{R_{N_2}}{R_{N_2 O}} = \frac{1}{2} \left[\left(1 + \frac{4k_4 k_6 P_{CO}(1-\theta_v)}{k_5^2 P_{NO}^2} \right)^{1/2} - 1 \right] \tag{3-15}$$

Under highly oxidizing conditions where θ_o is large compared to θ_v, θ_v will be much less than one, and equation 3-15 reduces to:

$$\frac{R_{N_2}}{R_{N_2 O}} = \frac{1}{2} \left[\left(1 + \frac{4k_4 k_6 P_{CO}}{k_5^2 P_{NO}^2} \right)^{1/2} - 1 \right] \tag{3-16}$$

Assuming reaction 6 in Figure 28 is rate limiting,

$$R_{CO_2} = k_6 \theta_O P_{CO} \tag{3-17}$$

Under highly oxidizing conditions, $\theta_o \simeq 1$ and therefore:

$$R_{CO_2} \simeq k_6 P_{CO} \tag{3-18}$$

In a CFSTR operating at 100% CO conversion, $R_{CO_2} = F^O_{CO}$, where F^O_{CO} is the input molar feed rate of CO. Under these conditions, 3-18 becomes:

$$F^O_{CO} = k_6 P_{CO} \qquad (3-19)$$

Substitution into 3-16 yields:

$$\frac{R_{N_2}}{R_{N_2O}} = \frac{1}{2}\left[\left(1 + \frac{4k_4 F^O_{CO}}{k_5^2 P_{NO}^2}\right)^{1/2} - 1\right] \qquad (3-20)$$

Substitution of 3-20 into equation 2-11 in Appendix 2 yields, with rearrangement:

$$(2/S_{N_2O} - 1)^2 - 1 = \left(\frac{4k_4}{k_5^2}\right) \frac{F^O_{CO}}{P_{NO}^2} \qquad (3-21)$$

Equation 3-21 is presented in Table 7.

B. Langmuir-Hinshelwood N_2O Production, $P_{NO} > P_{CO}$

The equation for R_{N_2}/R_{N_2O} is identical to that obtained under reducing conditions, since equations 2-13 through 2-17 are applicable in the oxidizing region as well.

REFERENCES

1. N. W. Cant, P. C. Hicks, and B. S. Lenon, "The Reduction of Nitric Oxide by Carbon Monoxide Over Silica Supported Noble Metals," to be published.

2. W. L. Winterbottom, Surface Science, 37, 195, (1973).

3. R. M. Lambert and C. M. Comrie, Surface Science, 46, 61, (1974).

4. Y. Iwasawa, R. Mason, M. Textor and G. A. Somorjai, Chemical Physical Letters, 44, 468 (1976).

5. L. H. Little, "Infrared Spectra of Adsorbed Species," Academic Press, New York, 1966.

6. G. Pirug and H. P. Bonzel, Journal of Catalysis, 50, 64, (1977).

7. H. P. Bonzel and G. Pirug, Surface Science, 62, 45, (1977).

8. F. Solymosi, J. Sarkany and A. Schauer, Journal of Catalysis, 46, 297, (1977).

9. C. N. Ludvik, "An Infrared and Kinetic Study of NO Reduction by CO Over a Pt Catalyst," M.S. thesis, Department of Chemical Enginering, University of California, Berkeley.

10. H. Dunken and H. Hobert, Z. Chem., 3, 398, (1963).

11. M. F. Brown and R. D. Gonzalez, Journal of Catalysis, 44, 477 (1976).

12. G. L. Bauerle, G. Service and K. Nobe, Ind. Eng. Chem. Prod. Res. Dev., 11, 54, (1972).

13. M. Shelef and J. T. Kummer, Chem. Eng. Prog. Symp. Ser., 67, 74, (1972).

14. M. Shelef and H. Gandhi, Ind. Eng. Prod. Res. Dev., 11, 393, (1972).

15. Shelef, K. Otto and H. Gandhi, Journal of Catalysis, 12, 361, (1968).

16. H. Niiyama, M. Tanaka, H. Iida and E. Echigoya, Bulletin of the Chemical Society of Japan, 49, 2047, (1976).

17. M. L. Unland, Journal of Physical Chemistry, 77, 1952 (1973).

18. M. L. Unland, Journal of Catalysis, 31, 459 (1973).

19. M. L. Unland, Science, 179, 567 (1973).

20. R. A. Dalla Betta and M. Shelef, Journal of Molecular Catalysis, 1, 431, (1975/76).

21. D. D. Eley, G. M. Kiwanuka and C. H. Rochester, J.C.S. Faraday Trans. I., 71, 1021, (1975).

22. A. Guillet, M. Coudurier and J. B. Donnet, Bulletin de la Soceite Chimique de France, 7-8, 1563, (1975).

23. E. E. Petersen, J. Landau and E. Saucedo, "Catalytic Chemistry of Nitrogen Oxides," ed. R. L. Klimisch and J. G. Larson, Plenum Press, New York, 1975.

24. A. F. Beck, M. A. Heine, E. J. Caule and M. J. Pryor, Corrosion Science, 7, 1-22, (1967).

25. D. H. Lorimer and A. T. Bell, I&E.C. Fundamentals, 15, 71, (1976).

26. V. S. Boronin, V. S. Nikulina and I. M. Poltorak, Russ. J. Phys. Chem., 37, 626, (1963).

27. H. A. Benesi, R. M. Curtis and H. P. Studer, Journal of Catalysis, 10, 328, (1968).

28. W. H. Weinberg and R. P. Merrill, Journal of Catalysis, 40, 268, (1975).

29. P. B. Weisz and C. D. Prater, Advan. Catal., 6, 167, (1954).

30. M. Wilf and P. T. Dawson, Surface Science, 60, 561, (1976).

31. K. Schawaha and E. Bechtold, Surface Science, 66, 383, (1977).

32. W. H. Weinberg and R. P. Merrill, Surface Science, 39, 206, (1973).

33. H. P. Bonzel and R. Ku, Journal of Vacuum Science and Technology, 9, (2), 663, (1972).

34. J. Katzer, "Catalytic Chemistry of Nitrogen Oxides," ed. R. L. Klimisch and J. G. Larson, Plenum Press, New York, 1975.

35. D. Monroe, Ph.D. thesis, Department of Chemical Engineering, University of California, Berkeley.

36. B. Lang, R. W. Joyner and G. A. Somorjai, Surface Science, 30, 454, (1972).

37. J. L. Gland and V. N. Vorchak, GM Research Labs Report #PC-66, June 28, 1977.

38. H. Hopster, H. Ibach and G. Comsa, Journal of Catalysis, 46, 37, (1977).

39. A. Amiranazmi and M. Boudart, Journal of Catalysis, 39, 383 (1975).

40. P. G. Harrison and E. W. Thornton, J.C.S. Chem. Comm., 398, (1977).

41. M. Primet, J. M. Basset, M. V. Mathieu and M. Prettre, J. Catal., 29, 213 (1973).

42. B. A. Morrow and I. A. Cody, J.C.S. Faraday Trans., I, 71, 1021, (1975).

43. F. A. Miller and G. L. Carlson, Spectrochim. Acta, 17, 977, (1961).

44. F. Solymosi, J. Kiss and J. Sarkany, Proc. 7th Intern. Vac. Congr. and 3rd Intern. Conf. Solid Surfaces, Vienna, 1977.

45. W. Beck and W. P. Fehlhammer, Angew. Chem., 79, 146, (1967).

46. Kirk-Othmer Encyclopedia of Chemical Technology, 2nd ed., 20, 662, Interscience Publishers, New York, 1963.

47. F. Solymosi and J. Rasko, Journal of Catalysis, 49, 240, (1977).

48. R. J. H. Voorhoeve, L. E. Trimble and D. J. Freed, "Synthesis of Ammonium Cyanate and Urea by Reduction of NO on Pt, Rh, and Ru Catalysts," to be published.